nature nanotechnology

SUPPLEMENTARY INFORMATION

https://doi.org/10.1038/s41565-019-0401-6

In the format provided by the authors and unedited.

Unidirectional rotary motion in a metal–organic framework

Wojciech Danowski[1], Thomas van Leeuwen[1], Shaghayegh Abdolahzadeh[2], Diederik Roke[1], Wesley R. Browne[1,2]*, Sander J. Wezenberg[1]* and Ben L. Feringa[1]*

[1]Centre for Systems Chemistry, Stratingh Institute for Chemistry, University of Groningen, Groningen, The Netherlands. [2]Molecular Inorganic Chemistry Group, Stratingh Institute for Chemistry, University of Groningen, Groningen, The Netherlands. *e-mail: w.r.browne@rug.nl; s.j.wezenberg@rug.nl; b.l.feringa@rug.nl

Supporting Information

Unidirectional Rotary Motion in a Metal Organic Framework

Wojciech Danowski, Thomas van Leeuwen, Shaghayegh Abdolahzadeh, Diederik Roke, Wesley R. Browne*, Sander J. Wezenberg*, Ben L. Feringa*

Centre for Systems Chemistry,Stratingh Institute for Chemistry, University of Groningen, Nijenborgh 4, 9747AG Groningen, The Netherlands

Email: b.l.feringa@rug.nl, s.j.wezenberg@rug.nl, w.r.brwone@rug.nl

Table of Contents

1. General Information

All reagents were obtained from commercial sources and used as received without further purification. Compounds **3**[1], **4**[2], **6**[3], **DPNI**[4] and **TCPB**[4] were synthesized according to literature procedures. Crystals of the parent Metal Organic Framework were synthesized according to a literature procedure.[4] Dry solvents were obtained from an MBraun solvent purification system. Column chromatography was performed on a Reveleris X2 flash chromatography system. TLC: silica gel 60, Merck, 0.25 mm. HRMS were recorded on an LTQ Orbitrap XL, and Elemental (C,H,N) Analysis was performed on a Elementar vario MICRO cube: Elemental Analyzer, ICP-OES was performed on a PerkinElmer optical emission spectrometer Optima 7000 DV. NMR spectra were obtained using a Varian Mercury Plus (^{1}H: 400 MHz, ^{13}C: 100 MHz ^{19}F: 376 MHz) or a Varian Innova (^{1}H: 500 MHz) instrument. Chemical shifts are reported in δ units (ppm) relative to the residual solvent signal of $CDCl_3$ (^{1}H NMR, δ 7.26 ppm; ^{13}C NMR, δ 77.0 ppm) MeOH-d_4 (^{1}H NMR, δ 3.31 ppm; ^{13}C NMR, δ 49.0 ppm) or DMSO-d_6 (^{1}H NMR, δ 2.50 ppm; ^{13}C NMR, δ 39.5 ppm). The splitting pattern of peaks is designated as follows: s (singlet), d (doublet), t (triplet), m (multiplet), br (broad), p (quintet) or dd (doublet of doublets). UV/Vis absorption spectra were measured on a Hewlett-Packard 8453 diode array spectrometer in a 1 cm quartz cuvette. Solvents used for spectroscopic studies were of spectroscopic grade (UVASOL, Merck*)*. UV/Vis irradiation experiments were performed using Thorlab LED (M395F1). NMR irradiation experiments were performed at −30 °C with a Thorlab model M395F1 LED coupled to a 0.6 mm optical fiber, which guided the light into the NMR tube inside the spectrometer.[5] Raman spectra were recorded using a Perkin Elmer Raman Station connected to a microscope equipped with a 785 nm 50 mW laser. Raman irradiation experiments were performed using Thorlab LEDs (M395F1). PXRD data were obtained for the capillary-encapsulated samples at room temperature with a Bruker D8 Advance diffractometer equipped with a Cu Kα source (λ = 0.15406 nm). Samples were mounted in capillaries with supernatant liquid; capillaries were sealed with wax and placed on the goniometer head for mounting on the diffractometer. SC X-ray data was collected using Bruker Proteum diffractometer with rotating anode and Cu radiation and Helios optics (λ = 1.54184 Å) at a temperature of 100 K. Density functional theory (DFT) calculations were carried out with the Gaussian 09 program (rev. D.01).[6] All of the calculations were performed on systems in the gas phase using the Becke's three-parameter hybrid functional[7] with the LYP correlation functional[8,9] (DFT B3LYP/6-31G(d,p)). Each geometry optimization was followed by a vibrational analysis to determine that a minimum or saddle point on the potential energy surface was found.

Kinetic Measurements

UV/Vis samples in heptane, chloroform or DMF (~1×10^{-5} M) were irradiated with a Thorlab LED (M395F1) between 7 and 16 °C to reach PSS. The thermal helix inversion was followed by recording UV/Vis spectra with 30-120 s intervals. The absorbance at 480 nm was followed in time in order to extract the rate constants used for the Eyring plots. A least squares analysis was performed on the Eyring equation.

Kinetic Measurements in moto-MOFs

Crystals of **moto-MOF1** closed in a 1 mm quartz cuvette filled with DMF or between two quartz slides, were irradiated with a Thorlab LED (M395F1) at 20 °C on the microscope stage until no changes were observed in the Raman spectrum. The thermal helix inversion was followed by recording Raman spectra with 1-5 min intervals. The changes in the area of the band centered at 1550 cm^{-1} was followed in time in order to determine the rate constant and Gibbs free energy of activation of THI.

2. Synthetic Procedures

Synthesis of motor 1 and 2-*E*/*Z*

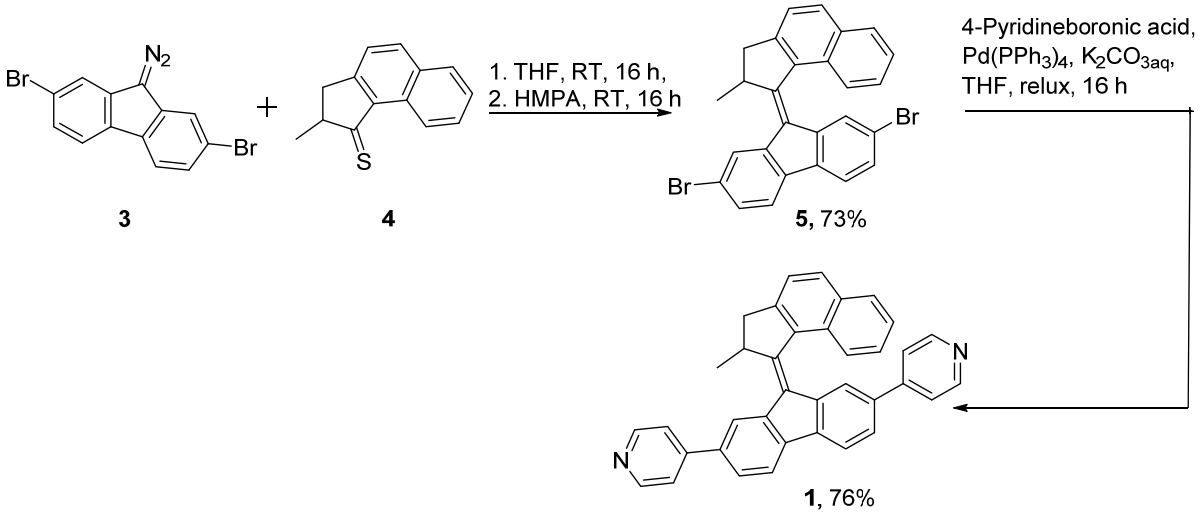

Scheme S1. Synthesis of motor **1**.

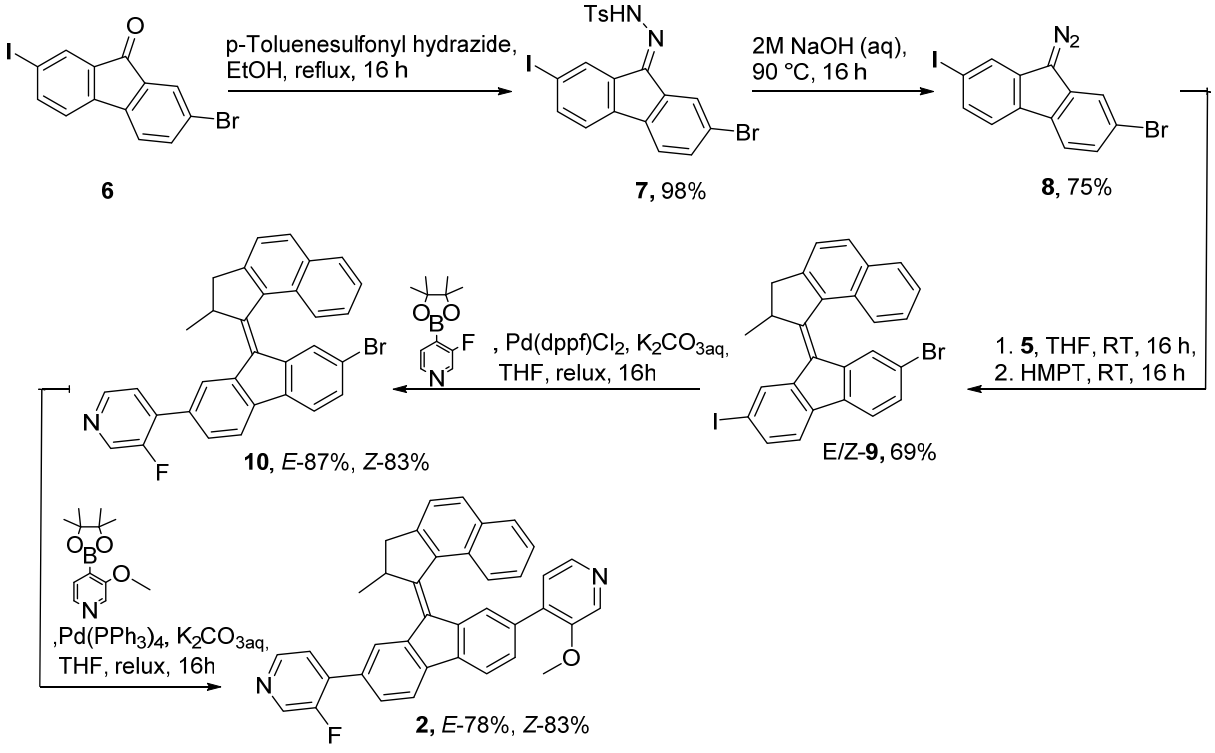

Scheme S2. Synthesis of motor **2**.

(*E*/*Z*) *N*'-(2-bromo-7-iodo-9*H*-fluoren-9-ylidene)-4-methylbenzenesulfonohydrazide (7)

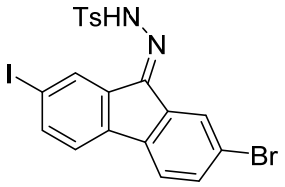

A two-neck round-bottom flask was charged with 2-bromo-7-iodo-9*H*-fluoren-9-one (**6**) (2.00 g, 5.19 mmol) and *p*-toluenesulfonyl hydrazide (1.2 eq. 1.16 g, 6.23 mmol) and EtOH (100 mL) was added. The resulting suspension was heated at reflux and stirred at this temperature for 16 h. The reaction mixture was cooled down to room temperature and the precipitate was filtrated off, washed with EtOH (30 mL) and dried at air to afford **7** as a pale yellow solid (*E*/*Z* mixture 1/1 ratio, 2.80 g, 5.10 mmol, 98%).The product was used in the next reaction step without further purification. ^{1}H NMR (400 MHz, DMSO-d_6): δ 8.38 (s, 1H) 8.22 (s, 1H), 7.97 – 7.83 (m, 5H), 7.83 – 7.51 (m, 10H), 7.46 (d, *J* = 8.0 Hz, 5H), 2.38 (s, 6H). HRMS (ESI) calcd $C_{20}H_{15}BrNISO_2$ $[M+H]^+$ 552.9077 found 552.9085.

2-bromo-9-diazo-7-iodo-9*H*-fluorene (8)

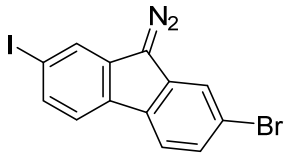

A round-bottom flask was charged with *N*-tosylhydrazone **7** (2.00 g 3.61 mmol) and an aqueous solution of NaOH (2 M, 100 mL) was added. The resulting suspension was heated at 90 °C and stirred at this temperature for 16 h. The resulting suspension was cooled down to room temperature and the aqueous phase was extracted with CH_2Cl_2 (3 x 100 mL). The combined organic layers were washed with brine (150 mL), dried over $MgSO_4$ and concentrated *in vacuo*. The pure product was obtained by crystallization from Et_2O to afford **8** as pink needle-shaped crystals (1.10 g, 2.70 mmol, 75%) ^{1}H NMR (400 MHz, $CDCl_3$): δ 7.82 (t, *J* = 1.0 Hz, 1H), 7.75 (d, *J* = 8.2 Hz, 1H), 7.62 (dd, *J* = 2.7 Hz, 1.4 Hz, 3H), 7.43 (dd, *J* = 8.3 Hz, 1.7 Hz, 1H). ^{13}C NMR (100 MHz, $CDCl_3$) δ 134.5, 134.1, 133.4, 129.7, 129.2, 127.8, 127.7, 122.2, 122.0, 121.8, 120.5, 91.3. (Resonance corresponding to carbon connected to diazo moiety was not observed).

(*E*/*Z*)-2-bromo-7-iodo-9-(2-methyl-2,3-dihydro-1*H*-cyclopenta[a]naphthalen-1-ylidene)-9*H*-fluorene (9)

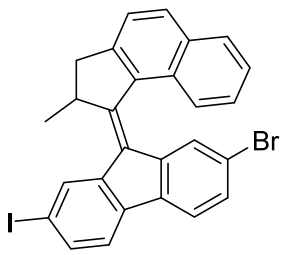

A two-neck flask was charged with 2-bromo-9-diazo-7-iodo-9*H*-fluorene (**8**) (794 mg, 2.00 mmol) and a solution of thioketone **4** (552 mg, 2.60 mmol) in dry THF (20 mL) was added. The reaction mixture was stirred at room temperature for 16 h. Subsequently tris(dimethylamino)phosphine (4 eq. 1.30 g, 8.00 mmol, 1.4 mL) was added and the resulting mixture was stirred at room temperature for 16 h. After purification by column chromatography (SiO_2, pentane/CH_2Cl_2) **9** was obtained as a yellow solid (*E*/*Z* mixture 1/1.1 ratio, 760 mg, 1.38 mmol, 69%). ^{1}H NMR (400 MHz, $CDCl_3$) δ 8.30 (d, *J* = 1.4 Hz, 1H), 8.08 (d, *J* = 1.6 Hz, 1H), 7.97 (dd, *J* = 7.1 Hz, 2.9 Hz, 4H), 7.76 – 7.29 (m, 16H), 6.94 (d, *J* = 1.4 Hz, 1H), 6.75 (d, *J* = 1.6 Hz, 1H) 4.29 (q, *J* = 5.9 Hz, 2H), 3.58 (dd, *J* = 15.2, 5.6 Hz, 2H), 2.81 (d, *J* = 15.2 Hz, 2H), 1.41 (m, *J* = 6.8 Hz, 3.6 Hz, 6H). ^{13}C NMR (101 MHz, $CDCl_3$) δ 154.1, 148.1, 148.1, 141.4, 140.8, 138.4, 138.1, 138.0, 137.7, 137.5, 137.1, 135.4, 135.2, 135.0, 133.0, 132.5, 132.5, 131.8, 131.8, 129.5, 129.4, 129.3, 129.2, 128.8, 127.7, 127.6, 126.9, 126.9, 126.8, 126.8, 125.5, 125.5,

123.8, 123.7, 121.1, 121.0, 120.7, 120.2, 120.1, 119.9, 92.3, 91.2, 45.1, 45.0, 41.8, 41.8, 19.2, 19.1. HRMS (APCI neg.) calcd $C_{27}H_{17}BrI$ $[M-H]^-$ 546.9553 found 546.9553.

(*E*)/(*Z*)-4-(7-bromo-9-(2-methyl-2,3-dihydro-1*H*-cyclopenta[a]naphthalen-1-ylidene)-9*H*-fluoren-2-yl)-3-fluoropyridine (10-*E*), (10-*Z*)

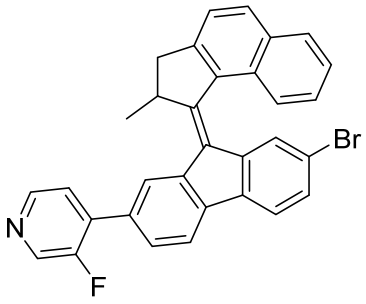

A two-neck round-bottom flask equipped with a reflux condenser was charged with a *E*/*Z* (1/1.1 ratio) mixture of **9** (505 mg 0.92 mmol), 3-fluoro-4-pyridineboronic acid pinacol ester (225 mg, 1.0 mmol), and $Pd(dppf)Cl_2•CH_2Cl_2$ (0.05 eq., 38 mg, 0.046 mmol). A degassed aqueous solution of K_2CO_3 (1 M, 10 eq., 9.2 mL) and THF (10 mL) were added and the resulting mixture was stirred at reflux for 5 h. Subsequently, the reaction mixture was cooled to room temperature, diluted with EtOAc (20 mL) and the phases were separated. The aqueous phase was extracted with EtOAc (2 x 10 mL) and the combined organic layers were washed with brine (20 mL), dried over $MgSO_4$ and concentrated *in vacuo*. Purification by column chromatography, during which the *E*-*Z* isomers could be readily separated, (SiO_2 pentane/EtOAc) afforded **10-*E*** and **10-*Z*** as yellow solids (0.38 mmol, 197 mg, 87% **10-*E***, 0.40 mmol, 207 mg, 83% **9-*Z***). **10-*E***: ^{1}H NMR (400 MHz, $CDCl_3$) δ 8.30 (d, *J* = 2.7 Hz, 1H), 8.12 (d, *J* = 1.6 Hz, 1H), 8.05 (dd, *J* = 9.3 Hz, 6.6 Hz, 2H), 7.96 (d, *J* = 8.2 Hz, 1H), 7.86 – 7.72 (m, 3H), 7.63 – 7.51 (m, 4H), 7.41 (ddd, *J* = 8.2 Hz, 6.8 Hz, 1.3 Hz, 1H), 6.90 (d, *J* = 1.5 Hz, 1H), 6.14 (dd, *J* = 6.9, 5.0 Hz, 1H), 4.32 (p, *J* = 6.6 Hz, 1H), 3.59 (dd, *J* = 15.3 Hz, 5.6 Hz, 1H), 2.82 (d, *J* = 15.3 Hz, 1H), 1.44 (d, *J* = 6.7 Hz, 3H). ^{13}C NMR (100 MHz, $CDCl_3$) δ 153.4, 148.1, 145.4, 145.3, 141.7, 139.0, 138.6, 138.3, 137.8, 137.1, 135.5, 132.6, 131.6, 131.5, 131.2, 130.4, 130.3, 129.7, 129.7, 129.0, 128.7, 127.9, 127.8, 127.0, 127.0, 125.6, 124.0, 123.5, 121.3, 121.2, 118.9, 45.0, 41.9, 19.1. (more signals were observed due to coupling to ^{19}F). ^{19}F NMR (376 MHz, $CDCl_3$): -132.82 (d). HRMS (ESI) calcd $C_{32}H_{22}BrNF$ $[M+H]^+$ 518.0914 found 518.0911. **10-*Z***: ^{1}H NMR (400 MHz, $CDCl_3$) δ 8.60 (s, 1H), 8.53 (d, *J* = 4.9 Hz, 1H), 8.29 (s, 1H), 8.02 – 7.90 (m, 3H), 7.71 – 7.57 (m, 4H), 7.58 – 7.49 (m, 2H), 7.46 – 7.34 (m, 2H), 6.80 (d, *J* = 1.7 Hz, 1H), 4.38 (p, *J* = 6.6 Hz, 1H), 3.61 (dd, *J* = 15.3 Hz, 5.7 Hz, 1H), 2.83 (d, *J* = 15.2 Hz, 1H), 1.44 (d, *J* = 6.7 Hz, 3H), ^{13}C NMR (100 MHz, $CDCl_3$) δ 153.9, 148.0, 145.8, 145.7, 139.7, 139.7, 139.0, 138.9, 138.7, 137.1, 136.7, 136.6, 135.3, 132.5, 131.8, 131.3, 131.3, 129.5, 129.3, 129.0, 128.8, 128.3, 127.3, 127.2, 126.9, 126.8, 125.5, 124.6, 124.6, 123.8, 120.4, 120.3, 119.9, 45.3, 41.8, 19.2. ^{19}F NMR (376 MHz, $CDCl_3$): -132.57 (br). HRMS (ESI) calcd $C_{32}H_{22}BrFN$ $[M+H]^+$ 518.0914, found 518.0920.

(*E*)/(*Z*)-3-fluoro-4-(7-(3-methoxypyridin-4-yl)-9-(2-methyl-2,3-dihydro-1*H*-cyclopenta[a]naphthalen-1-ylidene)-9*H*-fluoren-2-yl)pyridine (2-*E*), (2-*Z*)

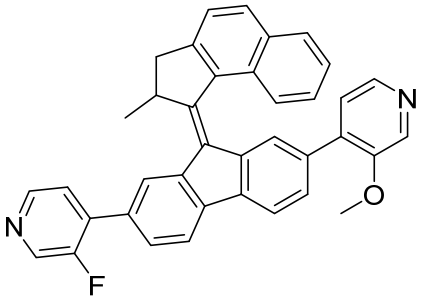

A two-neck round-bottom flask equipped with a reflux condenser was charged with **10-*E*** or **10-*Z*** (119 mg 0.23 mmol), 3-methoxy-4-pyridineboronic acid pinacol ester (1.4 eq., 75 mg, 0.32 mmol) and $Pd(PPh_3)_4$ (13 mg, 0.012 mmol). A degassed aqueous solution of K_2CO_3 (1 M, 2.3 mL) and THF (10 mL) were added and the resulting mixture was stirred at reflux for 2 h. Subsequently, the reaction mixture was cooled to room temperature, diluted with EtOAc (10 mL) and the phases were separated. The aqueous phase was extracted with EtOAc (2 x 10 mL) and the combined organic layers were washed with brine (20 mL), dried over $MgSO_4$ and concentrated *in vacuo*. Purification by column chromatography (SiO_2 pentane/EtOAc) afforded **2-*E*** and as yellow solid (0.18 mmol, 98 mg, 78 % **2-*E***) **2-*Z*** was synthesized according to the same procedure and afforded (0.19 mmol, 104 mg, 83 % **2-*Z***). **2-*E***: ^{1}H NMR (400 MHz, $CDCl_3$) δ 8.61 (d, *J* = 2.7 Hz, 1H), 8.53 (dd, *J* = 5.0, 0.8 Hz, 1H), 8.31 (s, 1H), 8.16 (s, 1H), 8.04 – 7.82 (m, 6H), 7.66 (ddd, *J* = 10.4 Hz, 7.9 Hz, 1.5 Hz, 2H), 7.56 (ddd, *J* = 9.7 Hz, 7.6 Hz, 5.7 Hz, 3H), 7.43 (ddd, *J* = 8.3 Hz, 6.8 Hz, 1.3 Hz, 1H), 6.89 (d, *J* = 1.4 Hz, 1H), 6.17 (d, *J* = 4.8 Hz, 1H), 4.38 (p, *J* = 6.6 Hz, 1H), 3.71 (s, 3H), 3.59 (dd, *J* = 15.2 Hz, 5.6 Hz, 1H), 2.81 (d, *J* = 15.2 Hz, 1H), 1.46 (d, *J* = 6.7 Hz, 3H). ^{13}C NMR (100 MHz, $CDCl_3$) δ 157.9, 152.5, 152.2, 147.7, 146.0, 145.9, 142.6, 140.4, 140.2, 139.2, 138.9, 138.3, 137.6, 137.3, 136.5, 136.4, 135.8, 134.1, 133.6, 132.6, 131.3, 129.8, 129.5, 129.0, 128.3, 127.3, 127.3, 127.1, 126.9, 126.1, 125.0, 124.6, 124.5, 124.0, 123.9, 123.8, 120.1, 118.7, 56.0, 45.2, 41.9, 19.2. (more signals were observed due to coupling to ^{19}F). ^{19}F NMR (376 MHz, $CDCl_3$): -132.77 (d). HRMS (ESI) calcd $C_{36}H_{28}FN_2O$ $[M+H]^+$ 547.2180, found 547.2161. **2-*Z***: ^{1}H NMR (400 MHz, $CDCl_3$) δ 8.48 – 8.37 (m, 2H), 8.32 (dd, *J* = 9.5, 2.1 Hz, 2H), 8.01 (ddd, *J* = 33.2 Hz, 8.2 Hz, 5.4 Hz, 4H), 7.88 (dd, *J* = 8.2, 5.4 Hz, 2H), 7.72 – 7.50 (m, 4H), 7.51 – 7.37 (m, 2H), 6.95 (d, *J* = 1.5 Hz, 1H), 6.15 (dd, *J* = 6.9 Hz, 5.0 Hz, 1H), 4.39 (p, *J* = 6.6 Hz, 1H), 4.00 (s, 3H), 3.59 (dd, *J* = 15.3 Hz, 5.7 Hz, 1H), 2.81 (d, *J* = 15.2 Hz, 1H), 1.44 (d, *J* = 6.7 Hz, 3H). ^{13}C NMR (100 MHz, $CDCl_3$) δ 152.4, 147.8, 145.4, 145.3, 143.1, 139.9, 139.5, 139.1, 138.6, 138.3, 137.8, 137.7, 135.8, 135.7, 134.6, 134.4, 132.6, 132.0, 131.9, 131.8, 131.4, 130.3, 129.7, 129.6, 129.0, 128.4, 128.3, 127.9, 127.8, 127.8, 127.1, 126.9, 125.6, 125.1, 125.1, 124.2, 124.0, 123.5, 119.9, 119.1, 56.2, 45.1, 41.9, 19.2. (more signals were observed due to coupling to ^{19}F) ^{19}F NMR (376 MHz, $CDCl_3$): -132.77 (m). HRMS (ESI) calcd $C_{36}H_{28}FN_2O$ $[M+H]^+$ 547.2180 found 547.2183.

3. PXRD Data

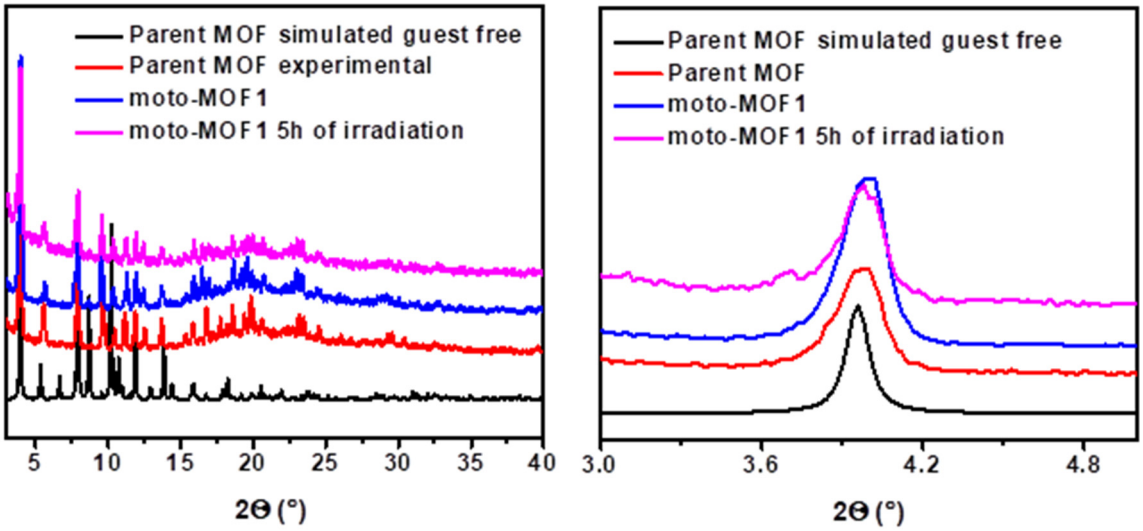

Supplementary Figure 1. PXRD patterns of MOFs, simulated parent MOF (intensity of first peak was decreased three times, black line), experimental parent MOF (red line), moto-MOF**1** after SALE with **1** (blue line) moto-MOF**1** irradiated for 5 h with 395 nm (purple line) (right). Expansion of the PXRD pattern showing the peak corresponding to reflection form the (001) plane (right). The apparent differences between the simulated and experimental PXRD patterns are the result of a preferred crystal orientation, and pore-bound solvent (DMF) molecules. Differences in intensity of peaks in PXRD pattern between the non-irradiated and the 5 h irradiated moto-MOF**1** samples can be attributed to the different sizes of crystals in both samples. As PXRD is destructive for the moto-MOF**1** crystals, different batches were used for collecting PXRD patterns of the irradiated and the non-irradiated moto-MOF**1**.

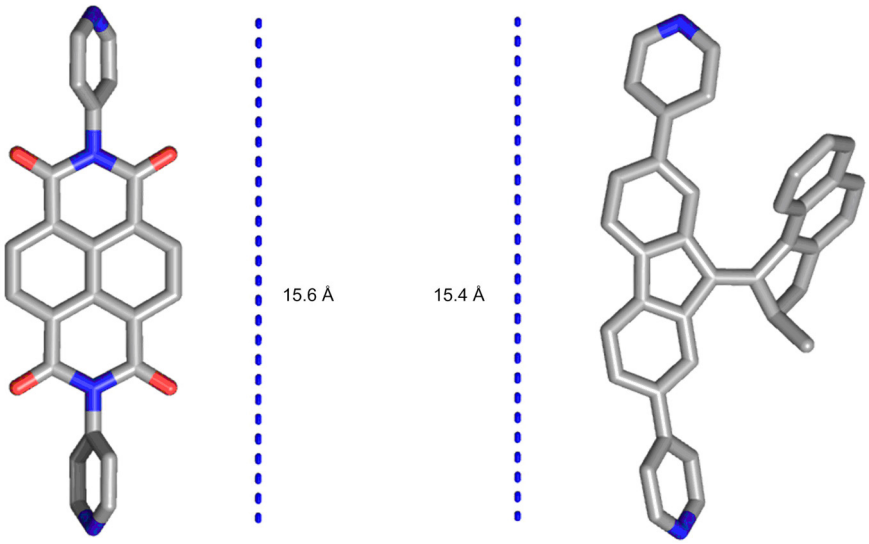

Supplementary Figure 2. Comparison of the N-N distance of DFT (B3LYP/6-31G(d,p)) optimized structures of DPNI and **1**

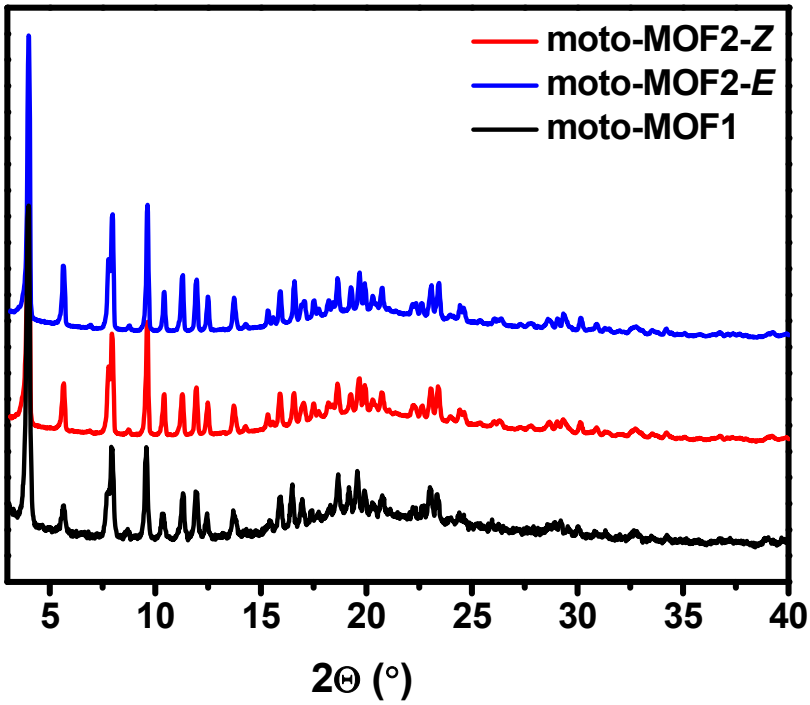

Supplementary Figure 3. Comparison of the PXRD patterns of moto-MOFs with motors **1** (moto-MOF**1**, black line), ***2-E*** (moto-MOF**2**-***E***, blue line), with motor **2**-***Z*** (moto-MOF**2**-***Z***, blue line) pillars.

4. SC XRD Data

X-ray intensities were measured on a Bruker Proteum diffractometer with rotating anode and Cu radiation and Helios optics (λ = 1.54184 Å) at a temperature of 100(2). Based on the strong reflections an orthorhombic unit cell could be found with a = 10.5609(8), b = 16.2194(8), and c = 22.0417(8) Å. These unit cell parameters correspond to the literature structure[4]. The reflection data were integrated with the Eval15 software.[10] Weak superstructure reflections were ignored. A large isotropic mosaicity of 1.8 ° was used for the prediction of reflection profiles. The structure of the 2-dimensionall TCPB could be solved in space group Pmmm (no. 47) with the zinc and bromine atoms on sites with mm2 symmetry, respectively (Supplementary Figure 3). The atomic structure of the molecular motor struts could not be determined (Supplementary Figure 4).

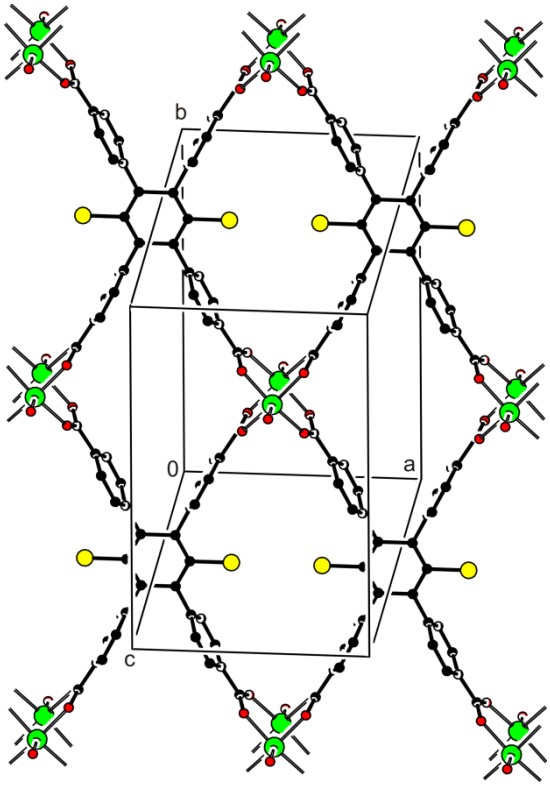

Supplementary Figure 3. Packing diagram of the TCPB in the unit cell of the moto-MOF**1**. Hydrogen atoms and disordered pillars have been omitted in the drawing. Zinc atoms are drawn in green, bromines in yellow, carbons in black, and oxygens, nitrogens in red.

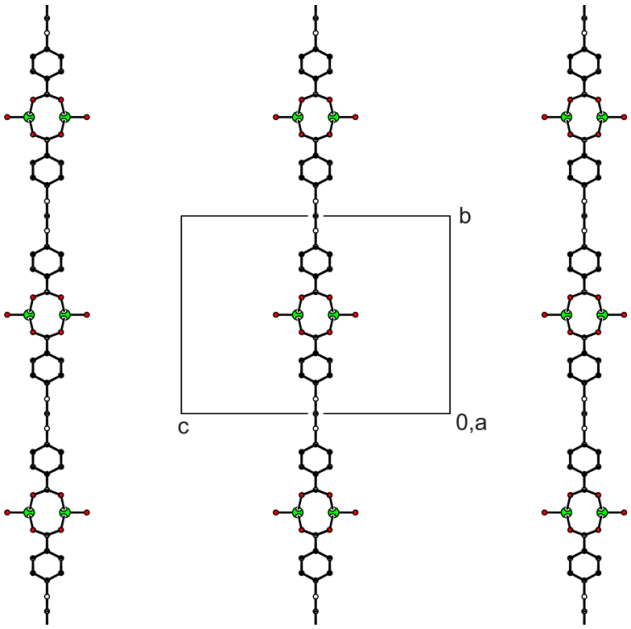

Supplementary Figure 4. Stacking of the two-dimensional layers in the *c* direction. Hydrogen atoms and disordered pillars have been omitted in the drawing. Zinc atoms are drawn in green, bromines in yellow, carbons in black, and oxygens, nitrogens in red. The volume between the layers is filled with diffuse electron density.

Simulated precession images

A reciprocal space reconstruction of the data has been prepared using the routine precession of the Eval15 software. A slice of the (h0l) plane is shown in Supplementary Figure 5.

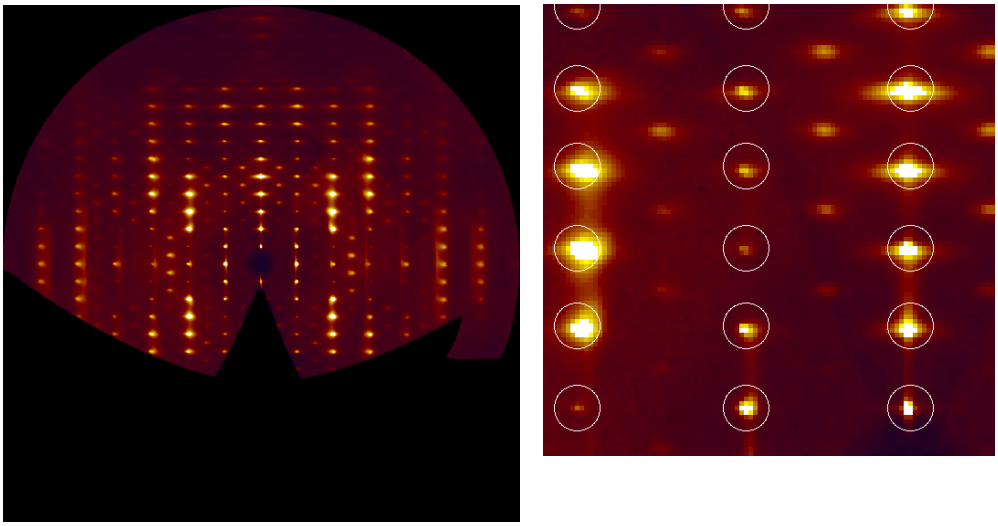

Supplementary Figure 5. Reconstruction of the (h0l) reflection plane. Diffuse streaks are running in the c* direction. The zoom window shows the predicted positions based on the orthorhombic unit cell. The non-indexed weak reflections show incommensurate features.

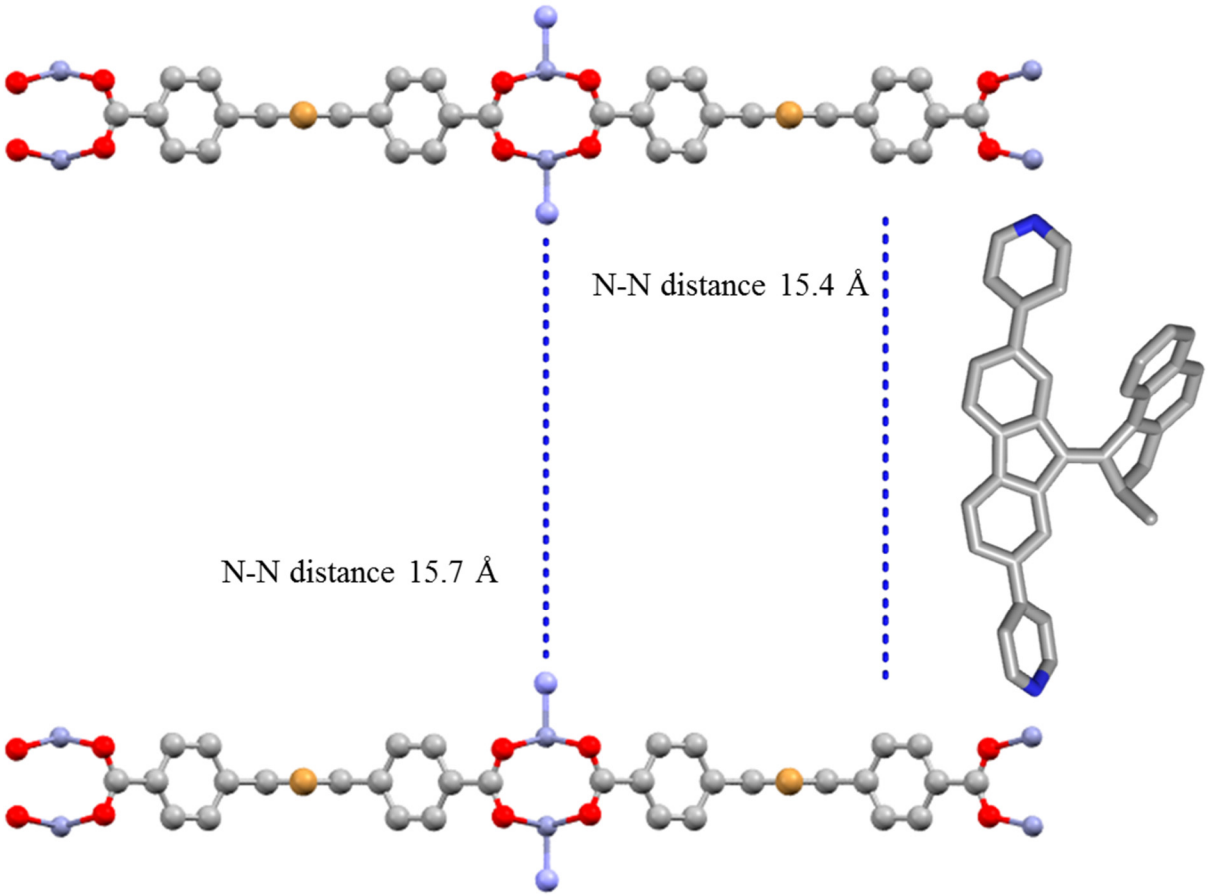

Supplementary Figure 6. Comparison of N-N distance of **1** in moto-MOF**1** and DFT (B3LYP 6-31G(d,p)) optimized structure of **1** (Carbon – grey, Bromine – yellow, Nitrogen – blue, Zinc – silver).

Free Volume analysis

The free volume in Parent MOF crystal was analyzed based on the published X-Ray structure of the parent MOF (ja909519e_si_008)[4] using the Mercury software package. The solvent accessible volume was mapped using a probe radius 1.5 Å with grid spacing 0.1 Å (Supplementary Figure 7) giving a free volume of 1470 $Å^3$ (39.4 % of the cell Volume).

The estimated maximum free volume required for the free rotation of a molecular motor i.e. the volume required for unhindered rotation of the upper-half in respect to lower-half of the motor can be approximated as a cylinder generated by the rotation of the rectangle with the dimensions of the naphtalene moiety (height 7.2 Å, length 6.4 Å), which gives the free volume required 926 $Å^3$. Hence, even with a conservative estimate of the free volume required, the free volume in the framework constructed from **TCPD** is greater than that required for unhindered rotation of the upper-half of the motor **1**.

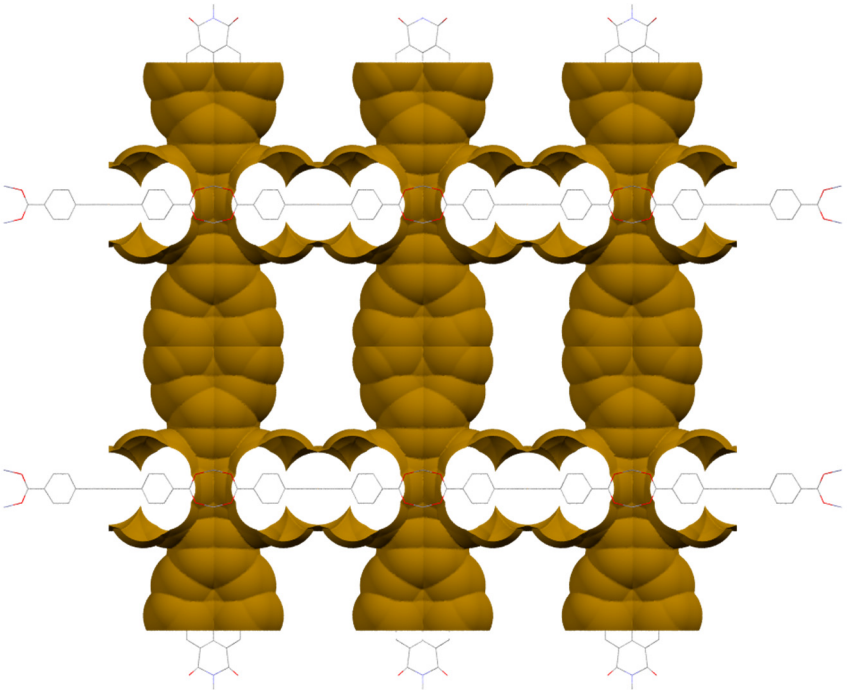

Supplementary Figure 7. Solvent accessible surface in parent MOF

5. Polarized Optical (POM) and Bright Field Optical Microscopy images

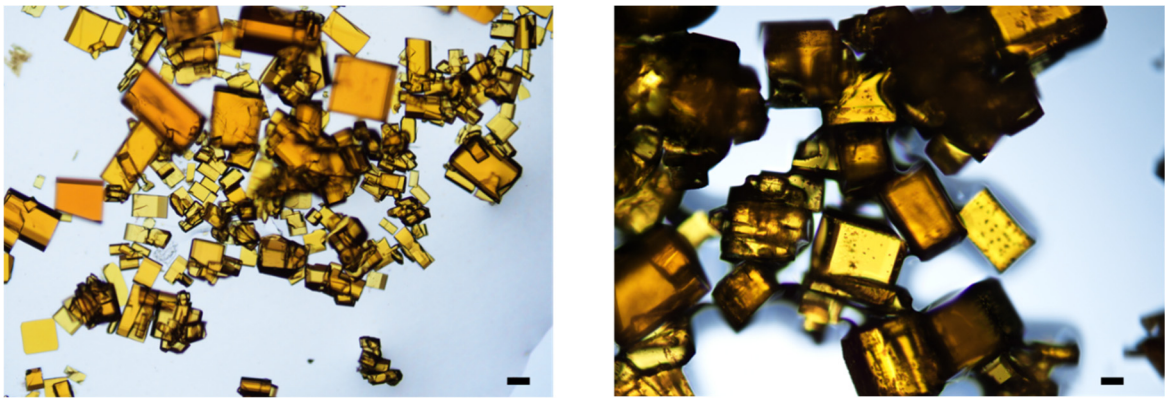

Supplementary Figure 8. Bright Field Optical microscopy images of the moto-MOF**2-Z** (left) and moto-MOF**2-E** (right) crystals (scale bar 100 μm).

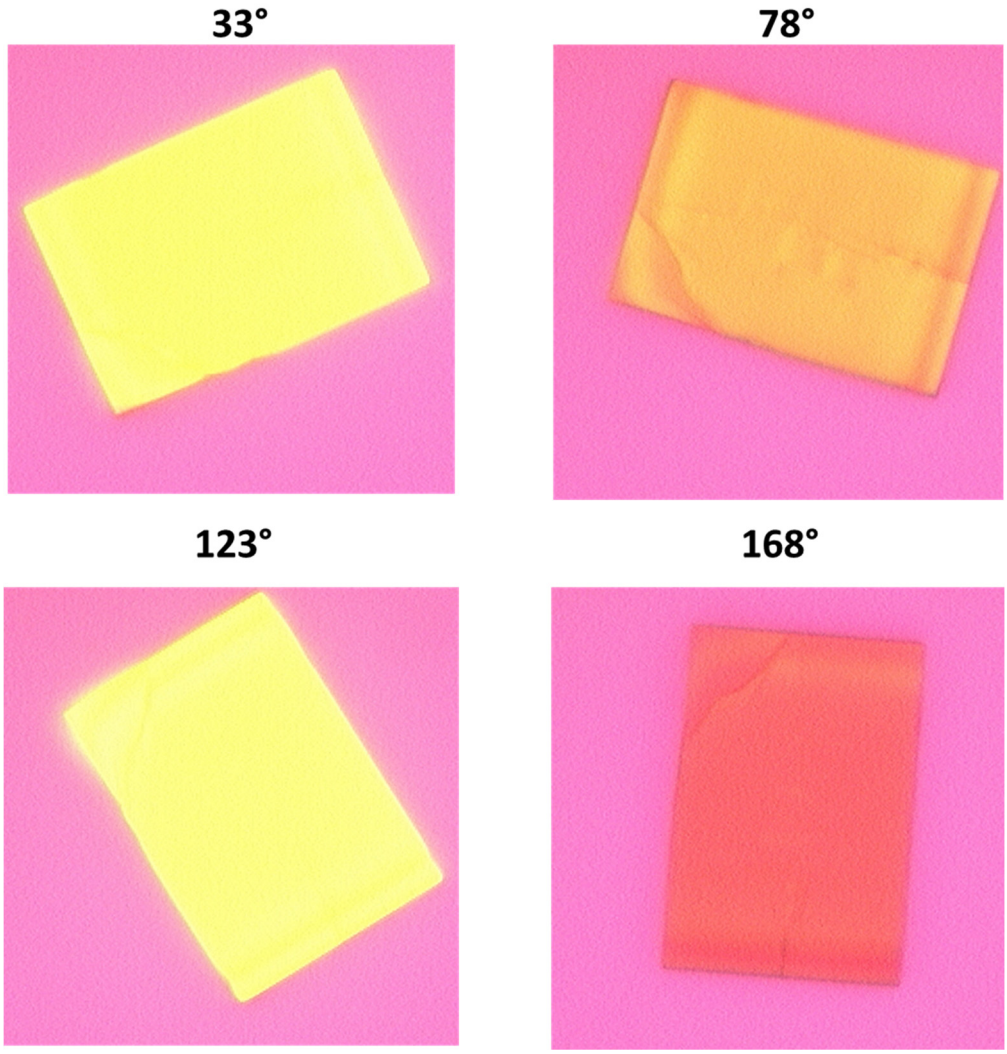

Supplementary Figure 9. Polarized optical microscope (POM) images of the moto-MOF**1** crystals. The crystal was rotated by 33°, 78°, 123° and 168° with respect to the transmission axis of the analyzer.

6. Raman Spectroscopy

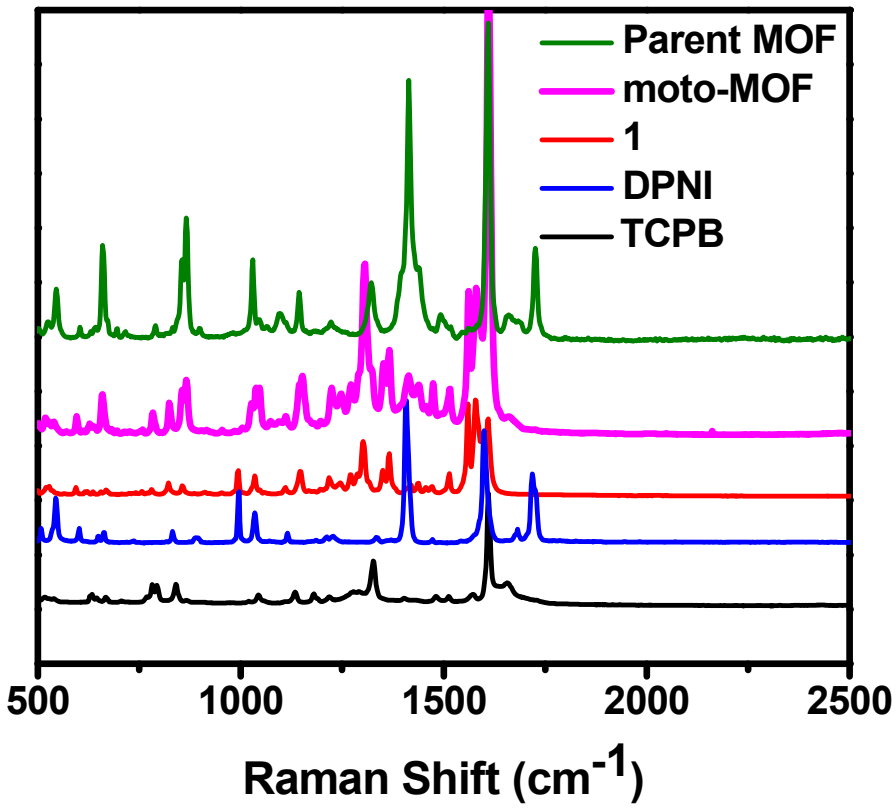

Supplementary Figure 10. Raman spectra of solid samples of **TCPB** (black), **DPNI** (blue), **1** (red) moto-MOF**1** (pink) and parent MOF (green).

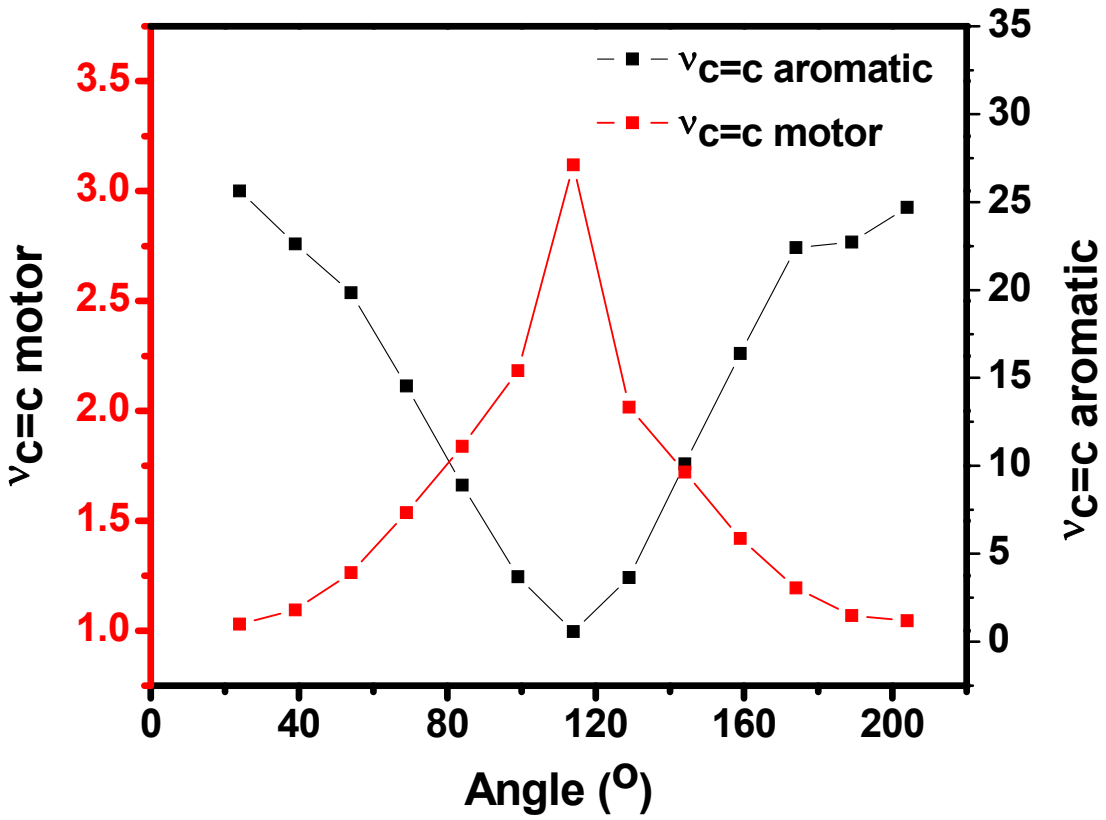

Supplementary Figure 11. Angle dependence of the (normalized) ratio of the band areas recorded with a polarized and non-polarized laser, for the bands centered at 1562 cm^{-1} (stretching of the central double bond of the molecular motor, red squares, left axis) and 1610 cm^{-1} (C=C stretching in the aromatic rings of both **1** and **TCBB**, black rectangles, right axis). During the measurement, the sample was kept under solvent-saturated conditions in a closed quartz cuvette to avoid drying. The sample of the moto-MOF was placed on the manual rotary table, mounted to the microscope stage. Raman spectra were taken in the direction perpendicular to the (001) plane of the single moto-MOF**1** crystal with the linearly polarized and non-polarized laser upon rotating the table every 15°.

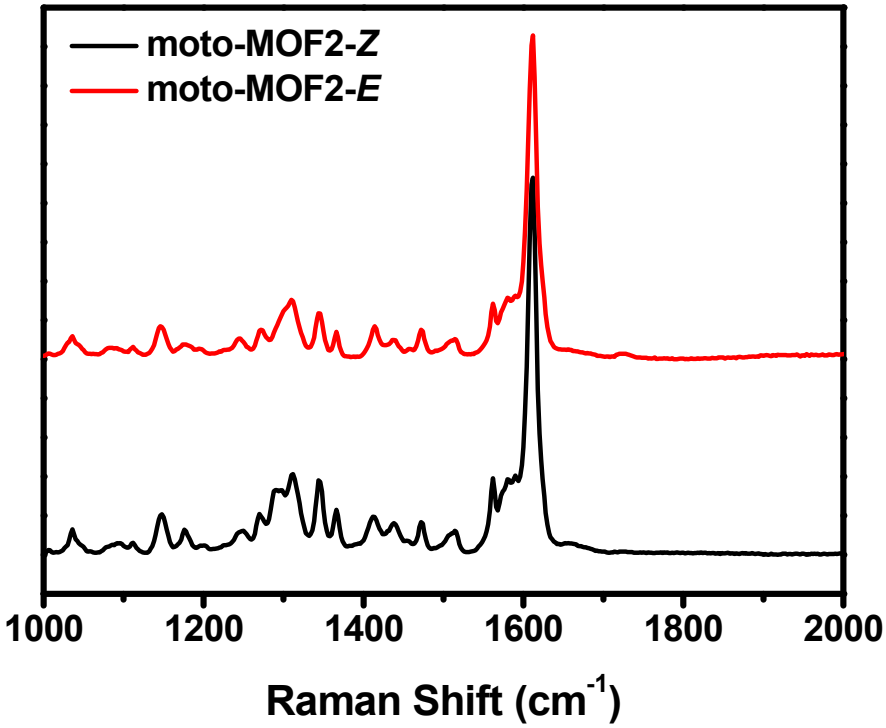

Supplementary Figure 12. Comparison of Raman Spectra of moto-MOF**2-*E*** (red line) and moto-MOF**2-*Z*** (black line)

7. UV/Vis spectra

In the MOF structure, the pyridyl units of 1 are bound to the zinc atoms, which would decrease the electron density in the pyridine rings. To investigate whether such an electronic effect would hamper the rotation, the bis-protonated form of **1** was studied in solution. In the UV/Vis spectrum sequential protonation of **1** in DMF with one and two equivalents of H_2SO_4 resulted in a bathochromic shift of the absorption band associated with the pyridine moieties from 320 nm to 360 nm with clear isosbestic point at 340 nm (upon addition of one and two equivalents of H_2SO_4) (Supplementary Figure 13). Irradiation of the protonated sample with 395 nm light resulted in the photochemical isomerization of stable metastable isomer.

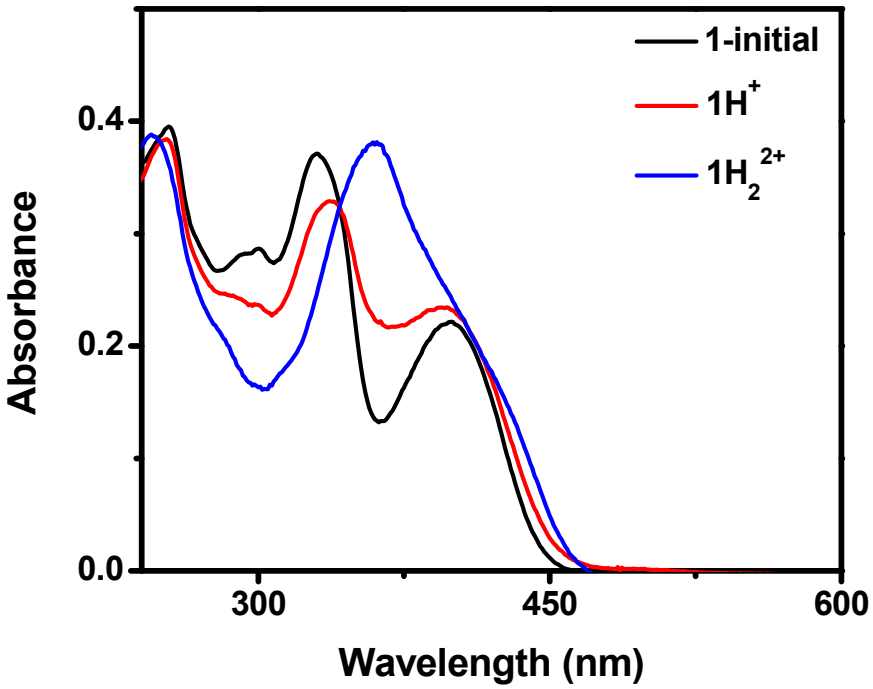

Supplementary Figure 13. Changes in UV/Vis spectrum of **1** (DMF, black line) upon addition of 1 eq. (red line) and 2 eq. (blue line) of H_2SO_4.

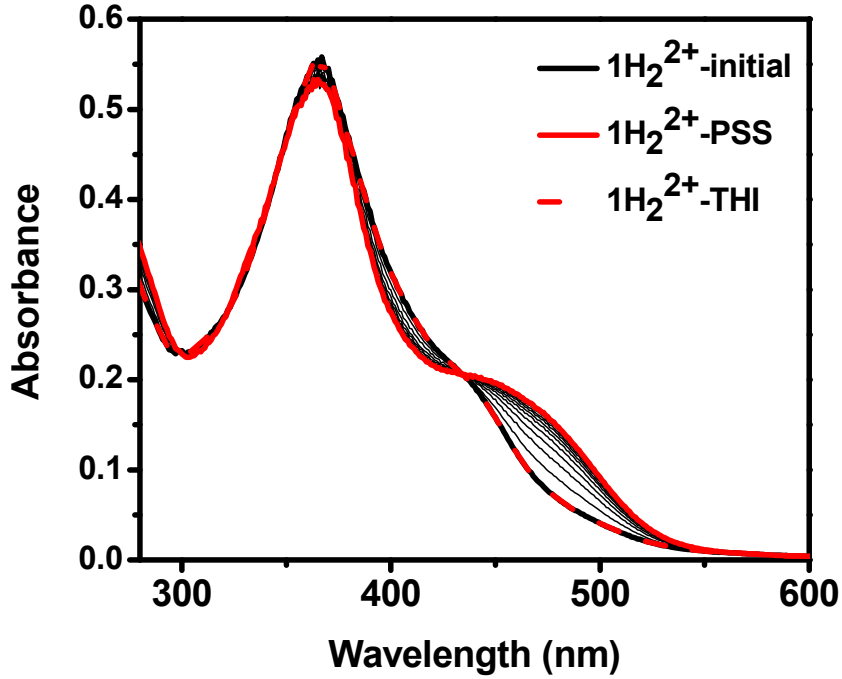

Supplementary Figure 14. Changes in UV/Vis spectra of $\mathbf{1}H_2^{2+}$ upon irradiation with a 395 nm LED. Stable (black solid line), PSS mixture (red solid line), after THI (red dashed line).

8. Eyring Plots

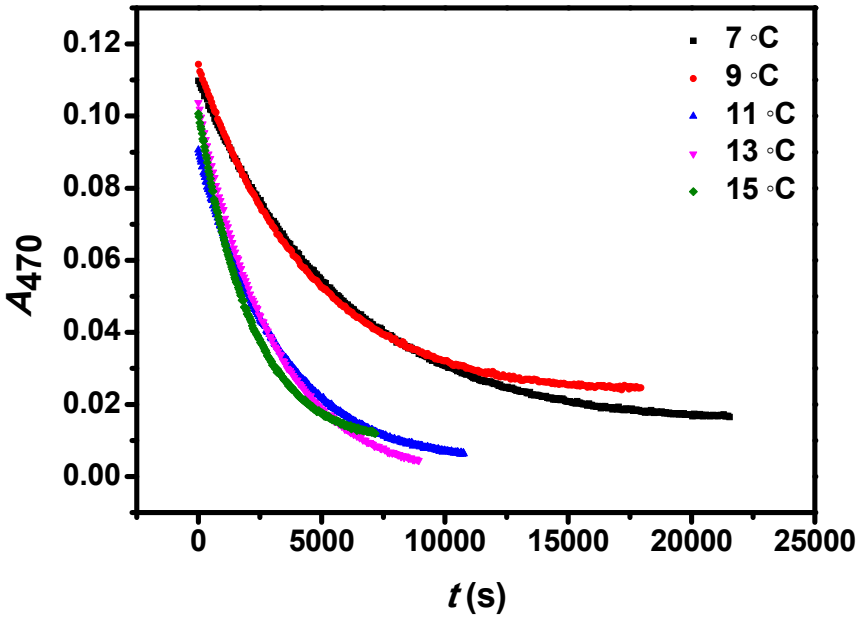

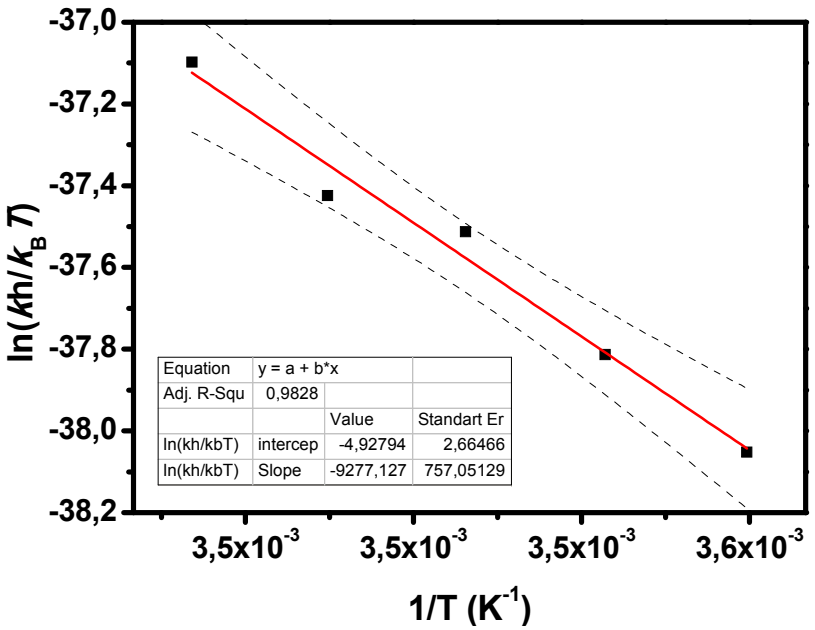

Supplementary Figure 15. Changes in the absorbance of **1** monitored at λ = 470 nm during the thermal helix inversion step from metastable **1** to stable **1** at various temperatures in chloroform. The rate constant (k) was obtained by fitting to the mono-exponential decay equation:$A=Y_0+A_0e^{-kt}$ using Origin software (top), Eyring plot analysis of thermal isomerization step from metastable **1** to stable **1** in chloroform. Thermodynamic parameters of the transition state were obtained by fitting the linearized form of the Eyring equation using Origin software and the results are summarized in the Table S1. Dashed lines indicate 95% confidence intervals.

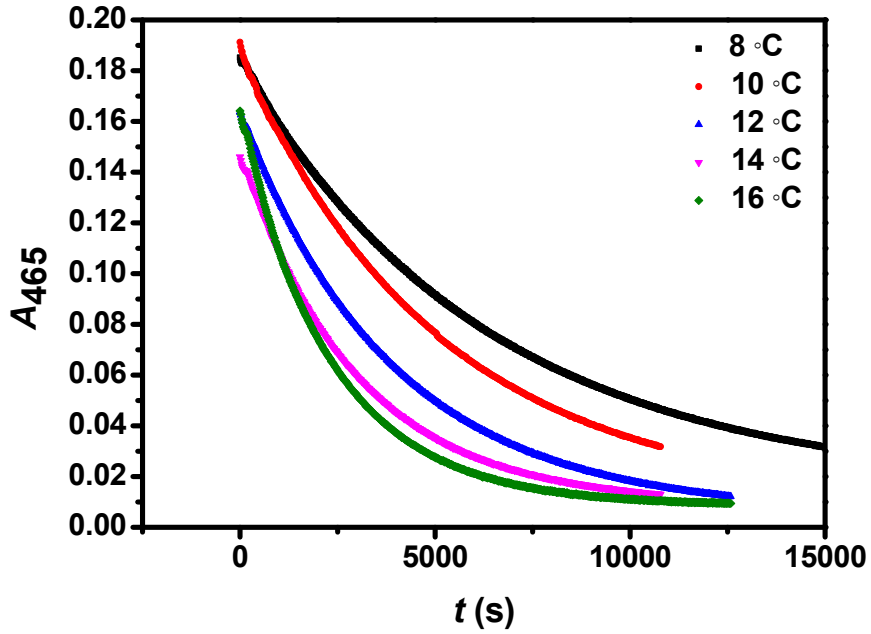

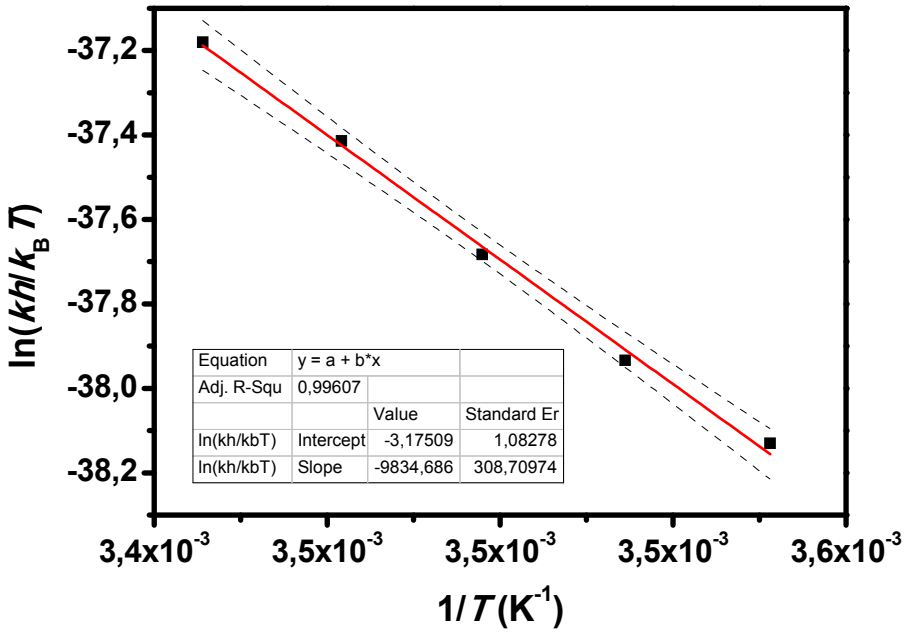

Supplementary Figure 16. Changes in the absorbance of **1** monitored at λ = 465 nm during the thermal helix inversion step from metastable **1** to stable **1** at various temperatures in heptane. The rate constant (k) was obtained by fitting to the mono-exponential decay equation: $A=Y_0+A_0e^{-t/k}$ using Origin software (top), Eyring plot analysis of thermal isomerization step from metastable **1** to stable **1** in hepatne. Thermodynamic parameters of the transition state were obtained by fitting fitting the linearized form of the Eyring equation using Origin software and the results are summarized in the Table S1. Dashed lines indicate 95% confidence intervals.

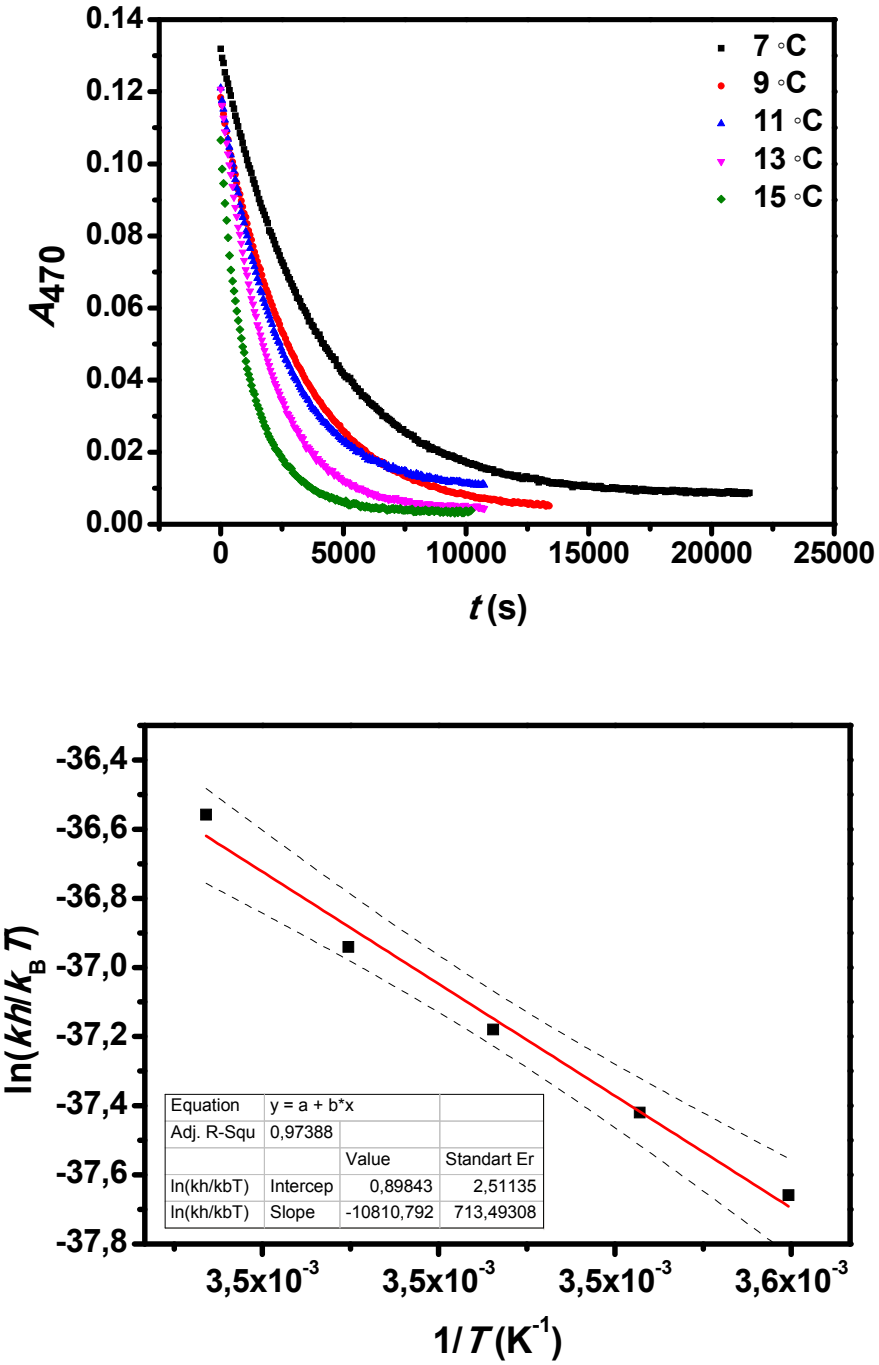

Supplementary Figure 17. Changes in the absorbance of **1** monitored at λ = 470 nm during the thermal helix inversion step from metastable **1** to stable **1** at various temperatures in DMF. The rate constant (k) was obtained by fitting to the mono-exponential decay equation: $A=Y_0+A_0e^{-t/k}$ using Origin software (top), Eyring plot analysis of thermal isomerization step from metastable **1** to stable **1** in DMF. Thermodynamic parameters of the transition state were obtained by fitting the linearized form of the Eyring equation using Origin software and the results are summarized in the Table S1. Dashed lines indicate 95% confidence intervals.

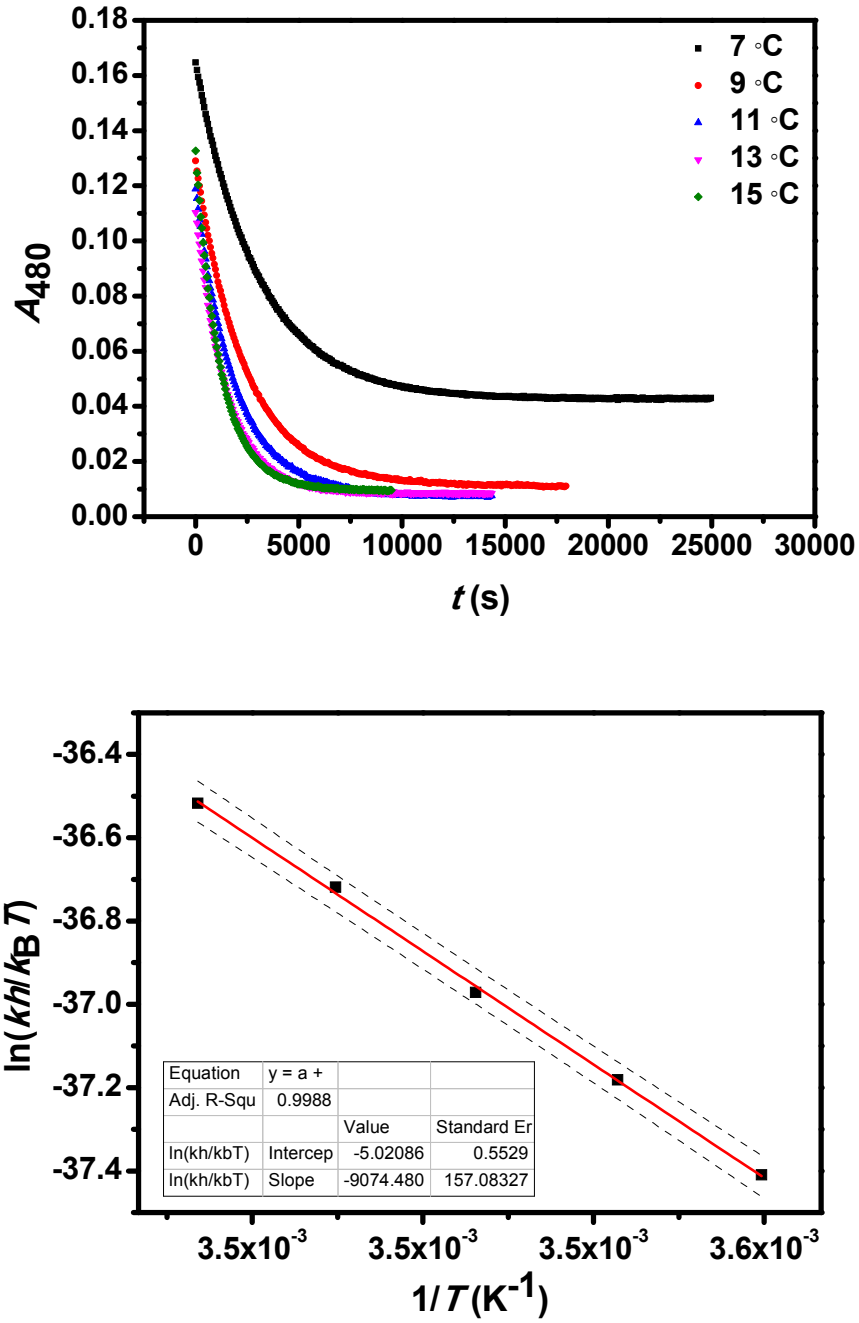

Supplementary Figure 18. Changes in the absorbance of $\mathbf{1H_2}^{2+}$ monitored at λ = 470 nm during the thermal helix inversion step from metastable $\mathbf{1H_2}^{2+}$ to stable $\mathbf{1H_2}^{2+}$ at various temperatures in DMF. The rate constant (k) was obtained by fitting to the mono-exponential decay equation: $A=Y_0+A_0e^{-t/k}$ using Origin software (top), Eyring plot analysis of thermal isomerization step from metastable **1** to stable **1** in DMF. Thermodynamic parameters of the transition state were obtained by fitting the linearized form of the Eyring equation using Origin software and the results are summarized in the Table S1. Dashed lines indicate 95% confidence intervals.

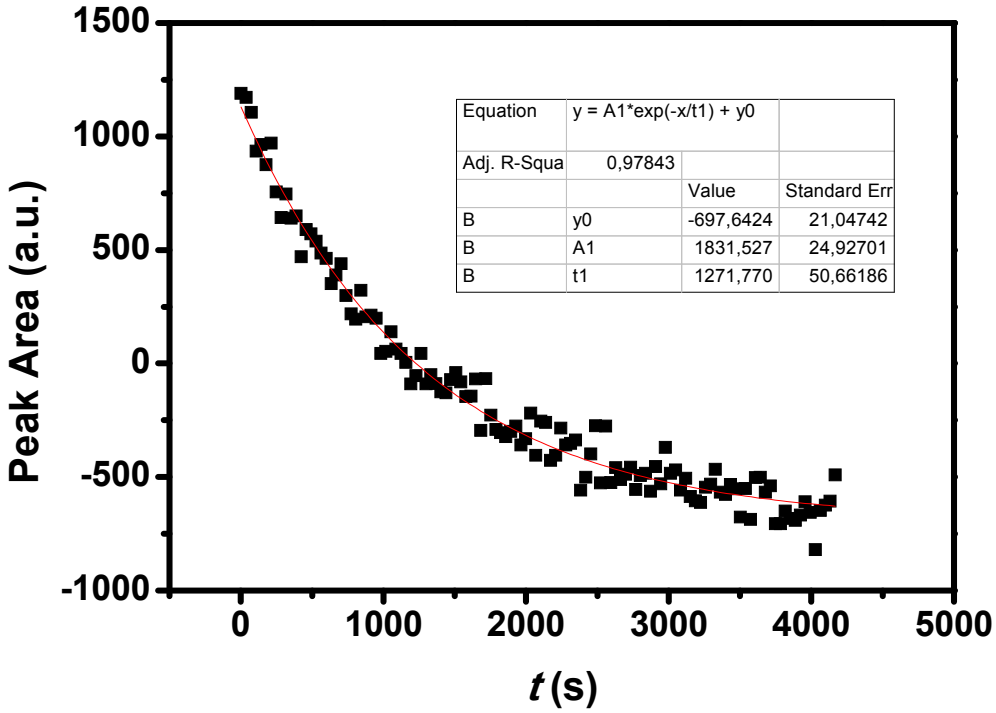

Supplementary Figure 19. Changes in the area of the peak corresponding to the metastable isomer of **1** monitored by Raman Spectroscopy (785 nm, 50 mW laser, 30s intervals) during the thermal helix inversion step from metastable **1** to stable **1** at room temperature in chloroform. The rate constant (k) was obtained by fitting to the mono-exponential decay equation: $A=Y_0+A_0e^{-t/k}$ using Origin software. The measurement was repeated four time and averaged to calculate Gibbs free energy, and error was estimated as 95% confidence interval calculated from variance of the obtained values.

Supplementary Table 1. Values of k and corresponding values of Gibbs free energy obtained from Raman spectra in $CHCl_3$ solution

k (20 °C) (s^{-1})	$\Delta^{\ddagger}G$ (20 °C) (kJ mol^{-1})
0.000786	89.18
0.000913	88.81
0.000887	88.88
0.000922	88.78

Table S2. Summary of the thermodynamic parameters of the transition state for the thermal isomerization of **1** and $\mathbf{1}H_2^{2+}$ in various solvents.

Solvent	$\Delta^{\ddagger}G$ (20 °C) (kJ mol^{-1})	$\Delta^{\ddagger}H$ (20 C) (kJ mol^{-1})	$\Delta^{\ddagger}S$ (20 °C) (J mol K^{-1})	$t_{1/2}$ (min.)
Chloroform	89.1±0.7	76.8±2.1	-42.3±7.4	15
Heptane	89.5±0.2	81.9±2.2	-26.1±7.8	7
DMF	87.7±0.6	89.4±2.5	5.7±8.7	8
DMF $\mathbf{1}H_2^{2+}$	87.7±0.2	75.4±2.0	-41.8±7.2	8

Errors of the Gibbs free energy were estimated as 95% confidence intervals, errors of entropy and enthalpy were derived from the fit.

9. NMR Studies

NMR studies of 1 in solution

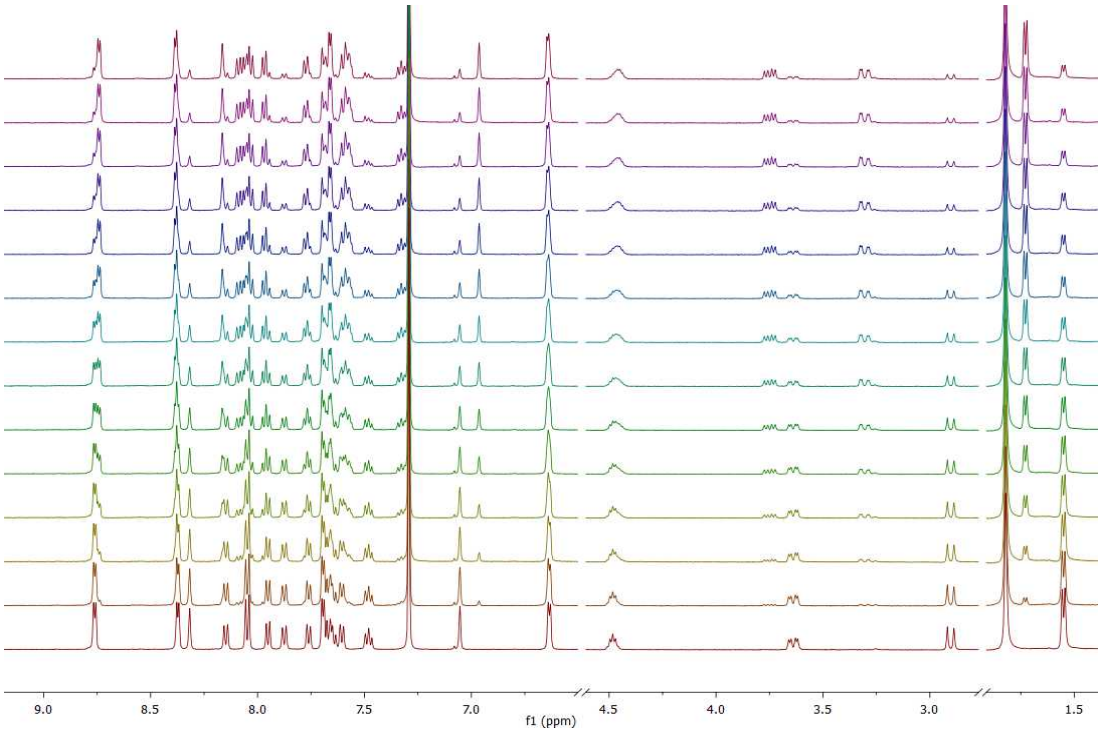

Supplementary Figure 20. Changes in ^{1}H NMR spectrum of **1** upon irradiation with 395 nm UV light at −30 °C in $CDCl_3$.

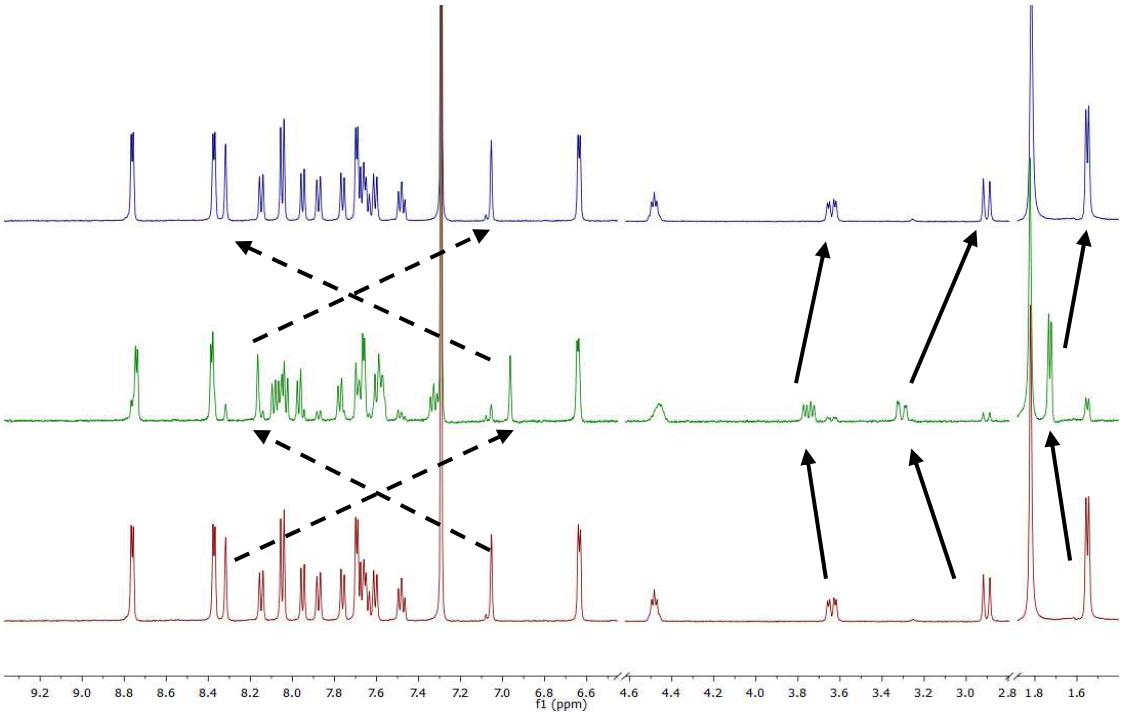

Supplementary Figure 21. Comparison of the ^{1}H NMR (500 MHz) spectra of stable **1** (red bottom spectra), PSS mixture (green, middle spectra) and the PSS mixture kept in the dark at room temperature overnight. (THI) (purple spectra, top) at −30 °C in $CDCl_3$. A PSS ratio of 83:17 (metastable:stable) was determined by integration of the aliphatic signals of the metastable form and stable form.

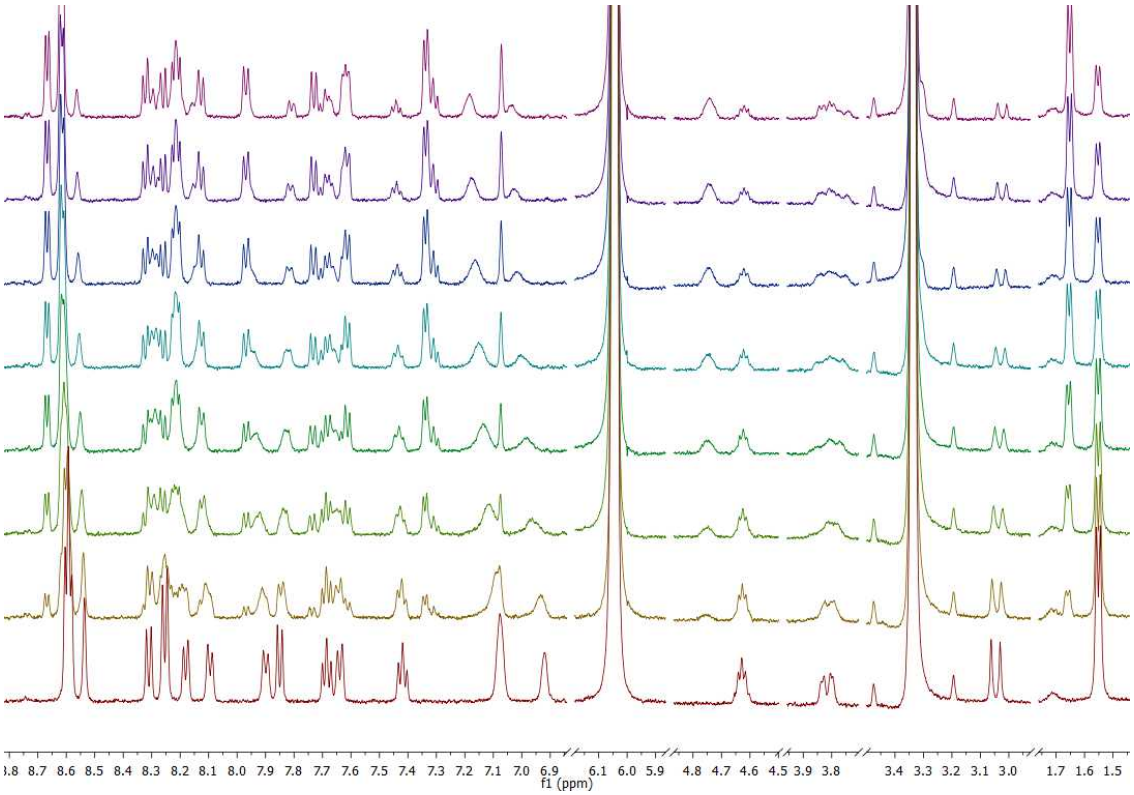

Supplementary Figure 22. Changes in ^{1}H NMR (500 MHz) spectra of protonated **1** upon irradiation with 395 nm UV light at −30 °C in d_4-MeOH.

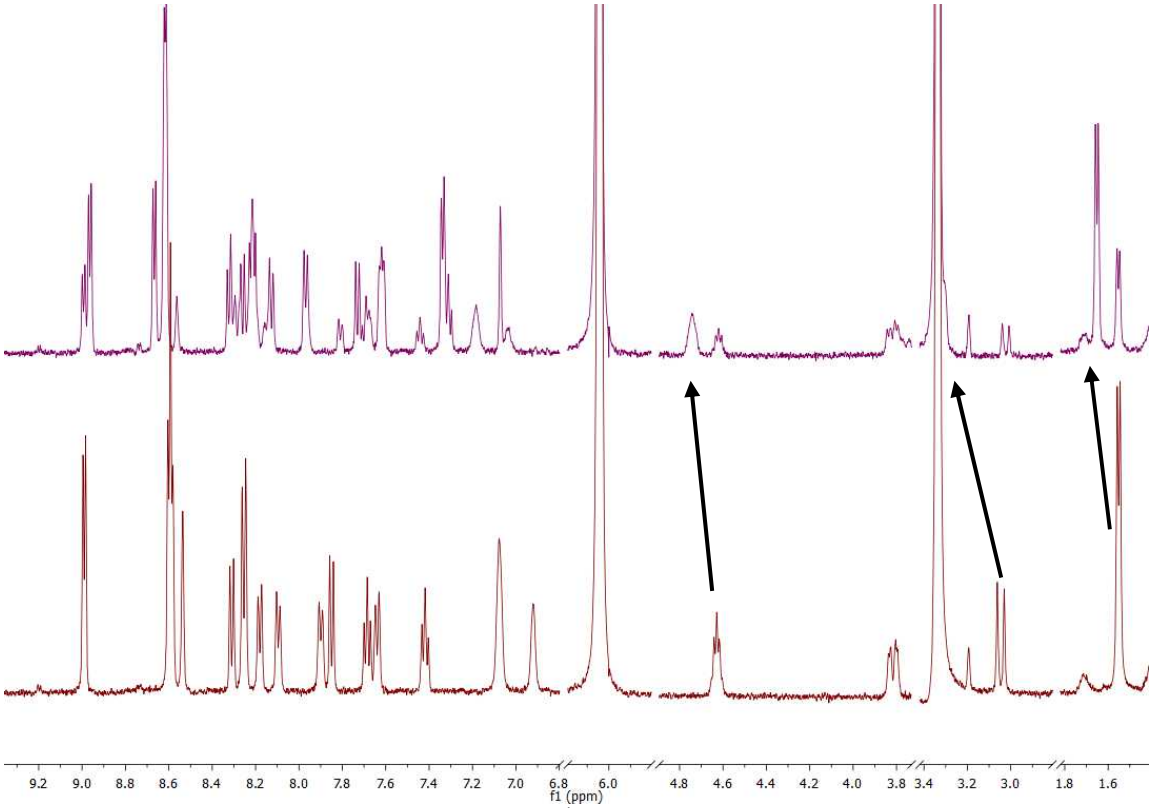

Supplementary Figure 23. Comparison of ^{1}H NMR (500 MHz) spectra of protonated stable **1** (red, bottom spectra) and PSS mixture (purple, top spectra) at −30 °C in d_4-MeOH. A PSS ratio of 68:32 (metastable:stable) was determined by integration of the aliphatic signals of metastable form and stable form.

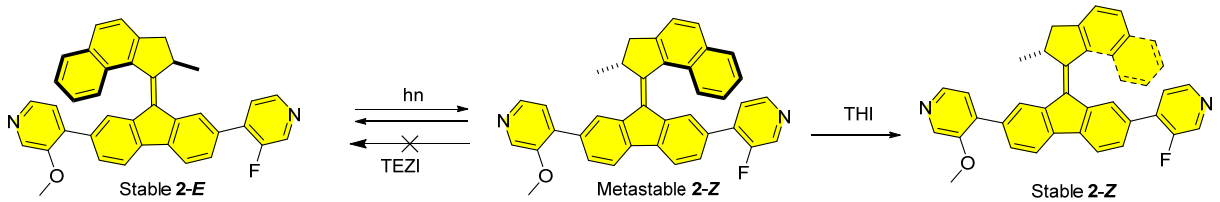

Supplementary Figure 24. In order to exclude the possible thermal *E*/*Z* (TEZI)[11–13] isomerization pathway of the metastable isomer, the photochemical and thermal isomerization of model compound **2** and its protonated form $\mathbf{2}H_2^{2+}$ was studied by ^{1}H NMR spectroscopy.

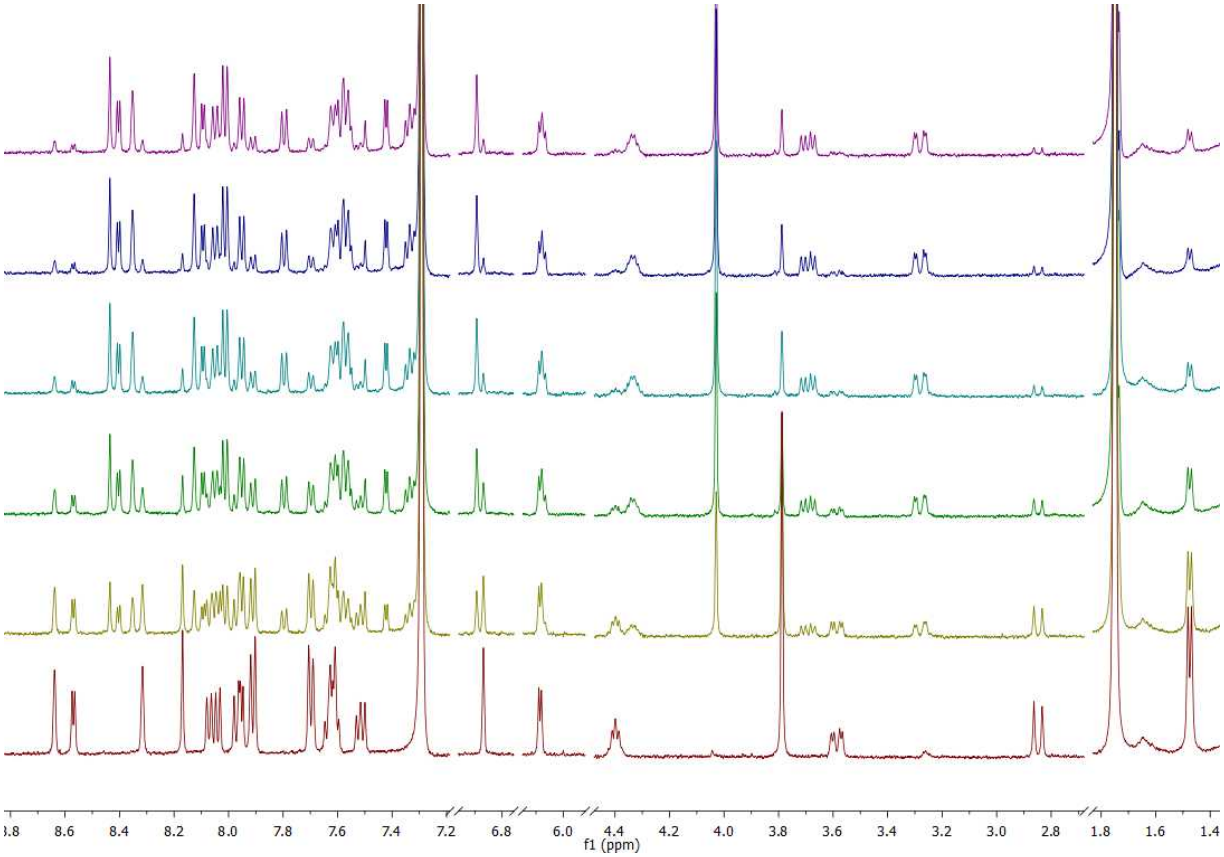

Supplementary Figure 25. Changes in ^{1}H NMR (500 MHz) spectra of **2-*E*** upon irradiation with 395 nm UV light at −30 °C in $CDCl_3$.

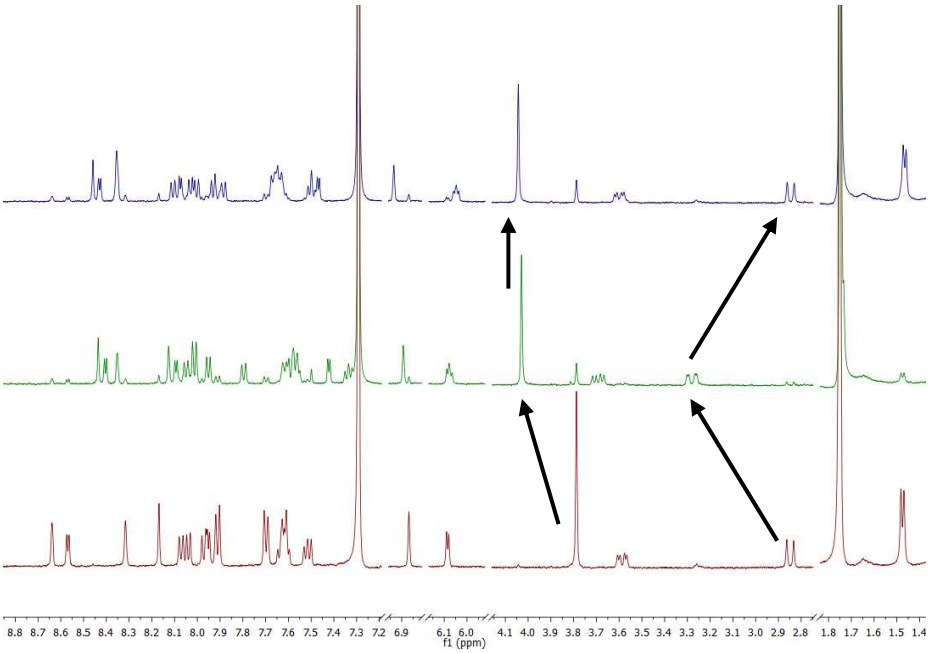

Supplementary Figure 26. Comparison of ^{1}H NMR spectra (500 MHz) of stable **2-*E*** (red bottom spectra), PSS mixture (green, middle spectra) and PSS mixture kept in the room temperature in dark overnight (THI) (purple spectra, top) at −30 °C in $CDCl_3$. A PSS ratio of 87:13 (**2-*Z*** metastable:**2-*E*** stable) was determined by integration of the aliphatic signals of the metastable form and stable form. Ratio of **2-*Z*** stable:**2-*E*** stable (87:13) after THI isomerization of **2-*E*** metastable was determined by integration of the signals of the methoxy group of the corresponding isomers. As it is evident from the ratios of **2-*Z*** metastable:**2-*E*** stable (87:13) and **2-*Z*** stable:**2-*E*** stable (87:13), heating of the sample to room temperature resulted in full conversion of **2-*Z*** metastable:**2-*E*** stable, thereby completely excluding the TEZ isomerization path.

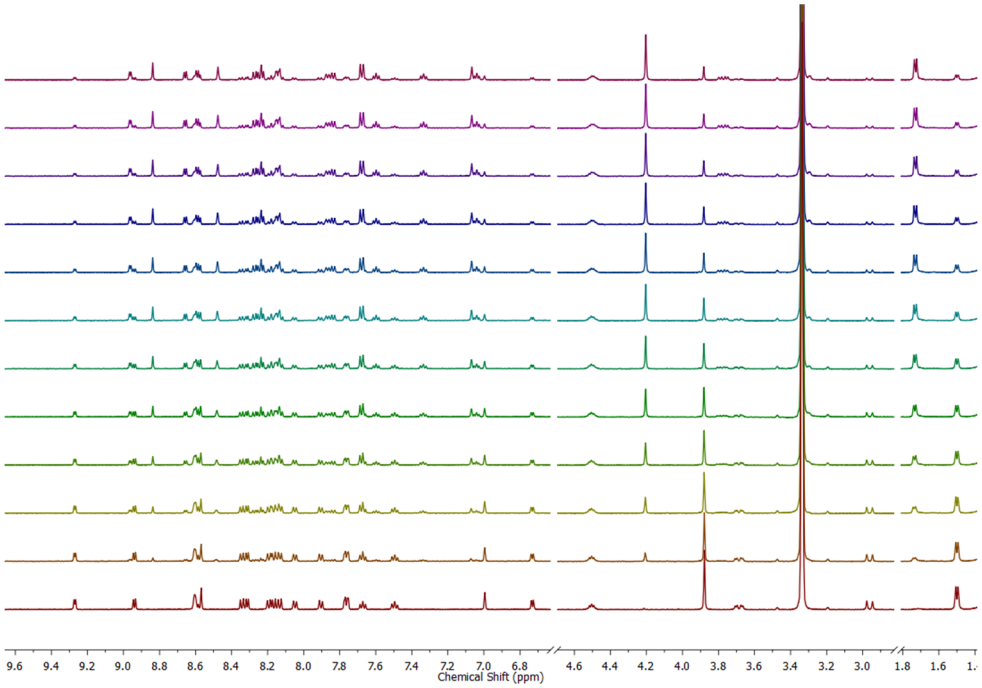

Supplementary Figure 27. Changes in ^{1}H NMR (500 MHz) spectra of **2-*E***H_2^{2+} upon irradiation with 395 nm UV light at −30 °C in d_4-MeOH.

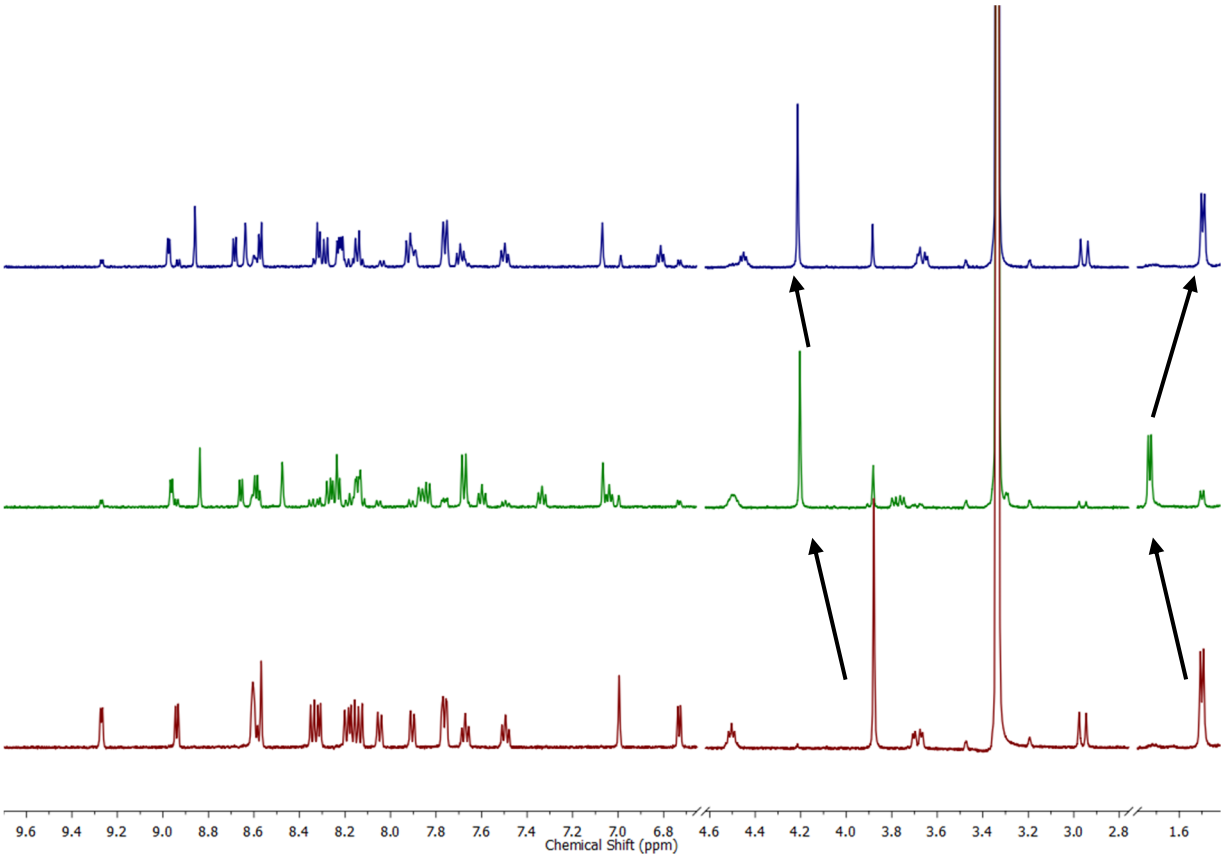

Supplementary Figure 28. Comparison of ^{1}H NMR (500 MHz) spectra of stable **2-*E*H$_2^{2+}$** (red bottom spectra), PSS mixture (green, middle spectra) and PSS mixture kept in the room temperature in dark overnight (THI) (blue spectra, top) at −30 °C in d_4-MeOH. A PSS ratio of 79:21 (protonated **2-*Z*** metastable:**2-*E*** stable) was determined by integration of the aliphatic signals of metastable form and stable form. Ration of protonated **2-*Z*** stable:**2-*E*** stable (79:21) after THI isomerization of protonated **2-*Z*$_{meta}$** was determined by integration of the signals of the methoxy group of the corresponding isomers. As it is evident from the ratios of protonated **2-*Z*** metastable:**2-*E*** stable (79:21) and protonated **2-*Z*** stable:**2-*E*** stable (79:21), heating of the sample to room temperature resulted in full conversion of protonated **2-*Z*** metastable into **2-*E*** stable, thereby completely excluding the TEZ isomerization path.

10. Raman spectroscopy of 2 in solution

The unidirectional rotary cycle of the molecular motors **2-*E*** and **2-*Z*** in $CHCl_3$ solution was followed by Raman probe spectroscopy (785 nm, 50 mW). First calibration curve, for the **2-*Z***, was made by measuring Raman spectra of $CHCl_3$ solutions with varying concentrations of **2-*E*** and **2-*Z***. Solutions used for the calibration curve, were prepared by mixing appropriate volume of stock solutions of **2-*E*** (3.0 mg·ml^{-1}) and **2-*Z*** (3.0 mg·ml^{-1}) and diluting to a final concentration of 1.5 mg·ml^{-1}. The calibration curve is based on the ratio of intensities at 1297 and 1283 cm^{-1} with a linear fit using Origin^{TM} (Supplementary Figures 29, 30).

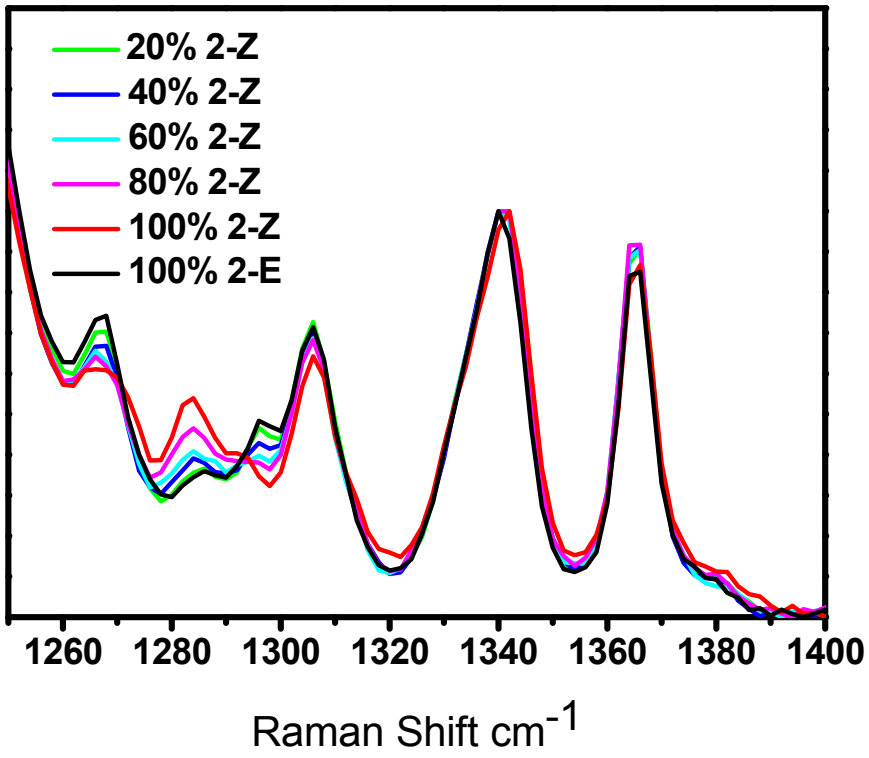

Supplementary Figure 29. Comparison of Raman (785 nm, 50 mW) spectra of various mole fraction mixtures of **2-*E*** and **2-*Z*** solutions (total concentration 1.5 mg mg·ml^{-1})

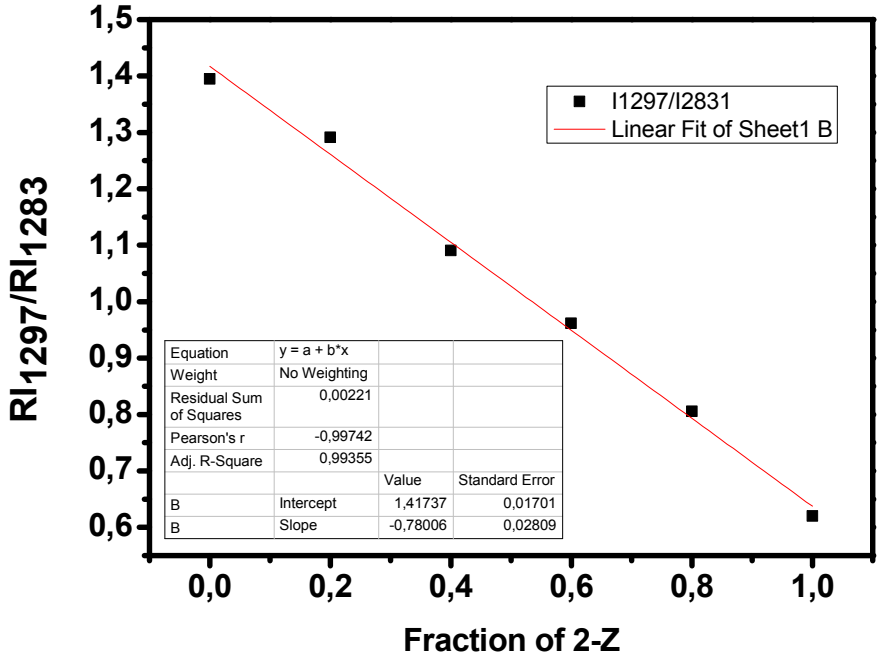

Supplementary Figure 30. Calibration curve obtained from Raman spectra

Solutions of **2-*E*** or **2-*Z*** (0.7 ml, 1.5 mg·ml^{-1}, $CHCl_3$, black lines, Supplementary Figures 31, 34 respectively) were irradiated at 395 nm for 5 h at -25 °C to reach their PSS (red lines, Supplementary Figures 31, 34 respectively). Raman spectra were recorded at PSS (at -25 °C) and after being held at RT in the dark overnight to allow for THI to proceed to completion (red and blue lines, Supplementary Figures 31, 34 respectively). The ratio of **2-*E*** or **2-*Z*** presnet in the mixtures after THI were determined from the calibration curve and validated by ^{1}H NMR spectra of the mixtures after removal of solvent (Supplementary Figures 33, 36 respectively).

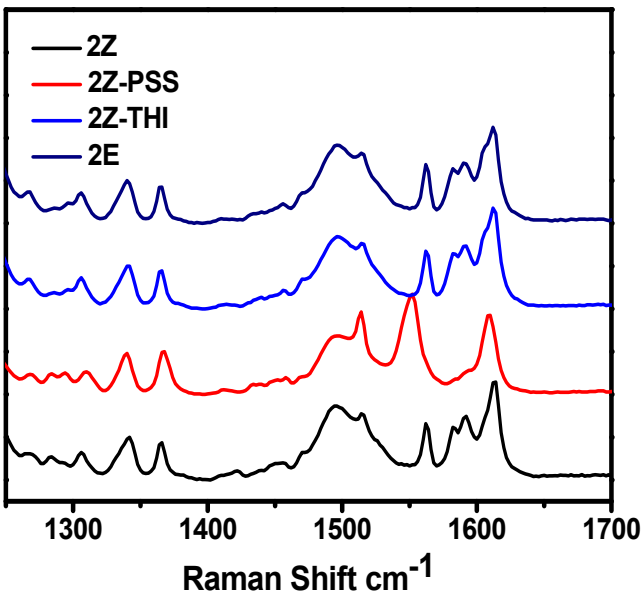

Supplementary Figure 31. Comparison of Raman spectra of **2-*E*** (black line), after irradiation at 395 nm for 5 h at -25 °C (PSS mixture, red line), and after THI (blue line). The ratio of **2-*E*/2-*Z*** was calculated to be 16/84 from the calibration curve, which is in agreement with the ratio determined by ^{1}H NMR spectroscopy (**2-*E*/2-*Z*** = 19/81) from the studied sample. The spectrum of **2-*Z*** (navy line) is shown for comparison.

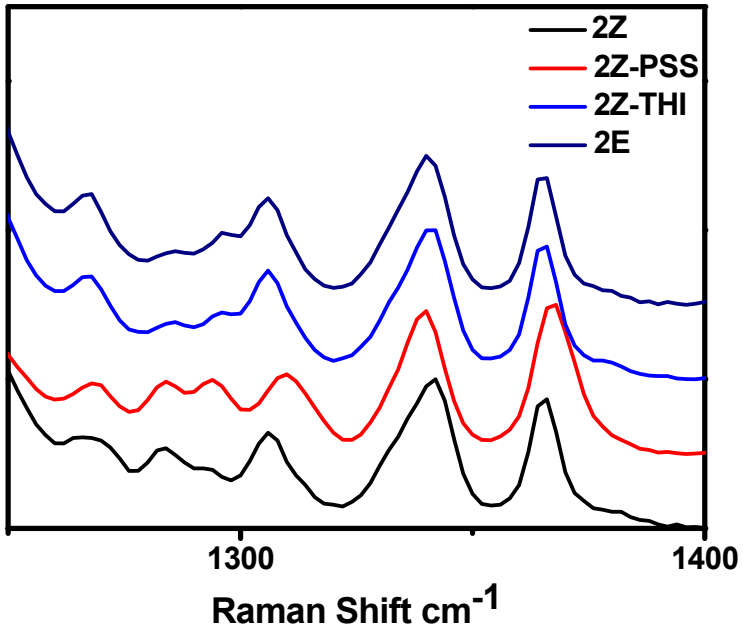

Supplementary Figure 32. Expansion of the Raman spectra from Supplementary Figure 31 in the region 1250 – 1450 cm^{-1}.

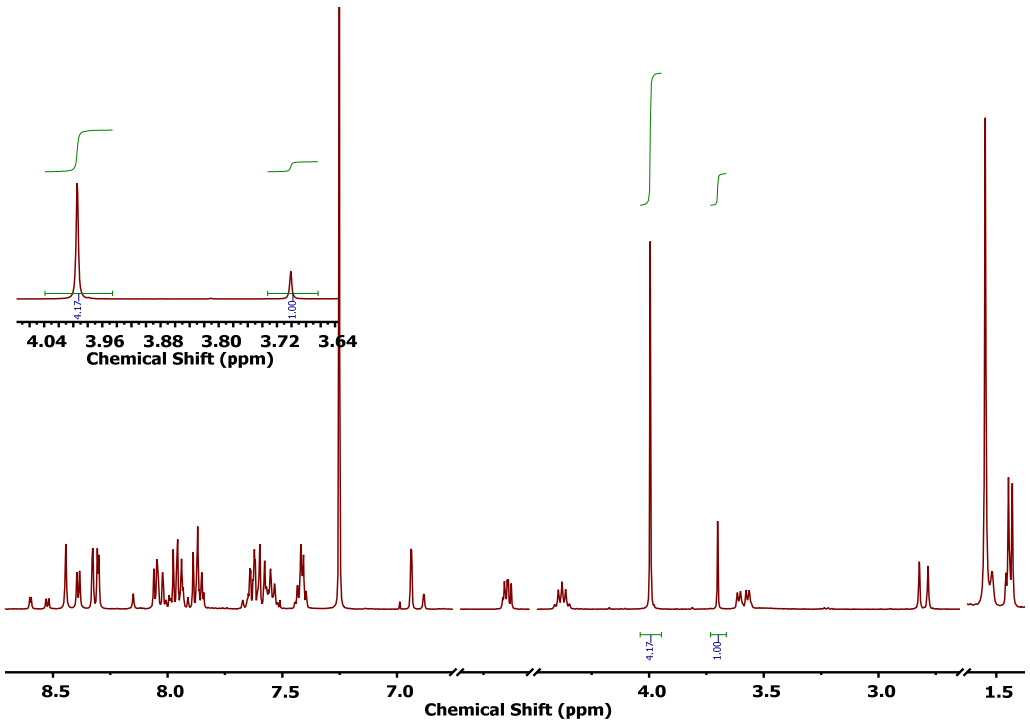

Supplementary Figure 33. ^{1}H NMR spectra of the sample of **2-*E***, used for Raman studies, after irradiation at 395 nm and subsequent THI.

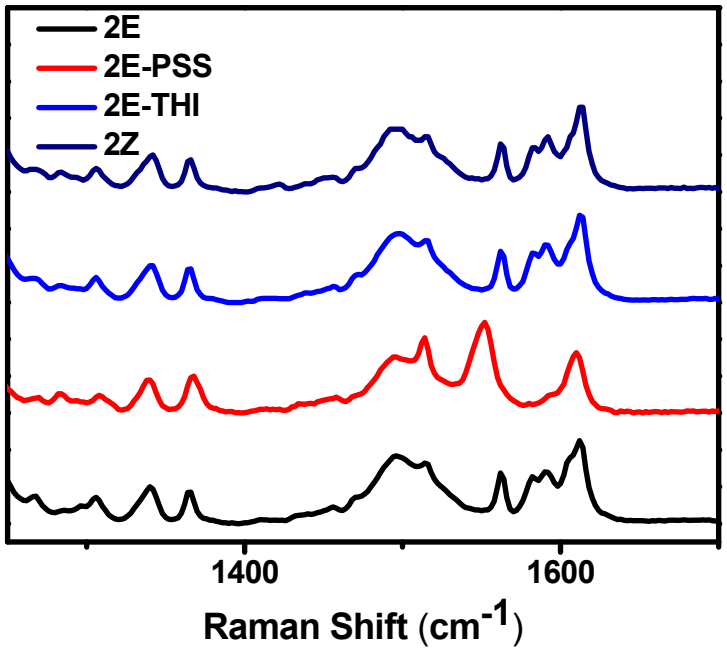

Supplementary Figure 34. Comparison of Raman spectra of **2-*Z*** (black line), after irradiation at 395 nm for 5 h at -25 °C (PSS mixture, red line), and after THI (blue line). The ratio of **2-*Z*/2-*E*** was calculated to be 23/77 from the calibration curve, which is in agreement with the ratio determined by ^{1}H NMR spectroscopy (**2-*Z*/2-*E*** = 25/75) from the studied sample. The spectrum of **2-*E*** (navy line) is shown for comparison.

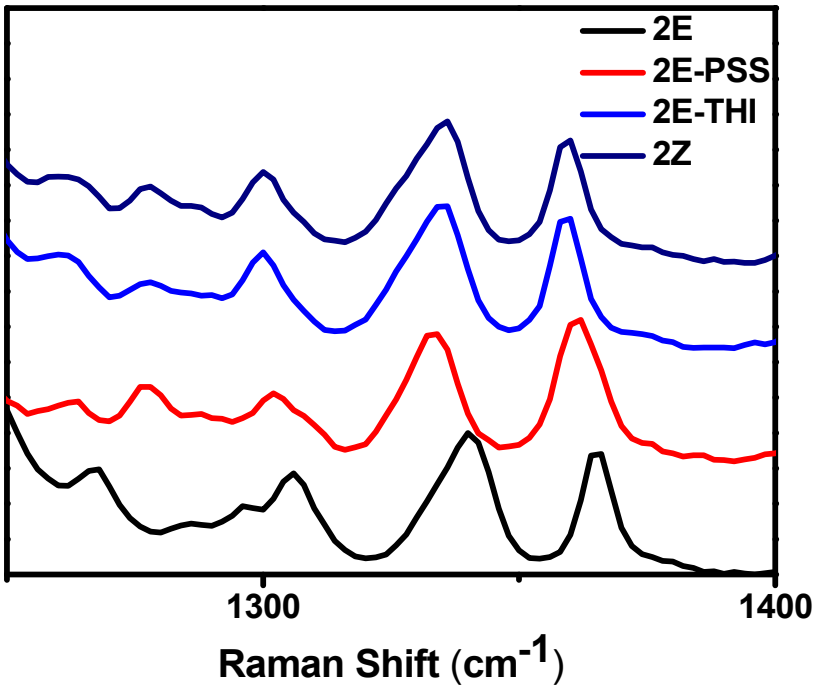

Supplementary Figure 35. Expansion of the Raman spectra from Supplementary Figure 34 in the region 1250 – 1450 cm^{-1}.

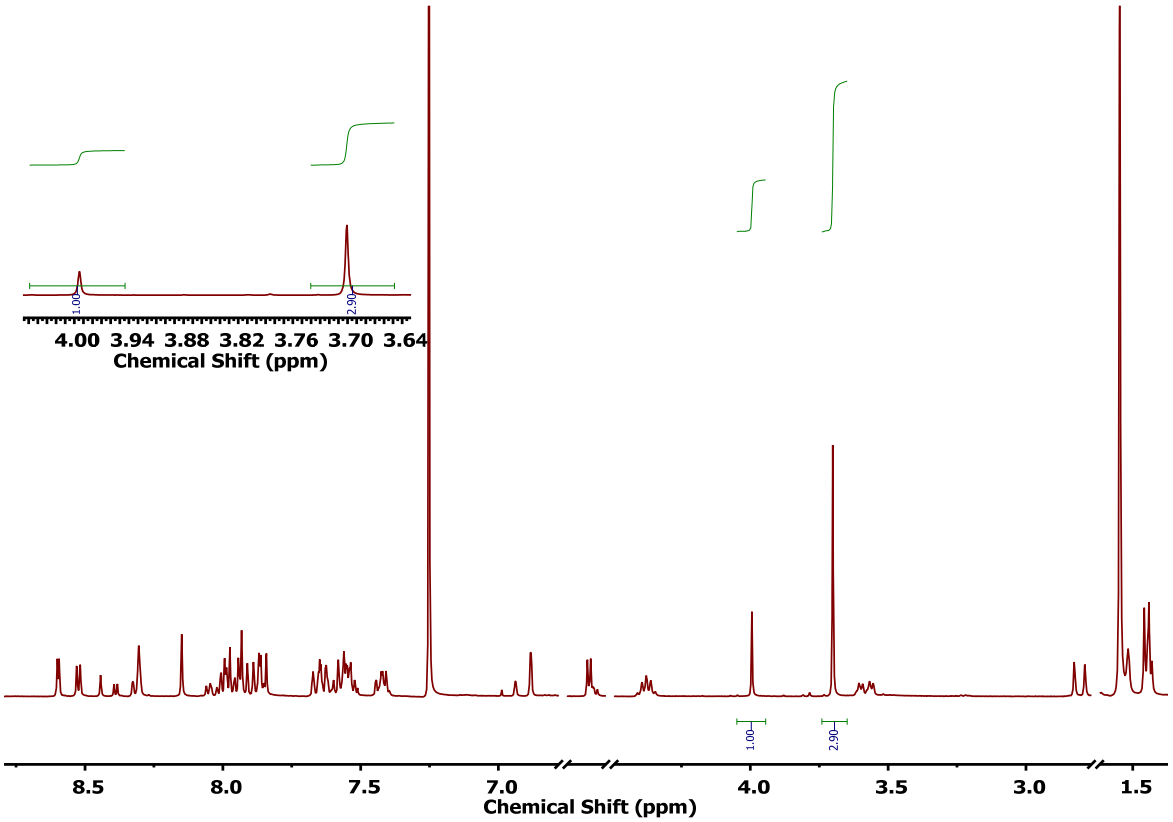

Supplementary Figure 36. ^{1}H NMR spectra of the sample of **2-*Z***, used for Raman studies, after irradiation at 395 nm and subsequent THI.

11. Local Heating Evaluation

It was found that in order to get a reproducible value for the rate constant, the laser power for the Raman measurement had to be carefully set. When using 50 mW laser power, the observed rate constant was dependent on the time intervals between every recording of the Raman spectrum, with shorter time intervals giving higher observed rate constants) (Supplementary Figure 37-39). Apparently, the measurement of the Raman spectra causes local heating in the crystal, leading to an incorrect observed value for the rate constant. However, using either 75%, 50% or 30% of the laser power and thereby reducing the effects of local heating, the observed rate constant was the same considering a small margin of error (15%) and not dependent on the time interval between the measurements (Supplementary Figure 40-43).

Kinetics with 50 mW Laser Power

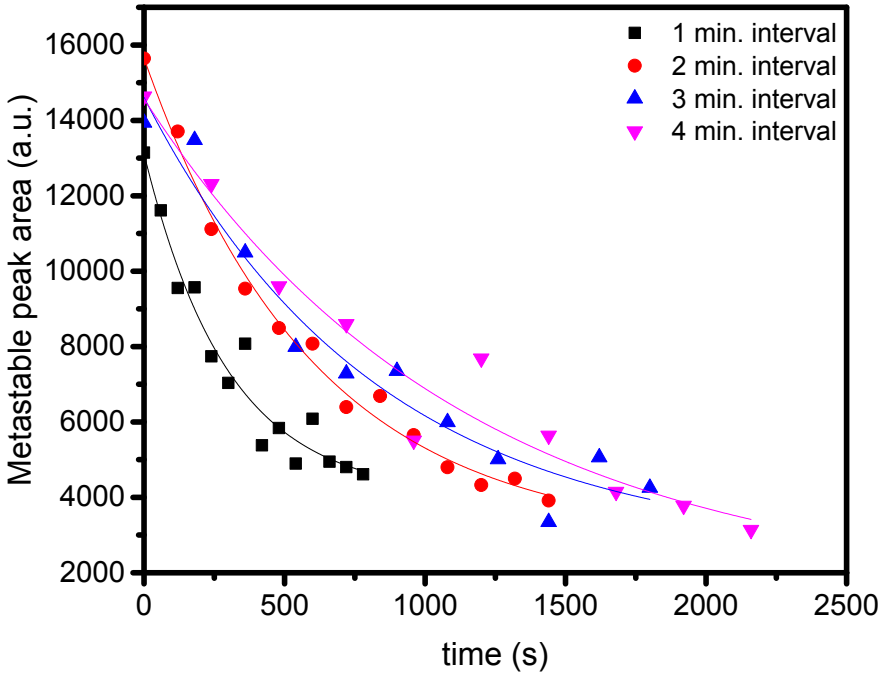

Supplementary Figure 37. Comparison of the exponential decay of the area of the band corresponding to metastable isomer of **1** in MOF recorded with 100% laser power with different (1 (black squares) 2 (red rectangles), 3 (blue triangles), 4 (purple rectangles) minutes) time intervals between recording consecutive Raman spectra (30 s exposure to the laser time, real experiment time). Rate constants were obtained by fitting the data to the exponential decay $I=I_0e^{-kt}+B$ using Origin software.

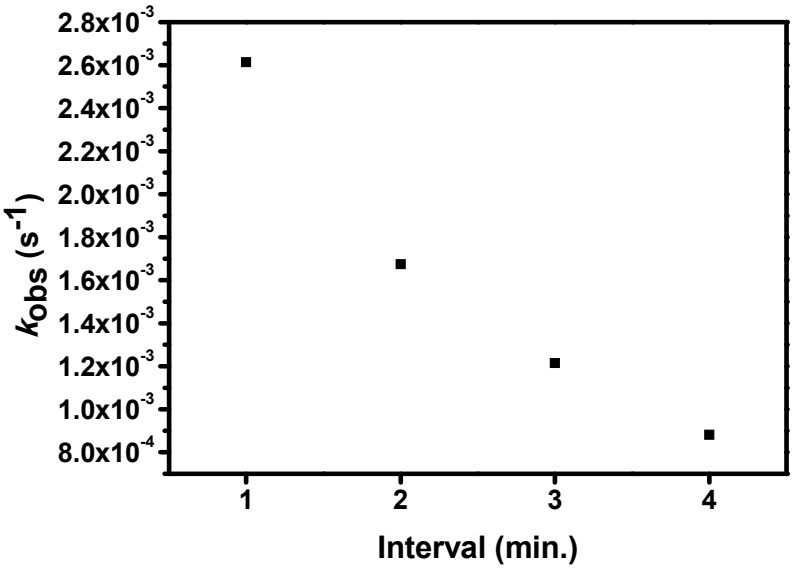

Supplementary Figure 38. Comparison of rate constants obtained from Raman measurements with different time intervals (30 s exposure time).

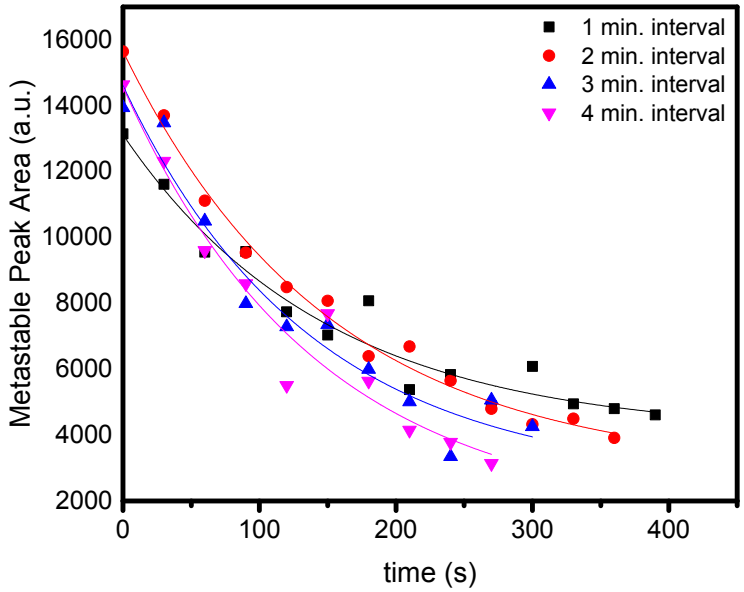

Supplementary Figure 39. Comparison of the exponential decay of the area of the band corresponding to metastable isomer of **1** recorded with 100% laser power with different (1 (black squares) 2 (red rectangles), 3 (blue triangles), 4 (purple rectangles) minutes) time intervals between recording subsequent Raman spectra (30 s exposure to the laser time) Time axis is set as a cumulated exposure to laser time. The fact that the rate of the decay is the same and independent of the interval indicates that metastable isomer undergoes THI step much faster during exposure to Raman laser than between the consecutive measurements. The measurement of the Raman spectrum with 100% laser power results in local heating of the sampling area, thereby increasing the observed rate of the THI with respect to the expected rate from the bulk sample temperature.

Kinetics with different Laser Power

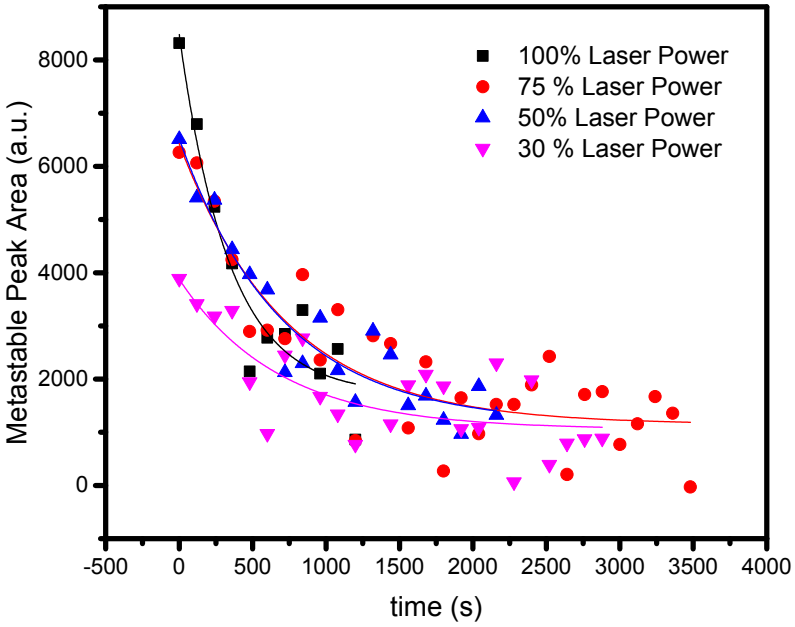

Supplementary Figure 40. Comparison of the exponential decay of the area of the band corresponding to metastable isomer of **1** in MOF recorded with different laser power (100% (black squares) 75% (red rectangles), 50% (blue triangles), 30% (purple rectangles)) 1 min. intervals between recording consequent Raman spectra (30 s exposure to the laser) Rate constants were obtained by fitting exponential decay $I=I_0e^{-kt}+B$ using Origin software.

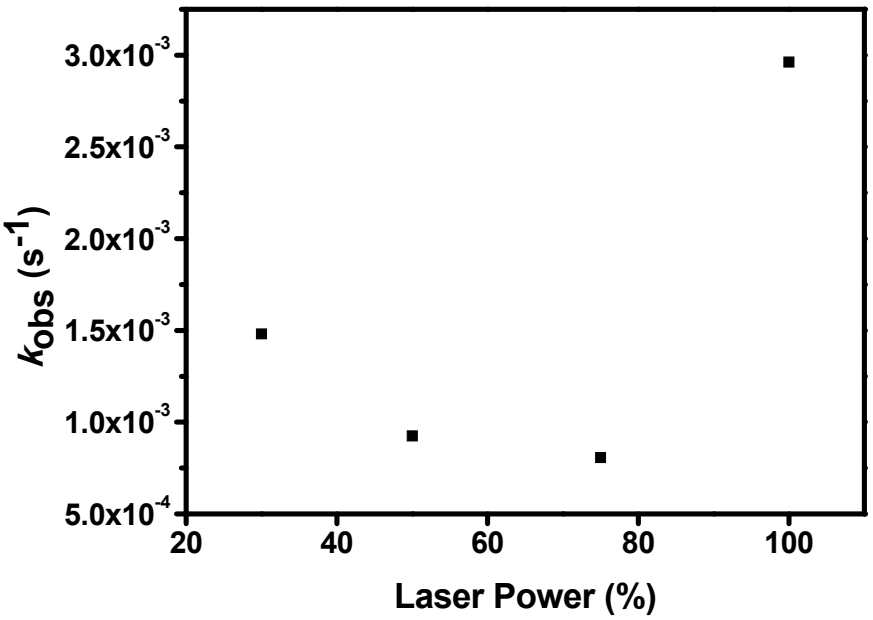

Supplementary Figure 41. Comparison of rate constants of **1** in MOF using 30, 50, 75 and 100% 50 mW 785 nm laser power (30 s exposure time, spectra recorded every 2 min.). Decreasing laser power to 75% of its nominal value results in lowering the observed *k*, further lowering of the laser power does not lead to further lowering of observed *k* indicating that local heating effect is only observed when 100% laser power is used.

Kinetics with 75% Laser Power

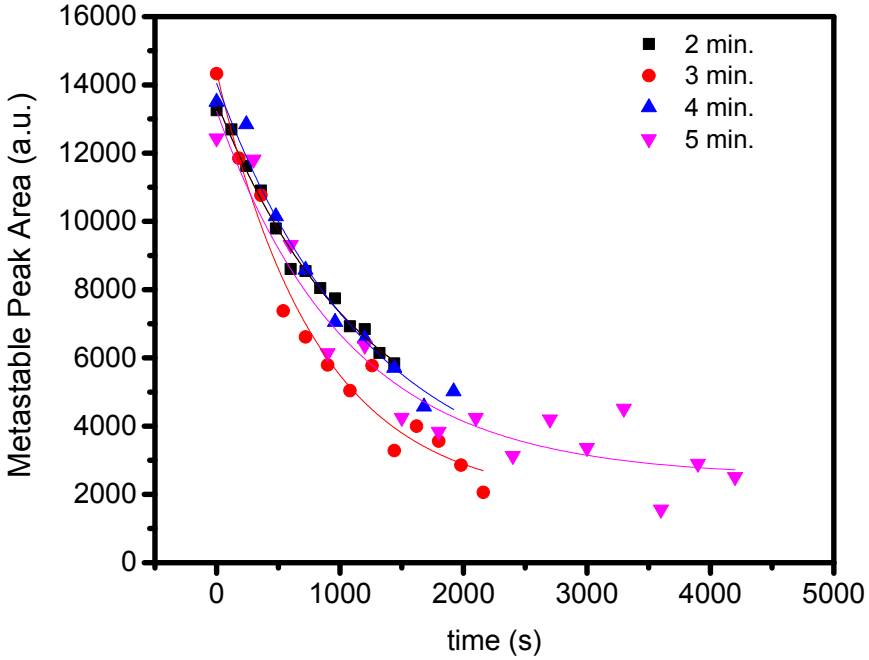

Supplementary Figure 42. Comparison of the exponential decay of the area of the band corresponding to metastable isomer of **1** in MOF recorded with 75% laser power with different (2 (black squares) 3 (red rectangles), 4 (blue triangles), 5 (purple rectangles) minutes) time intervals between recording consequent Raman spectra (30 s exposure to the laser time, real experiment time). Rate constants were obtained by fitting exponential decay $I=I_0e^{-kt}+B$ using Origin software. The values of the rate constant obtained were similar and independent on the interval time, thereby excluding local heating.

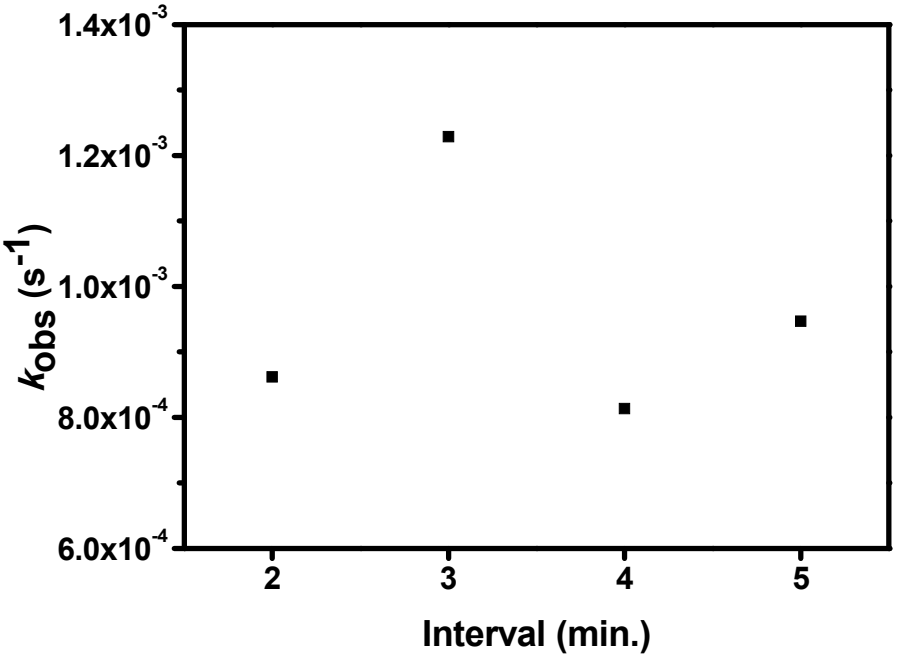

Supplementary Figure 43. Comparison rate constants of **1** in MOF obtained from Raman measurements with different time intervals of **1** in MOF using 75% 50 mW 785 nm laser power (30 s exposure time).

Supplementary Table 3 Values of *k* and corresponding values of Gibbs free energy obtained from Raman spectra in moto-MOF**1** (50 mW laser, 75% power, 40s exposure time) Average value was calculated from measurements done with 2 min. interval and error was estimated as 95% confidence interval calculated from variance of the obtained values.

Entry	k (20 °C) (s^{-1})	$\Delta^{\ddagger}G$ (20 °C) (kJ mol^{-1})	Interval (min.)
1	$8.621 \cdot 10^{-4}$	88.95	2
2	$1.232 \cdot 10^{-3}$	88.08	3
3	$8.135 \cdot 10^{-4}$	89.09	4
4	$9.469 \cdot 10^{-4}$	88.72	5
5	$1.212 \cdot 10^{-3}$	88.12	2
6	$8.694 \cdot 10^{-4}$	88.93	2
7	$1.268 \cdot 10^{-3}$	88.01	2
8	$8.009 \cdot 10^{-4}$	89.13	2
Average	$(1.0 \pm 0.3) \cdot 10^{-3}$	88.6±0.7	2

Possible effects of the viscosity of the MOF confined solvent

The thermal helix inversion for the molecular motor involves rearrangement of only fraction of the molecule. In the previous reports, we have shown that rotational motion of archetypical 1st generation molecular motor is only marginally dependent on the viscosity (three order of magnitude difference), while motors with long, rigid arms, where the fraction of the molecule involved in THI is higher, showed significant but nevertheless moderate

differences in half-life.[14] In the follow up study, it was demonstrated that the dependence of the rate THI process for 2nd generation molecular motor is independent of the viscosity (over small range of – one order of magnitude – viscosities of solvents) due to, most probably much smaller atomic displacement during THI process.[15] Therefore the possible effects of the confined solvent on the rate of THI step are expected to be marginal within the experimental error.

12. Raman spectroscopy of moto-MOF

Photostationary State in moto-MOF1

A sample of crystals of moto-MOF**1** were placed between two 1 mm quartz slides and sealed with PTFE paste to avoid loss of the solvent and placed in a MicrostatN Oxford Instruments (Supplementary Figure 44) and cooled to -5 °C. The maximum ratio of the photo-generated metastable isomer to the stable isomer was determined from the relative intensities of the representative bands (Supplementary Figure 46).

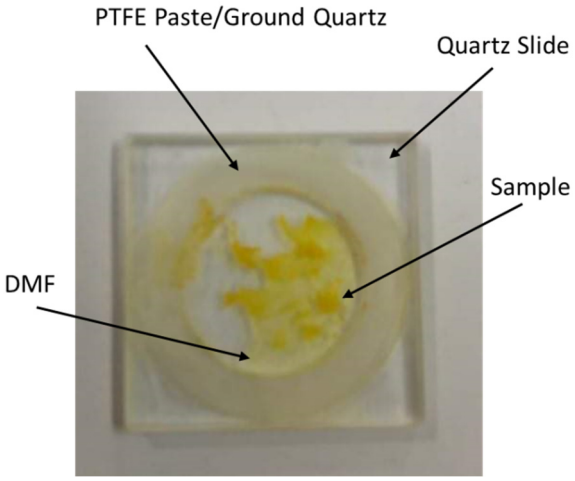

Supplementary Figure 44. Sample preparation for low temperature Raman studies

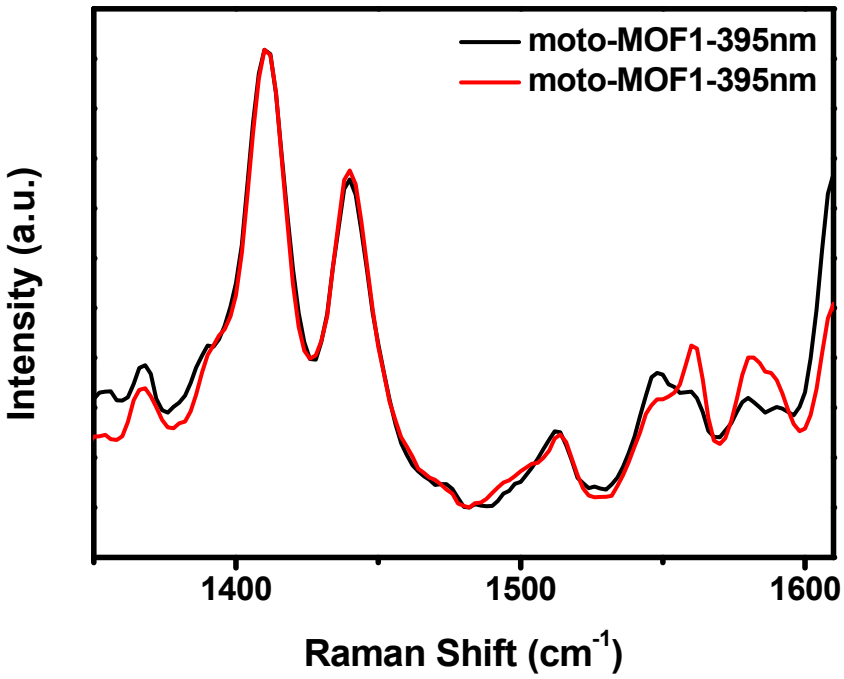

Supplementary Figure 45. Comparison of Raman spectra of moto-MOF**1** crystals of various thicknesses (thinner black spectrum, thicker red spectrum) under continuous irradiation at 395 nm at -5 °C. The maximal ratio of metastable:stable isomer that can be generated in the whole crystal upon irradiation depends of the crystal thickness as the light penetration depth (c.a. 5 μm) is limited by molar absorptivity.

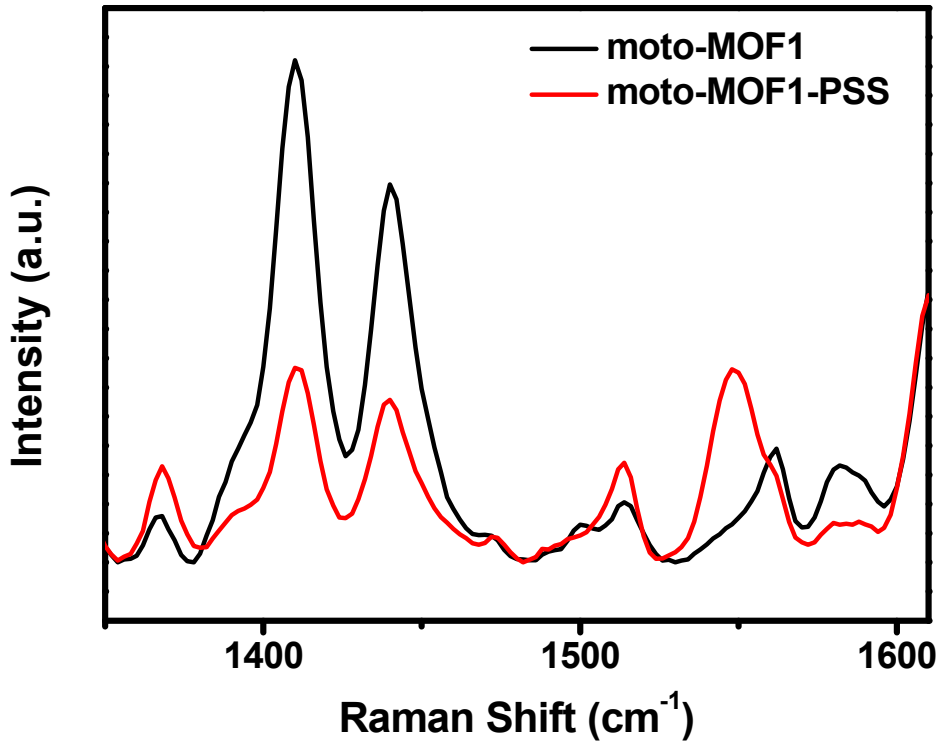

Supplementary Fgiure 46. Comparison of Raman spectra of thin crystal of moto-MOF**1** before (black spectrum) and after irradiation at (395 nm) -5 °C (red spectrum). The ratio of metastable to stable isomer achieved can be estimated from the ratio of intensities of bands at 1550 cm^{-1} (band characteristic of metastable isomer) to bands and 1582 cm^{-1} (c. a. 5) which are similar to the ratio of intensities of these bands in the Raman spectrum of a PSS mixture in $CHCl_3$ (c.a. 5). It can be therefore concluded that depending on the crystal thickness the PSS ratio that can be achieved can be as high as in solution (c. a. 80-70 % of metastable isomer). Bands around 1400 – 1500 cm^{-1} are characteristic of DMF and their intensity varies with time depending on exact position of the confocal volume with respect to the crystal.

Analysis of rotary motion of the molecular motor 2-*E* in moto-MOF2-*E*

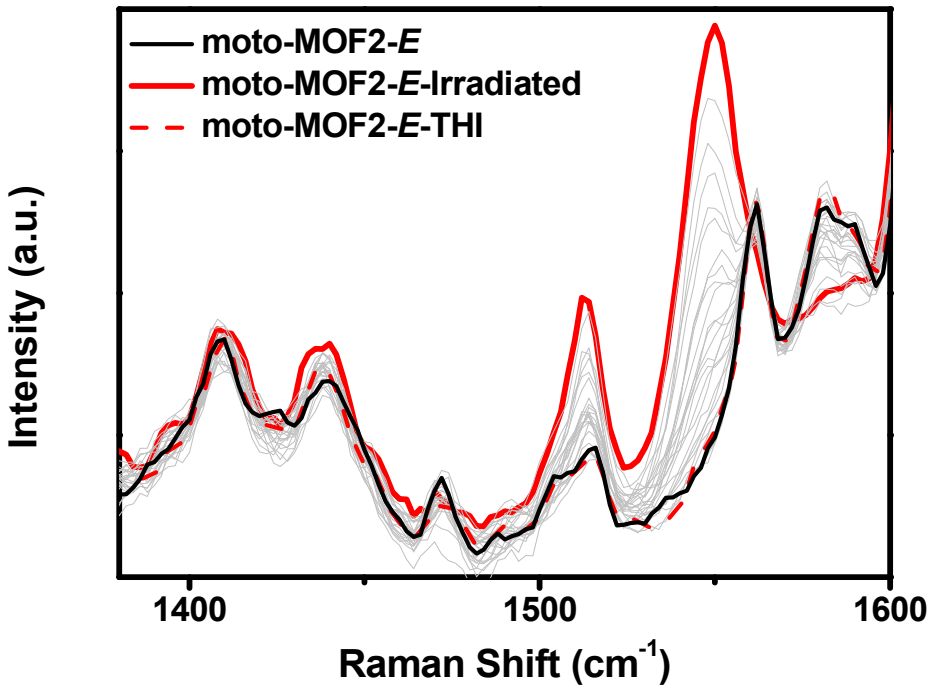

Supplementary Figure 47. Changes in the Raman spectra of moto-MOF**2-*E*** (black line), upon irradiation at 395 nm (red, solid line) and after THI (red, dashed line)

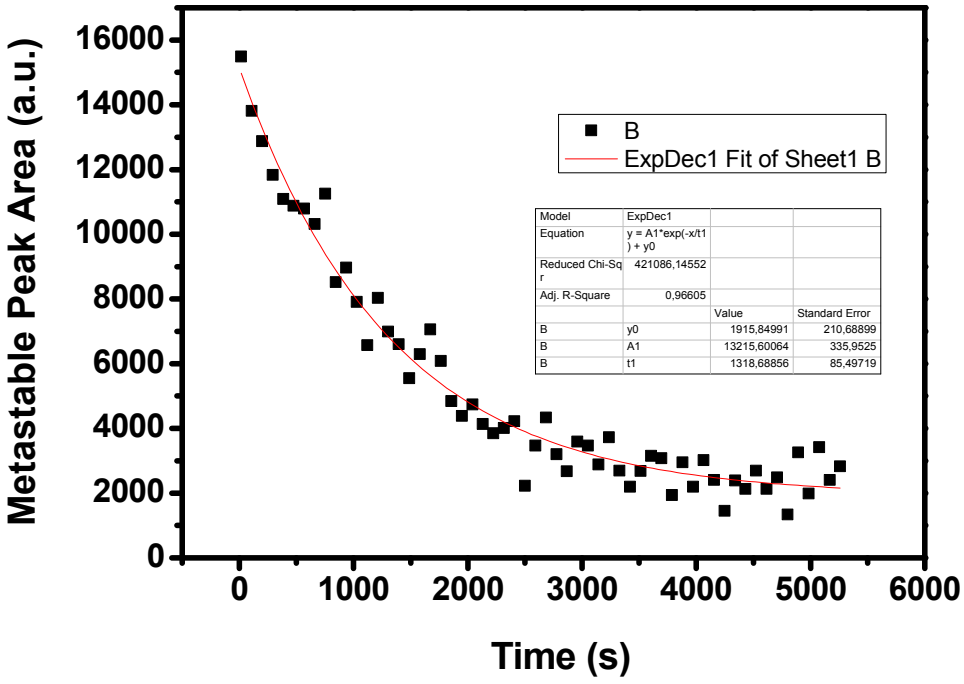

Supplementary Figure 48. Example of the changes in the area of the band corresponding to the metastable isomer (**2-*Z*** metastable) in moto-MOF**2-*E*** followed in time. Spectra were recorded with 75% of laser power (785 nm, 50 mW, 32 s integration time) every 90 s;

Supplementary Table 4 Values of *k* and corresponding values of Gibbs free energy (**2-*Z*** metastable to **2-*Z*** stable) obtained from Raman spectra in moto-MOF**2-*E*** (50 mW laser, 75% power, 32s exposure time). Average value was calculated from measurements done with 90 s. interval and error was estimated as 95% confidence interval calculated from variance of the obtained values. With each measurement fresh sample was used.

Entry	k (20 °C) (s^{-1})	$\Delta^{\ddagger}G$ (20 °C) (kJ mol^{-1})
1	$1.157 \cdot 10^{-3}$	88.23
2	$7.182 \cdot 10^{-4}$	88.23
3	$7.509 \cdot 10^{-4}$	88.73
4	$9.469 \cdot 10^{-4}$	89.40
5	$1.159 \cdot 10^{-3}$	89.29
6	$7.583 \cdot 10^{-4}$	89.26
Average	$(9.1 \pm 4.8) \cdot 10^{-4}$	88.9±1.3

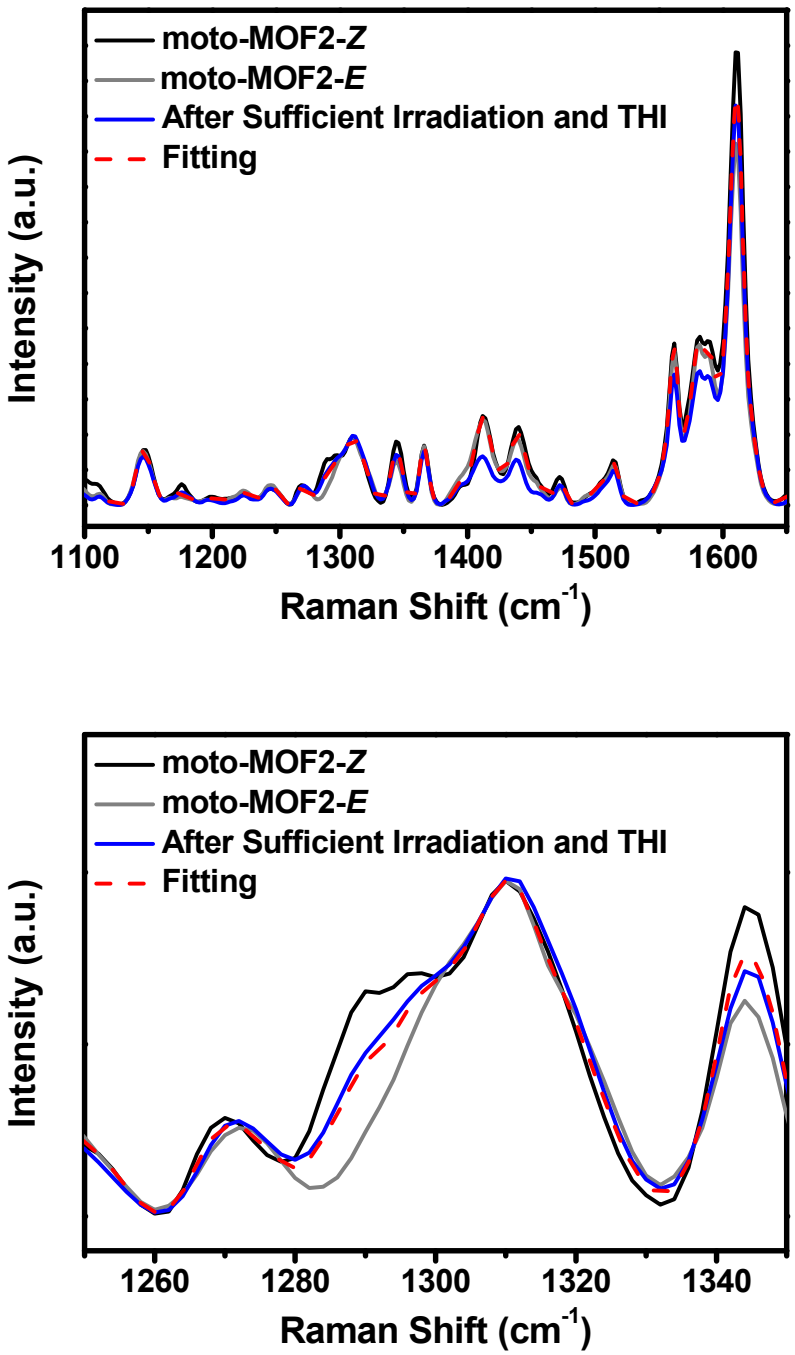

Supplementary Figure 49. Comparison of the Raman spectra of moto-MOF**2**-***Z*** (black line) and moto-MOF**2**-***E*** (grey line) after long irradiation at 395 nm (1 h, 4x$t_{1/2}$, blue line) to equalize 1:1 ratio of **2**-***Z*** and **2**-***E*** pillars. The major changes indicative for *E*/*Z* isomers are observed around 1290 cm^{-1}. Starting from each isomer moto-MOF**2**-***Z*** or moto-MOF**2**-***E*** same spectrum is obtained (blue line) indicating unidirectional rotation of molecular motor. The green, dashed line is a model spectrum consisting of 50% contribution of moto-MOF**2**-***Z*** and moto-MOF**2**-***E*** spectra. Bands between 1400-1450 cm^{-1} are characteristic of DMF and are not reproducible in the confocal volume of Raman microscope. These spectra were measured for sample kept between two 100 μm thick sapphire slides at x 100 magnification to minimize the contribution of background.

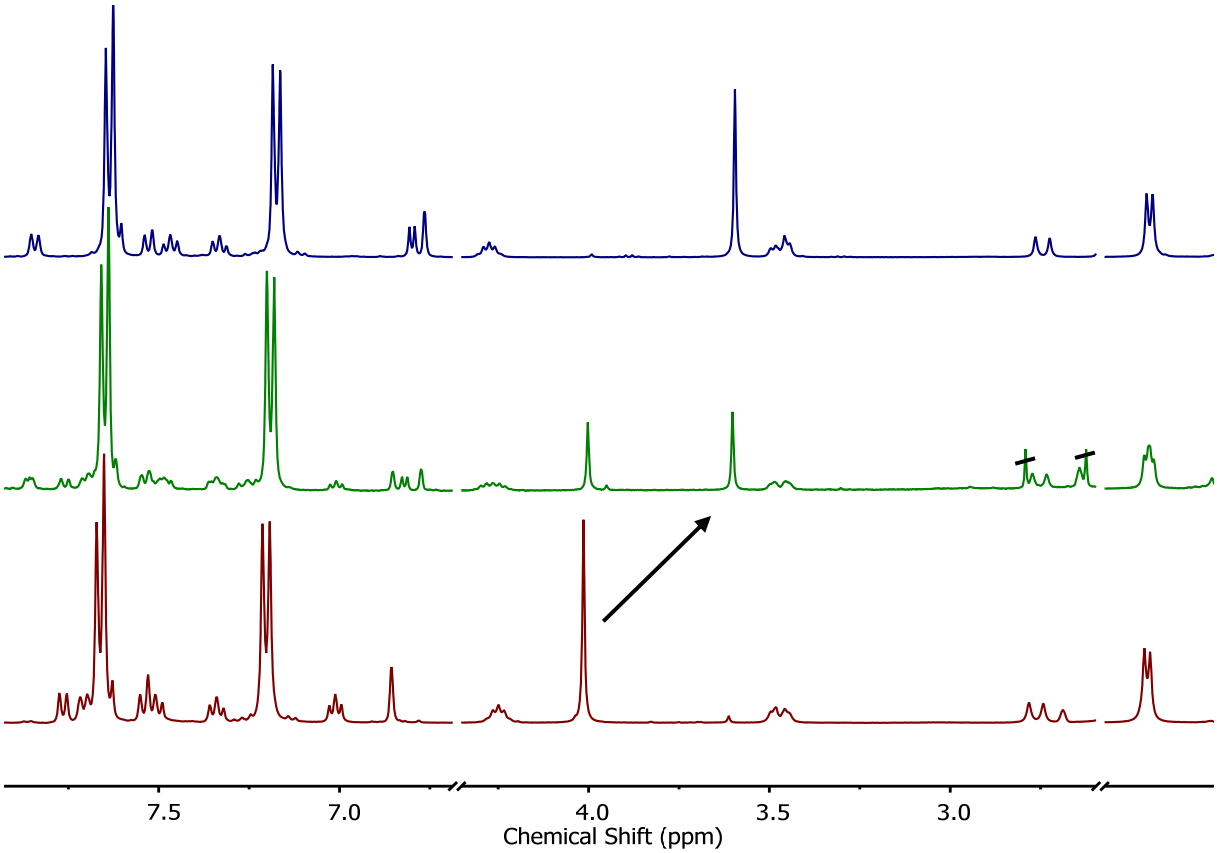

Supplementary Figure 50. Comparison of ^{1}H NMR (DMSO-d_6, digested using D_2SO_4) spectra of moto-MOF**2**-***Z*** (black spectrum), and moto-MOF**2**-***Z*** after irradiation at 395 nm and THI (red spectrum). Crystals of moto-MOF**2**-***Z*** were ground in a mortar and irradiated for 4 h at -20 °C with stirring. The crystals were recovered by centrifugation, washed with DCM to remove DMF and dried in vacuo. Upon irradiation, a metastable **2**-***E*** pillar is formed which is subsequently converted to stable **2**-***Z*** thereby showing unidirectional rotation of the motor. The ^{1}H NMR spectrum of digested moto-MOF**2**-***E*** is shown for comparison. Crossed resonances belong to residual DMF.

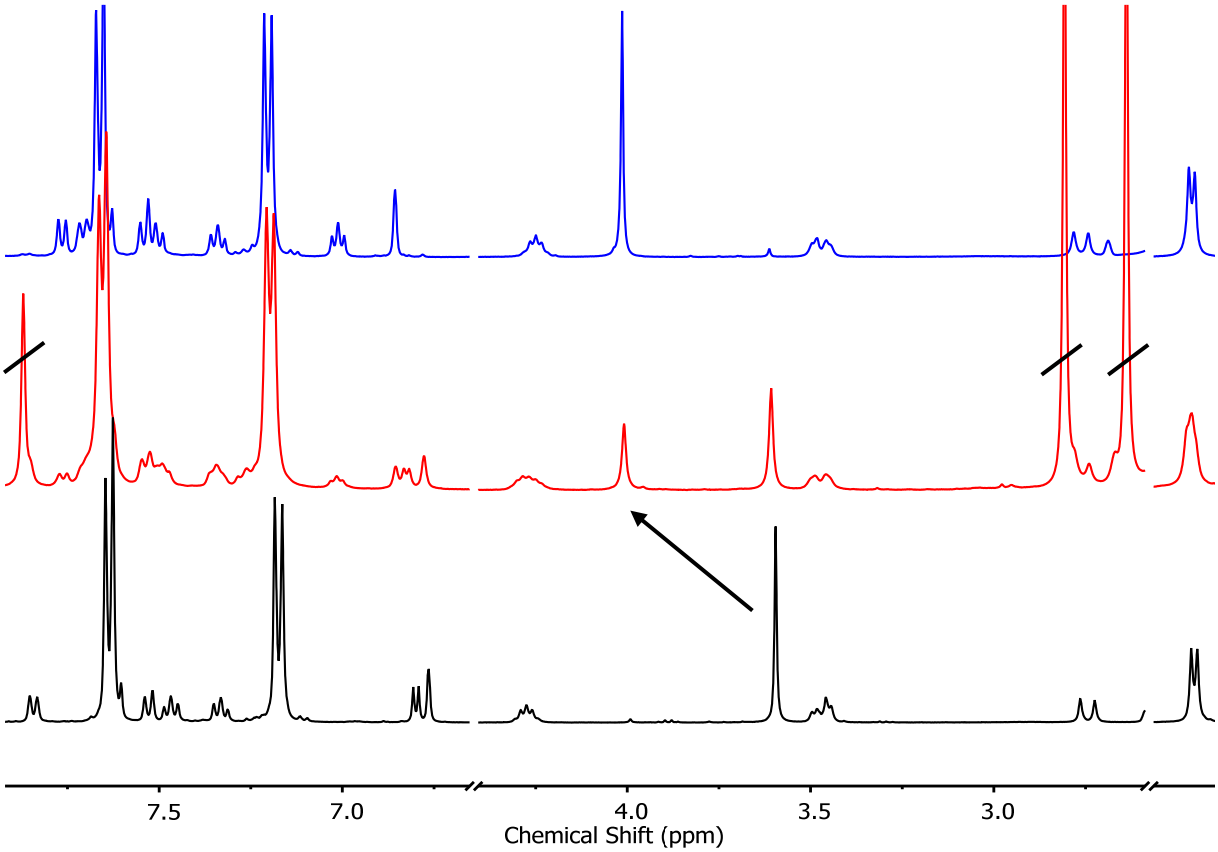

Supplementary Figure 51. Comparison of ^{1}H NMR (DMSO-d_6, digested using D_2SO_4) spectra of moto-MOF**2**-***E*** (black spectrum), and moto-MOF**2**-***E*** after irradiation at 395 nm and THI (red spectrum). Crystals of moto-MOF**2**-***E*** were ground in a mortar and irradiated for 4 h at -20 °C with stirring. The crystals were recovered by centrifugation, washed with DCM to remove DMF and dried in vacuo. Upon irradiation, a metastable **2**-***Z*** pillar is formed which is subsequently converted to stable **2**-***E*** thereby showing unidirectional rotation of the motor. The final ratio of **2**-***E***/**2**-***Z*** 60/40 was determined by integration of the methoxy resonances of the respective isomers. The ^{1}H NMR spectrum of digested moto-MOF**2**-***Z*** is shown for comparison. Crossed resonances belong to residual DMF.

13. Computational details

Supplementary Table 5. Cartesian coordinates of stable-**1**.

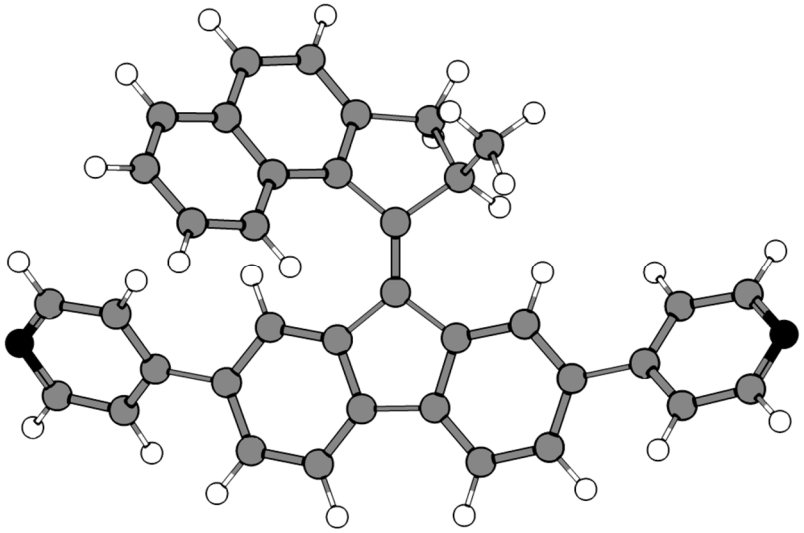

Number of imaginary frequencies: 0
SCF energy (B3LYP/6-31G(d,p)) -1535.17285555

C	-0.232374000	0.433095000	-1.187440000
C	-0.545392000	0.086692000	0.100297000
C	0.356932000	0.007306000	1.280293000
C	-0.409969000	-0.329467000	2.424499000
C	-1.801767000	-0.484431000	2.021319000
C	-1.904721000	-0.197073000	0.635174000
C	-1.227070000	1.029214000	-2.188867000
C	-0.367822000	2.150300000	-2.846264000
C	1.026330000	1.578587000	-2.780685000
C	1.084969000	0.547557000	-1.842871000
C	2.149503000	1.948050000	-3.543892000
C	3.320617000	1.235712000	-3.403284000
C	3.394122000	0.100699000	-2.549519000
C	2.252305000	-0.280497000	-1.764556000
C	4.569276000	-0.696251000	-2.493490000
C	4.611035000	-1.845449000	-1.737272000
C	3.467273000	-2.251984000	-1.010266000
C	2.319599000	-1.488018000	-1.020497000
C	1.702144000	0.343904000	1.443108000
C	2.302859000	0.286872000	2.713331000
C	1.530602000	-0.104240000	3.823744000
C	0.177719000	-0.400207000	3.686735000
C	-2.923714000	-0.842027000	2.766630000
C	-4.162851000	-0.922751000	2.137577000
C	-4.293263000	-0.657820000	0.761937000
C	-3.153146000	-0.303467000	0.017652000
C	-1.704179000	0.019327000	-3.251013000
C	3.732791000	0.643689000	2.881224000
C	-5.616190000	-0.758142000	0.099344000

C	4.199578000	1.298341000	4.032257000
C	5.552255000	1.612022000	4.142616000
N	6.466993000	1.330833000	3.205290000
C	6.019287000	0.707736000	2.107171000
C	4.689916000	0.346760000	1.898087000
C	-5.997497000	0.116371000	-0.930363000
C	-7.251243000	-0.023733000	-1.521481000
N	-8.147385000	-0.954678000	-1.169191000
C	-7.783861000	-1.787392000	-0.184954000
C	-6.554749000	-1.734728000	0.468608000
H	-2.088686000	1.457951000	-1.672404000
H	-0.681913000	2.380595000	-3.870148000
H	-0.444986000	3.078219000	-2.264006000
H	2.088375000	2.778936000	-4.241040000
H	4.199948000	1.506811000	-3.981453000
H	5.432400000	-0.390553000	-3.078888000
H	5.511757000	-2.451225000	-1.710931000
H	3.492563000	-3.177212000	-0.442308000
H	1.447832000	-1.813654000	-0.466233000
H	2.290774000	0.688792000	0.604414000
H	2.000146000	-0.181353000	4.799258000
H	-0.411470000	-0.671504000	4.558058000
H	-2.838484000	-1.052545000	3.828836000
H	-5.044467000	-1.173410000	2.718890000
H	-3.267530000	-0.152977000	-1.046834000
H	-0.855899000	-0.359404000	-3.829556000
H	-2.206802000	-0.841544000	-2.801511000
H	-2.403019000	0.496999000	-3.945981000
H	3.513380000	1.584594000	4.822835000
H	5.919072000	2.124239000	5.030665000
H	6.767155000	0.476173000	1.350494000
H	4.410407000	-0.182633000	0.993299000
H	-5.336350000	0.915543000	-1.249854000
H	-7.554354000	0.655054000	-2.316990000
H	-8.513599000	-2.545829000	0.093568000
H	-6.320770000	-2.462731000	1.238617000

Supplementary Table 6. Cartesian coordinates of metastable-**1**.

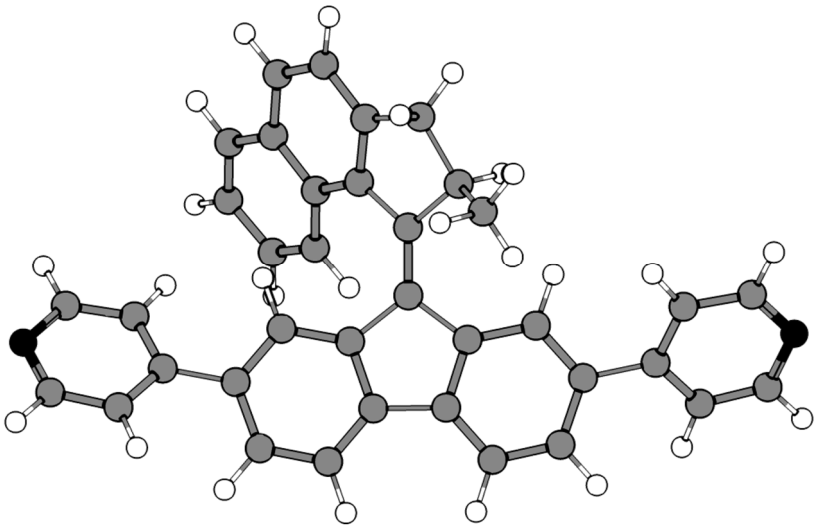

Number of imaginary frequencies: 0
SCF energy (B3LYP/6-31G(d,p)) -1535.16717322

C	-0.813633000	1.910392000	-0.721244000
C	-0.953486000	1.070115000	0.362111000
C	0.036524000	0.783491000	1.427744000
C	-0.488198000	-0.215758000	2.288973000
C	-1.837187000	-0.543316000	1.845200000
C	-2.110533000	0.197671000	0.665565000
C	-1.420079000	1.641907000	-2.113467000
C	-0.503039000	2.461186000	-3.069611000
C	0.188871000	3.447977000	-2.177247000
C	-0.011076000	3.135554000	-0.831021000
C	0.937781000	4.567323000	-2.583794000
C	1.459308000	5.409292000	-1.628236000
C	1.185964000	5.209223000	-0.247023000
C	0.405895000	4.078414000	0.177169000
C	1.633779000	6.150306000	0.717967000
C	1.288334000	6.025776000	2.044420000
C	0.458431000	4.957379000	2.451488000
C	0.031842000	4.009370000	1.544051000
C	1.361178000	1.195236000	1.589019000
C	2.146206000	0.671024000	2.629485000
C	1.589973000	-0.291547000	3.495354000
C	0.284658000	-0.743005000	3.323262000
C	-2.807273000	-1.373509000	2.405740000
C	-4.063310000	-1.452630000	1.810856000
C	-4.375890000	-0.690930000	0.667273000
C	-3.390735000	0.141165000	0.108782000
C	-1.471224000	0.173864000	-2.559887000
C	3.545968000	1.126354000	2.811190000
C	-5.730098000	-0.756921000	0.066728000
C	4.559282000	0.251158000	3.233062000

C	5.858270000	0.729671000	3.388581000
N	6.224024000	1.997436000	3.157405000
C	5.255738000	2.830943000	2.754601000
C	3.926505000	2.456177000	2.570588000
C	-5.929956000	-0.676689000	-1.320510000
C	-7.223809000	-0.739079000	-1.833184000
N	-8.323480000	-0.876899000	-1.081215000
C	-8.132120000	-0.955507000	0.242234000
C	-6.882554000	-0.900456000	0.855596000
H	-2.429713000	2.076619000	-2.162456000
H	0.222700000	1.789927000	-3.548938000
H	-1.058625000	2.948925000	-3.878160000
H	1.100318000	4.759939000	-3.640457000
H	2.054006000	6.270922000	-1.919628000
H	2.239077000	6.988143000	0.382171000
H	1.629180000	6.756315000	2.771727000
H	0.146310000	4.883717000	3.488979000
H	-0.614391000	3.208309000	1.875327000
H	1.806335000	1.902226000	0.900410000
H	2.186658000	-0.677386000	4.315837000
H	-0.120120000	-1.502957000	3.985638000
H	-2.593531000	-1.948729000	3.302069000
H	-4.812670000	-2.117673000	2.228107000
H	-3.653609000	0.766033000	-0.737124000
H	-0.473786000	-0.273747000	-2.500886000
H	-2.143856000	-0.439936000	-1.962283000
H	-1.801608000	0.119161000	-3.603063000
H	4.345170000	-0.797387000	3.413597000
H	6.649706000	0.054581000	3.710173000
H	5.556929000	3.861674000	2.574526000
H	3.192475000	3.197248000	2.271343000
H	-5.085656000	-0.593008000	-1.997346000
H	-7.383886000	-0.682546000	-2.908664000
H	-9.029451000	-1.061450000	0.849612000
H	-6.810539000	-0.942225000	1.937586000

Supplementary Table 7. Cartesian coordinates of TS-THI-**1**.

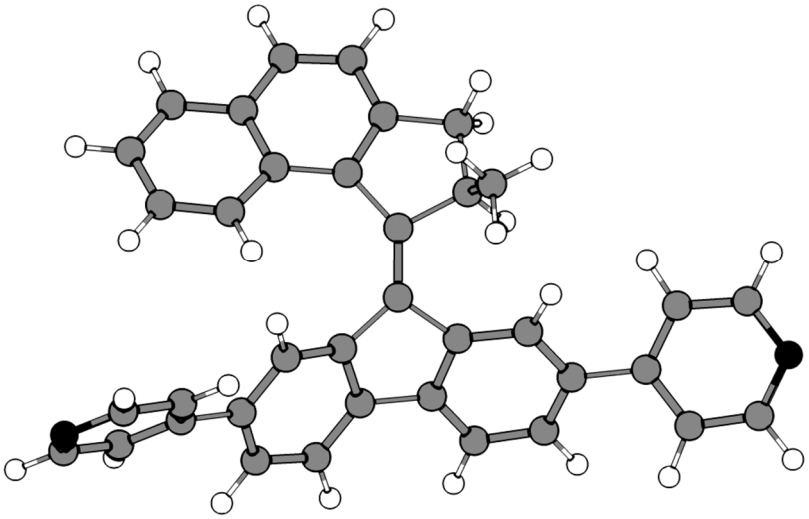

Number of imaginary frequencies: 1
SCF energy (B3LYP/6-31G(d,p)) -1535.13323010

C	0.368805000	1.432211000	0.450115000
C	0.381984000	0.070981000	0.191703000
C	-0.679098000	-0.888741000	-0.243859000
C	-0.122389000	-1.791605000	-1.187370000
C	1.327051000	-1.639725000	-1.149735000
C	1.652366000	-0.664671000	-0.164927000
C	1.676905000	2.079217000	0.935025000
C	1.635440000	3.542580000	0.479615000
C	0.217435000	3.741929000	0.054293000
C	-0.561635000	2.580811000	0.153186000
C	-0.263319000	4.965773000	-0.452569000
C	-1.565132000	5.065679000	-0.864311000
C	-2.448879000	3.967906000	-0.697903000
C	-1.975078000	2.724049000	-0.143042000
C	-3.820000000	4.117900000	-1.033844000
C	-4.732915000	3.118448000	-0.788628000
C	-4.295464000	1.933947000	-0.163774000
C	-2.962759000	1.758481000	0.145293000
C	-1.936682000	-1.192730000	0.270142000
C	-2.735065000	-2.198230000	-0.308175000
C	-2.222756000	-2.942662000	-1.384408000
C	-0.901174000	-2.775037000	-1.793075000
C	2.313847000	-2.389571000	-1.783375000
C	3.643797000	-2.237138000	-1.398531000
C	3.987440000	-1.366229000	-0.352736000
C	2.982751000	-0.586256000	0.257089000
C	1.816396000	1.939782000	2.462504000
C	-4.087802000	-2.481236000	0.229103000
C	5.388069000	-1.279358000	0.126502000
C	-5.156078000	-2.826719000	-0.613856000
C	-6.409481000	-3.084569000	-0.063001000

N	-6.681143000	-3.023594000	1.247155000
C	-5.661441000	-2.693650000	2.050677000
C	-4.371164000	-2.418549000	1.602957000
C	5.946513000	-0.071236000	0.573085000
C	7.267001000	-0.046921000	1.016726000
N	8.068534000	-1.119311000	1.046770000
C	7.536342000	-2.271399000	0.617946000
C	6.227986000	-2.404020000	0.158663000
H	2.527170000	1.596539000	0.459353000
H	1.916367000	4.240187000	1.278675000
H	2.326310000	3.729230000	-0.352848000
H	0.414814000	5.810961000	-0.531351000
H	-1.949196000	5.989512000	-1.288224000
H	-4.138903000	5.059867000	-1.472265000
H	-5.779703000	3.250484000	-1.044665000
H	-5.008427000	1.154294000	0.087543000
H	-2.662482000	0.866994000	0.654728000
H	-2.302196000	-0.696405000	1.158426000
H	-2.828031000	-3.725424000	-1.830280000
H	-0.470343000	-3.447632000	-2.528996000
H	2.050054000	-3.104515000	-2.557420000
H	4.419178000	-2.807253000	-1.900086000
H	3.264007000	0.000562000	1.120720000
H	0.995090000	2.454067000	2.973381000
H	1.795280000	0.891044000	2.773298000
H	2.757597000	2.383673000	2.805753000
H	-5.019450000	-2.869650000	-1.689611000
H	-7.242627000	-3.348022000	-0.712497000
H	-5.885226000	-2.653000000	3.115372000
H	-3.591041000	-2.186750000	2.321160000
H	5.368835000	0.847205000	0.551343000
H	7.706320000	0.888276000	1.360028000
H	8.190119000	-3.141346000	0.650188000
H	5.858654000	-3.378211000	-0.144645000

Supplementary Table 8. Cartesian coordinates of **DPNI**.

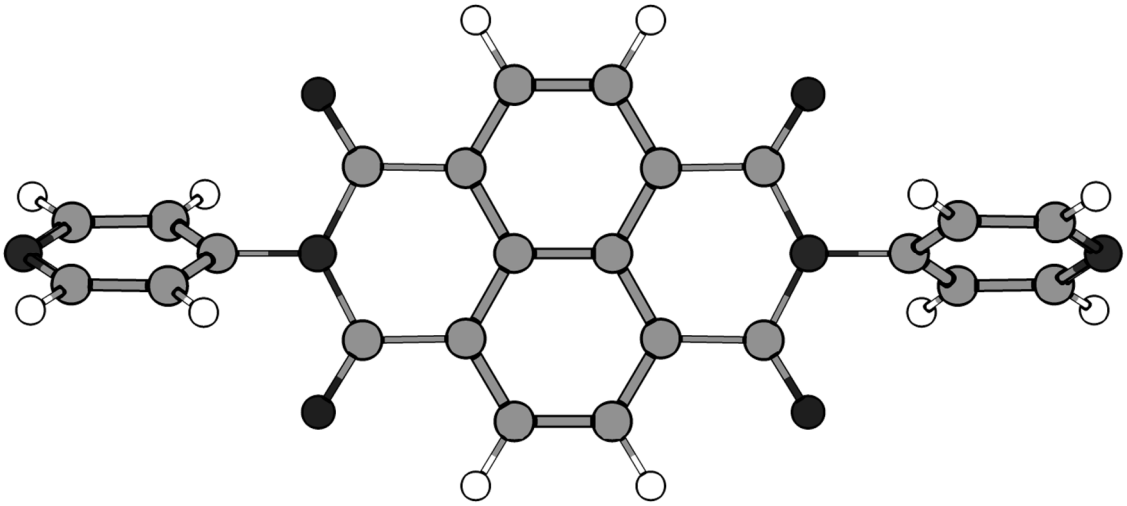

Number of imaginary frequencies: 0
SCF energy (B3LYP/6-31G(d,p)) -1441.77349800

C	-7.085091000	0.455401000	-1.046772000
C	-5.691621000	0.474821000	-1.102572000
C	-4.987039000	-0.000003000	-0.000028000
C	-5.691807000	-0.474816000	1.102401000
C	-7.085267000	-0.455374000	1.046373000
N	-7.783810000	0.000018000	-0.000257000
N	-3.541686000	-0.000007000	0.000092000
C	-2.892443000	1.257010000	-0.004607000
C	-1.405623000	1.233368000	-0.001590000
C	-0.710856000	-0.000002000	0.000137000
C	-1.405619000	-1.233375000	0.001851000
C	-2.892438000	-1.257022000	0.004904000
C	-0.703588000	2.428336000	-0.001102000
C	0.703580000	2.428339000	0.001282000
C	1.405619000	1.233373000	0.001825000
C	0.710856000	0.000000000	0.000125000
C	1.405623000	-1.233370000	-0.001606000
C	0.703588000	-2.428339000	-0.001105000
C	-0.703580000	-2.428341000	0.001294000
C	2.892438000	1.257020000	0.004845000
N	3.541686000	0.000005000	0.000059000
C	2.892443000	-1.257012000	-0.004639000
C	4.987039000	0.000003000	-0.000037000
C	5.691788000	0.474835000	1.102396000
C	7.085249000	0.455397000	1.046390000
N	7.783810000	-0.000009000	-0.000222000
C	7.085108000	-0.455410000	-1.046741000
C	5.691639000	-0.474836000	-1.102563000
O	-3.530174000	2.294624000	-0.008970000
O	-3.530162000	-2.294642000	0.009001000
O	3.530163000	2.294639000	0.008987000

O	3.530174000	-2.294626000	-0.008979000
H	-7.665954000	0.824317000	-1.889427000
H	-5.174090000	0.856608000	-1.974884000
H	-5.174424000	-0.856610000	1.974797000
H	-7.666273000	-0.824282000	1.888933000
H	-1.261731000	3.357987000	-0.002274000
H	1.261719000	3.357992000	0.002424000
H	1.261731000	-3.357990000	-0.002282000
H	-1.261719000	-3.357994000	0.002447000
H	5.174390000	0.856640000	1.974778000
H	7.666241000	0.824319000	1.888953000
H	7.665986000	-0.824337000	-1.889382000
H	5.174123000	-0.856637000	-1.974877000

14. NMR and MS spectra

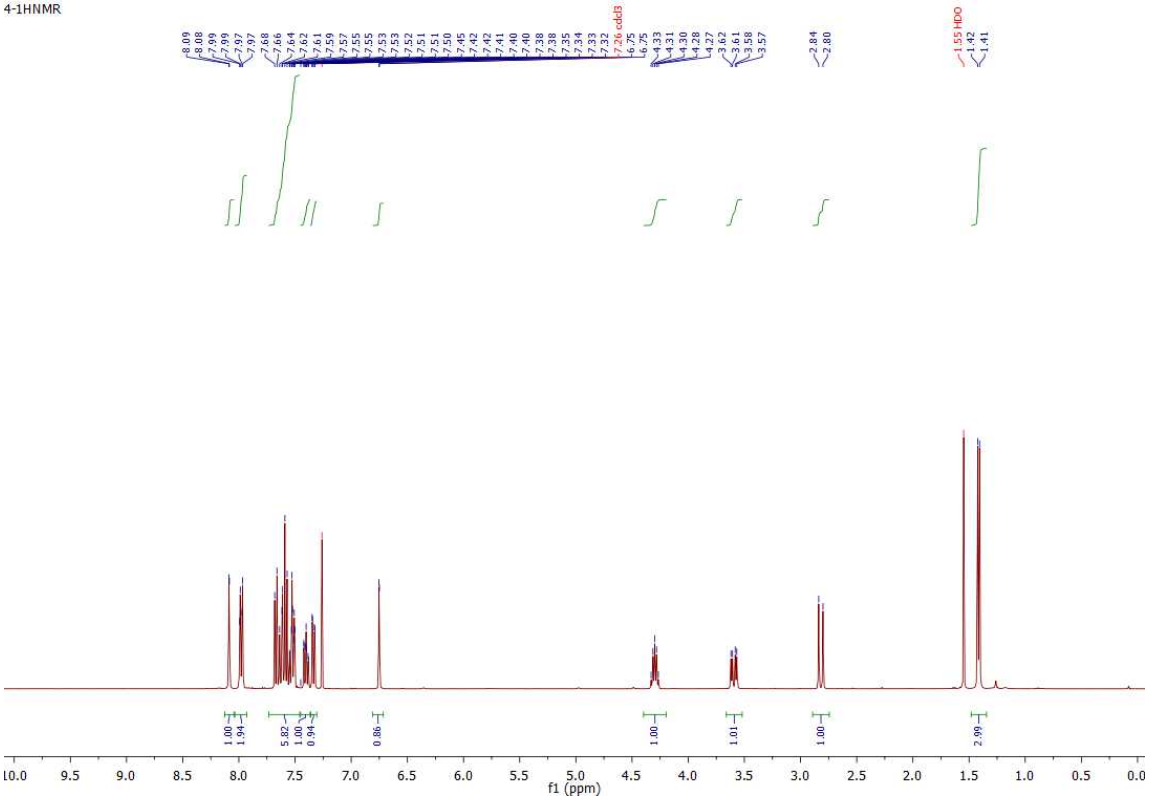

Supplementary Figure 52. ^{1}H NMR spectrum of **5**.

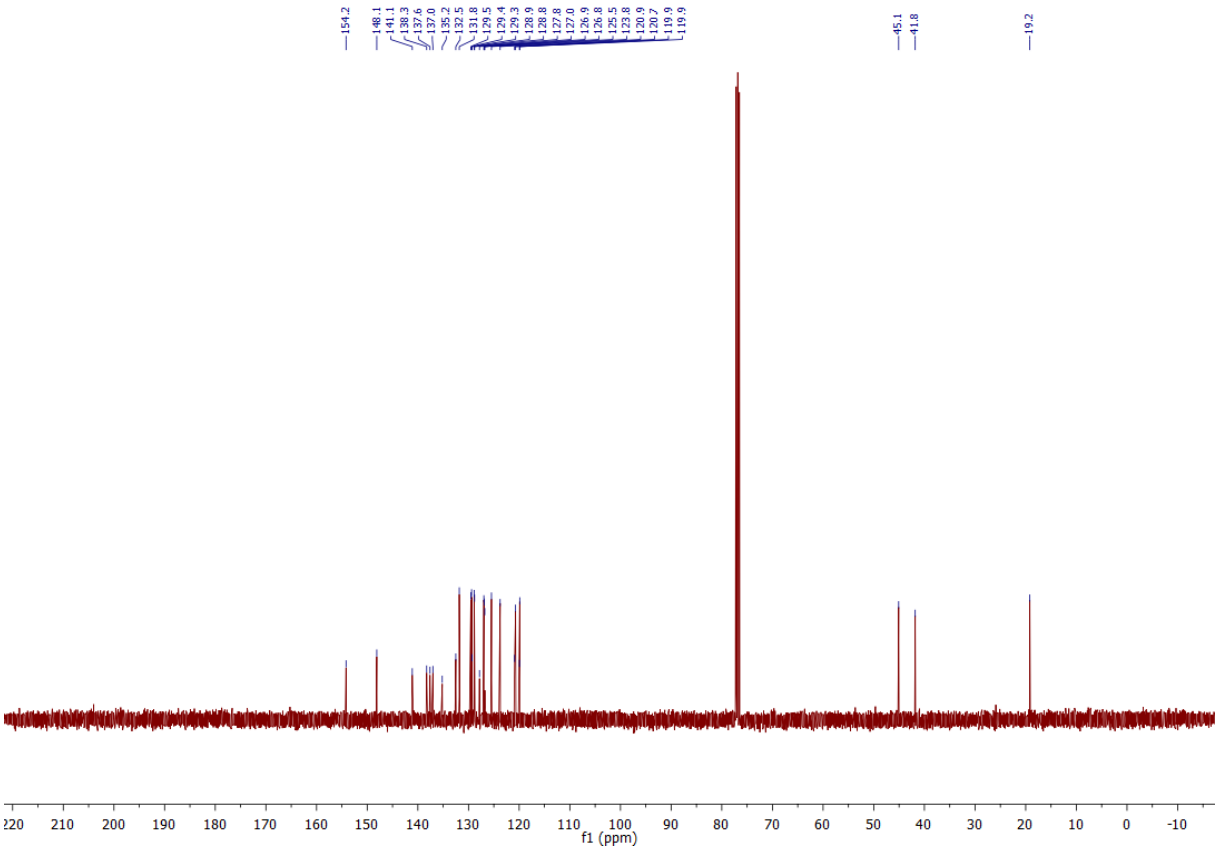

Supplementary Figure 53. ^{13}C NMR spectrum of **5**.

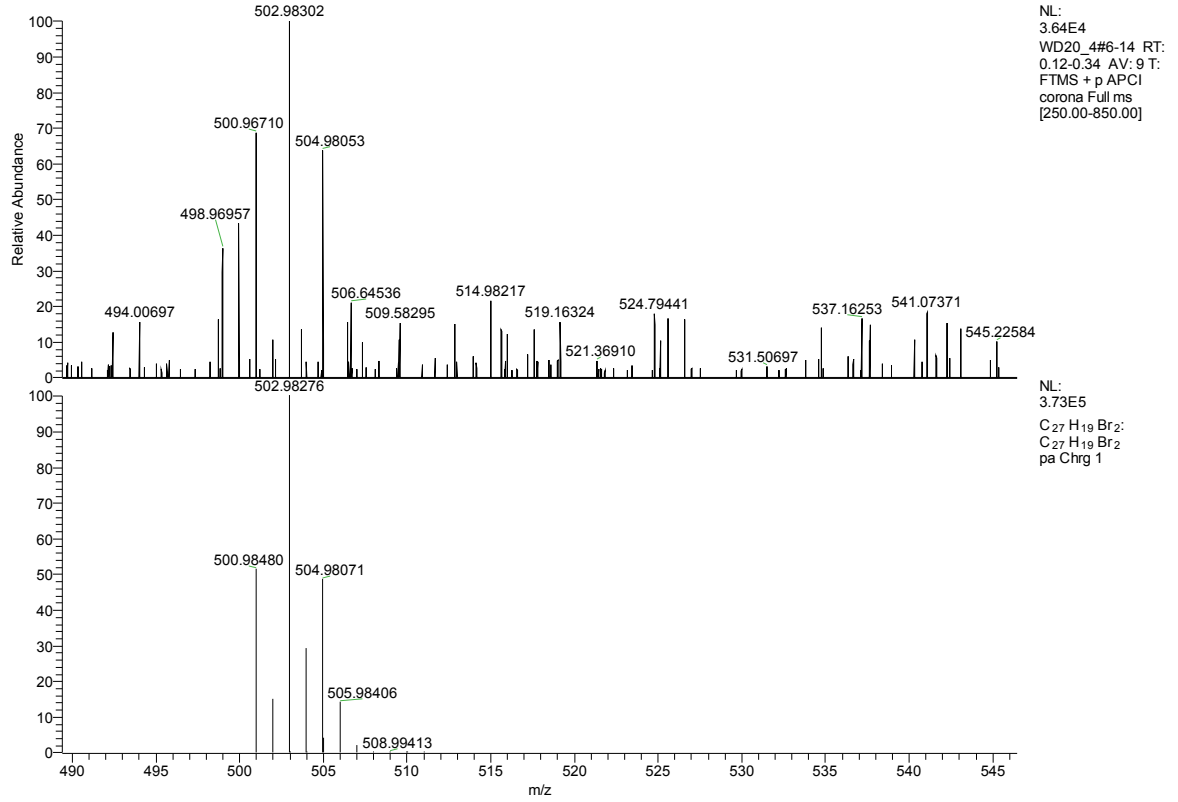

Supplementary Figure 54. HRMS (ESI) spectra of **5** (top:measured, bottom: calcd.).

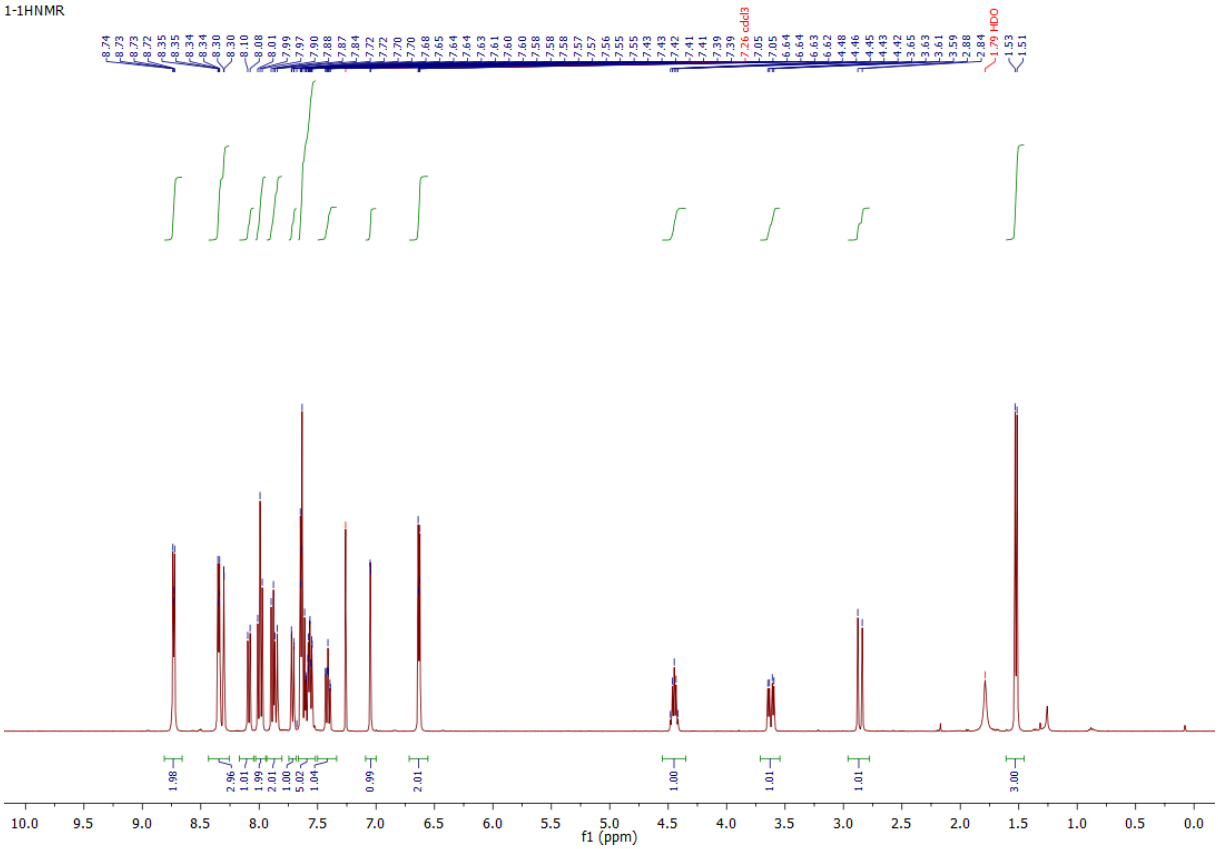

Supplementary Figure 55. ^{1}H NMR spectrum of **1**.

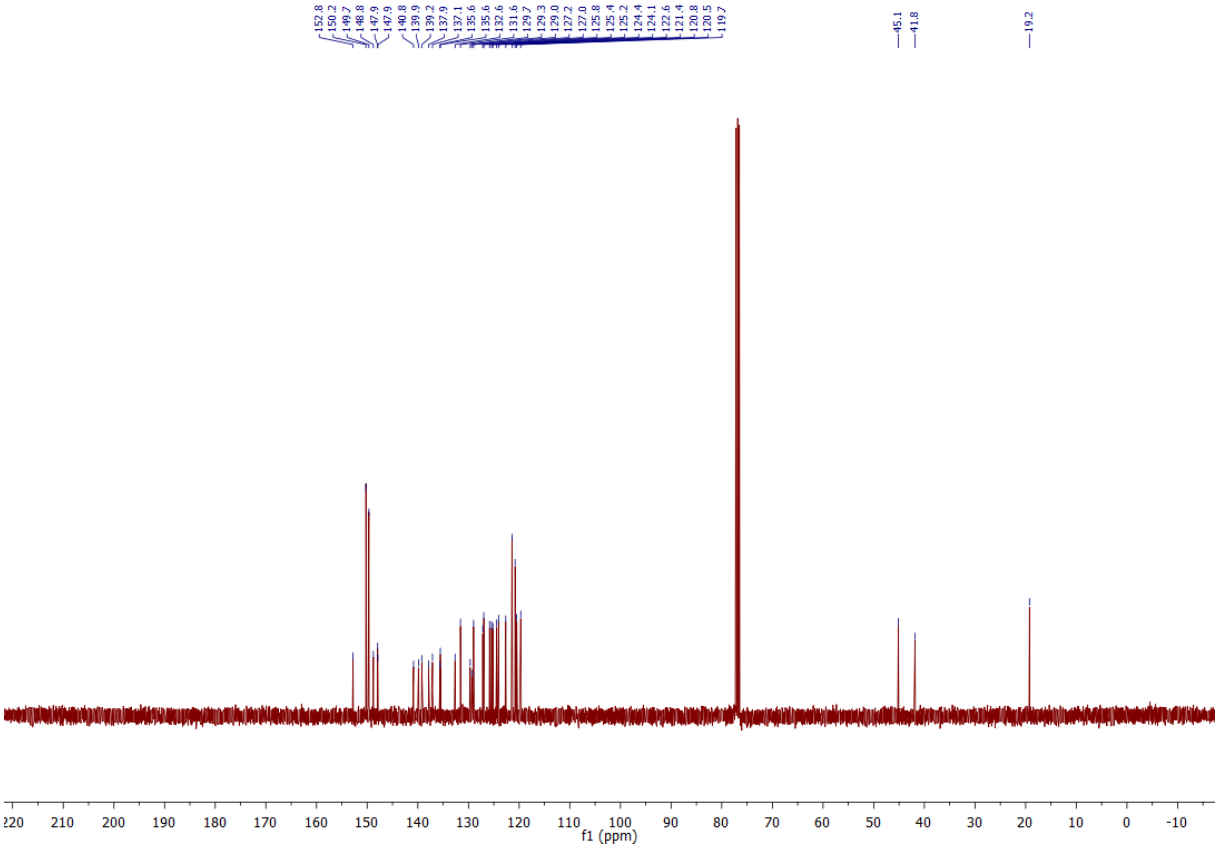

Supplementary Figure 56. ^{13}C NMR spectrum of **1**.

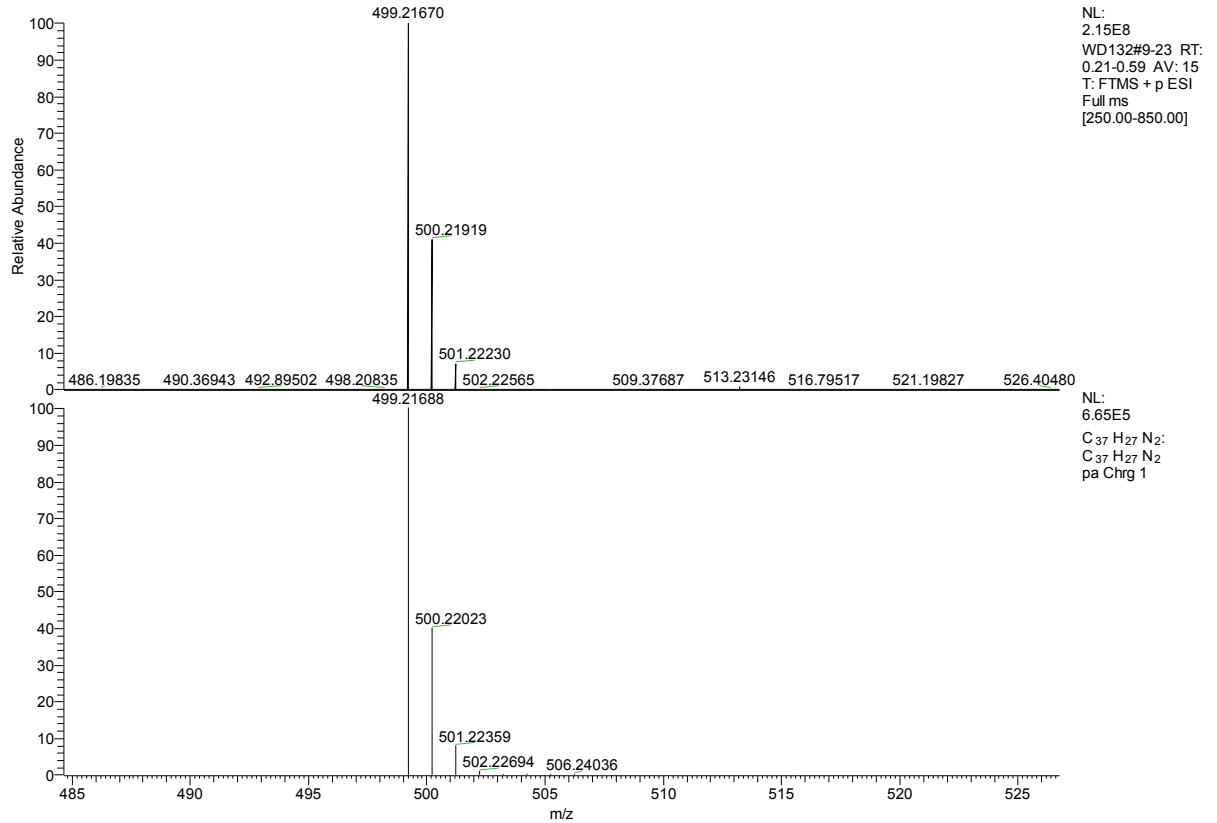

Supplementary Figure 57. HRMS (ESI) spectra of **1** (top:measured, bottom: calcd.).

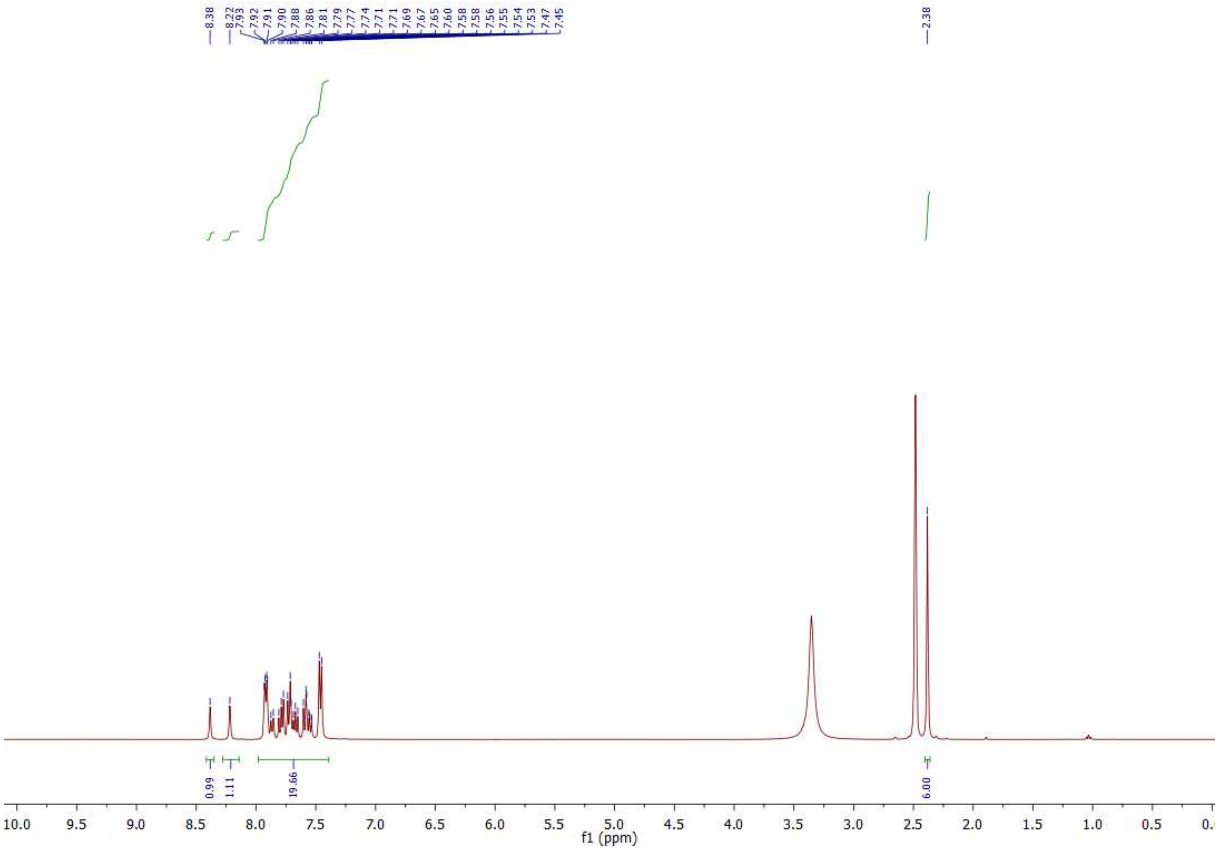

Supplementary Figure 58. ^{1}H NMR spectrum of **7**.

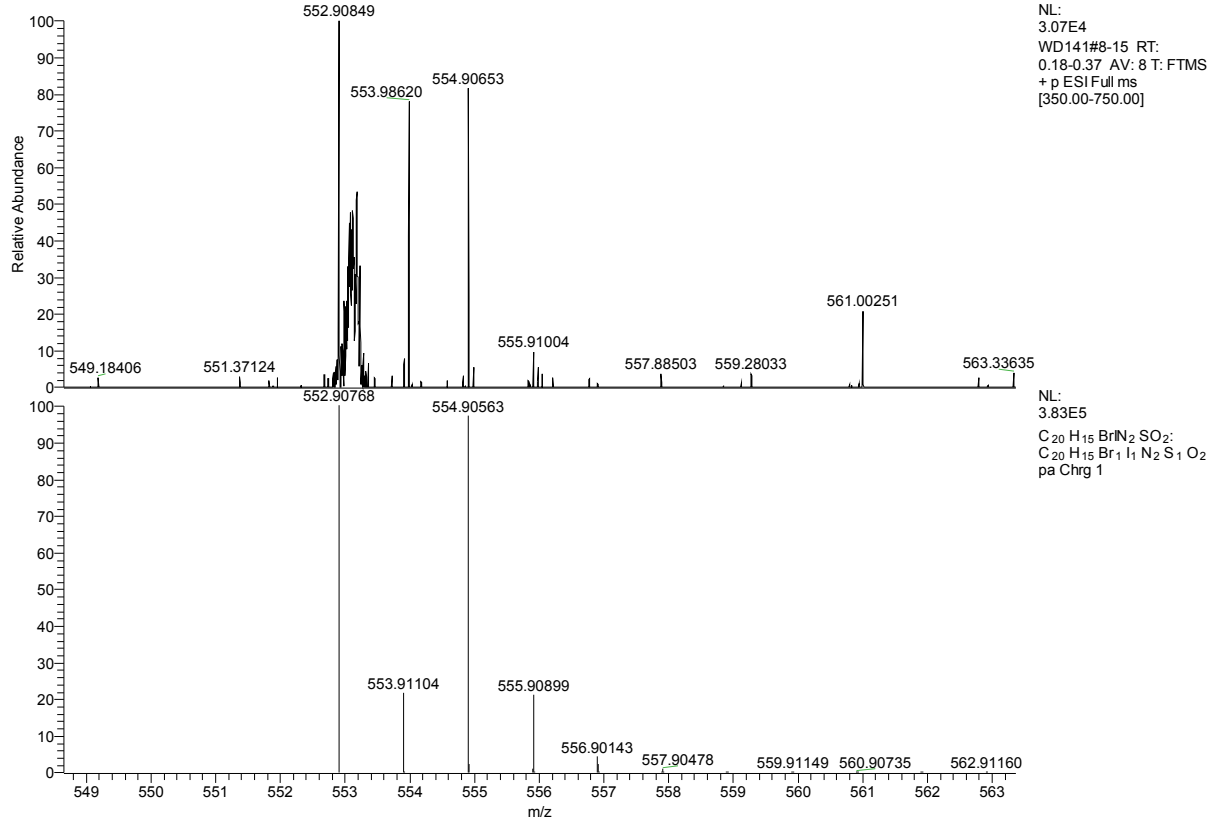

Supplementary Figure 59. HRMS (ESI) spectra of **7** (top:measured, bottom: calcd.).

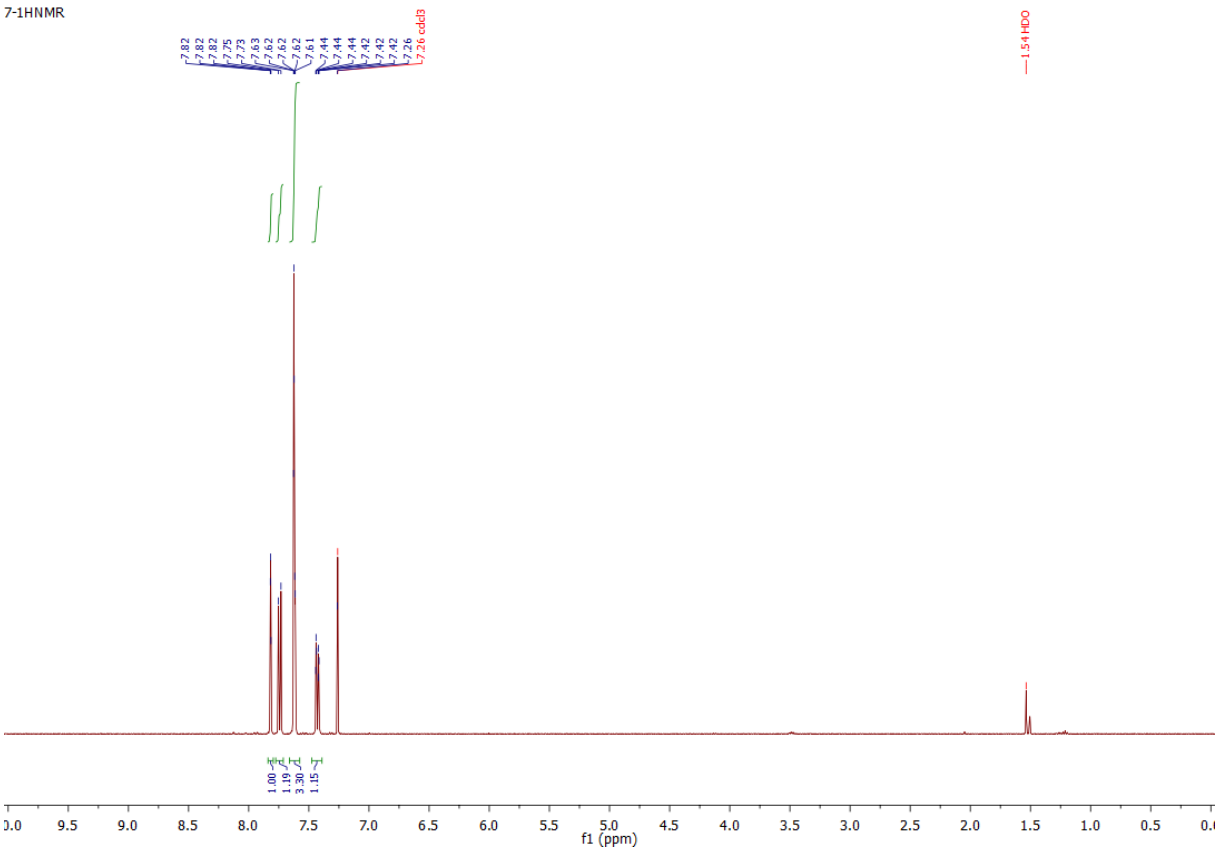

Supplementary Figure 60. ^{1}H NMR spectrum of **8**.

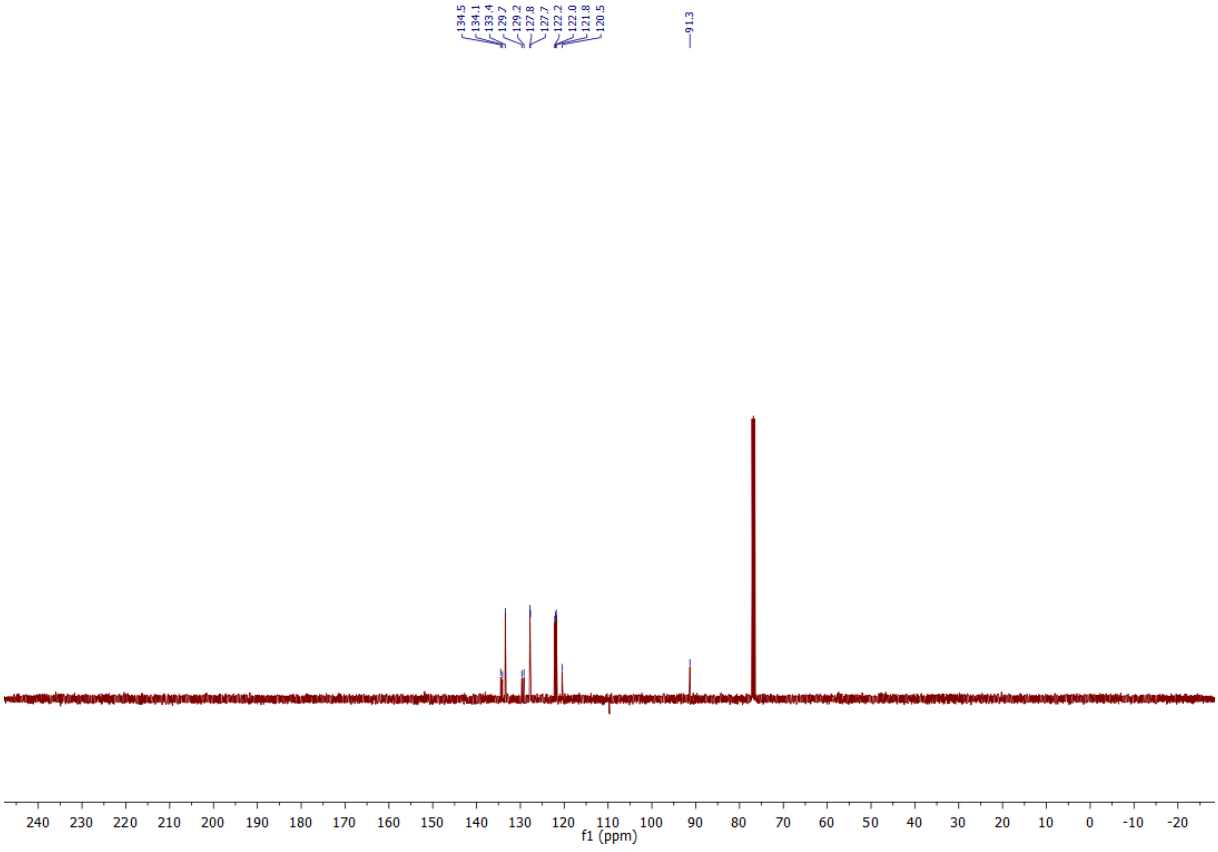

Supplementary Figure 61. ^{13}C NMR spectrum of **8**.

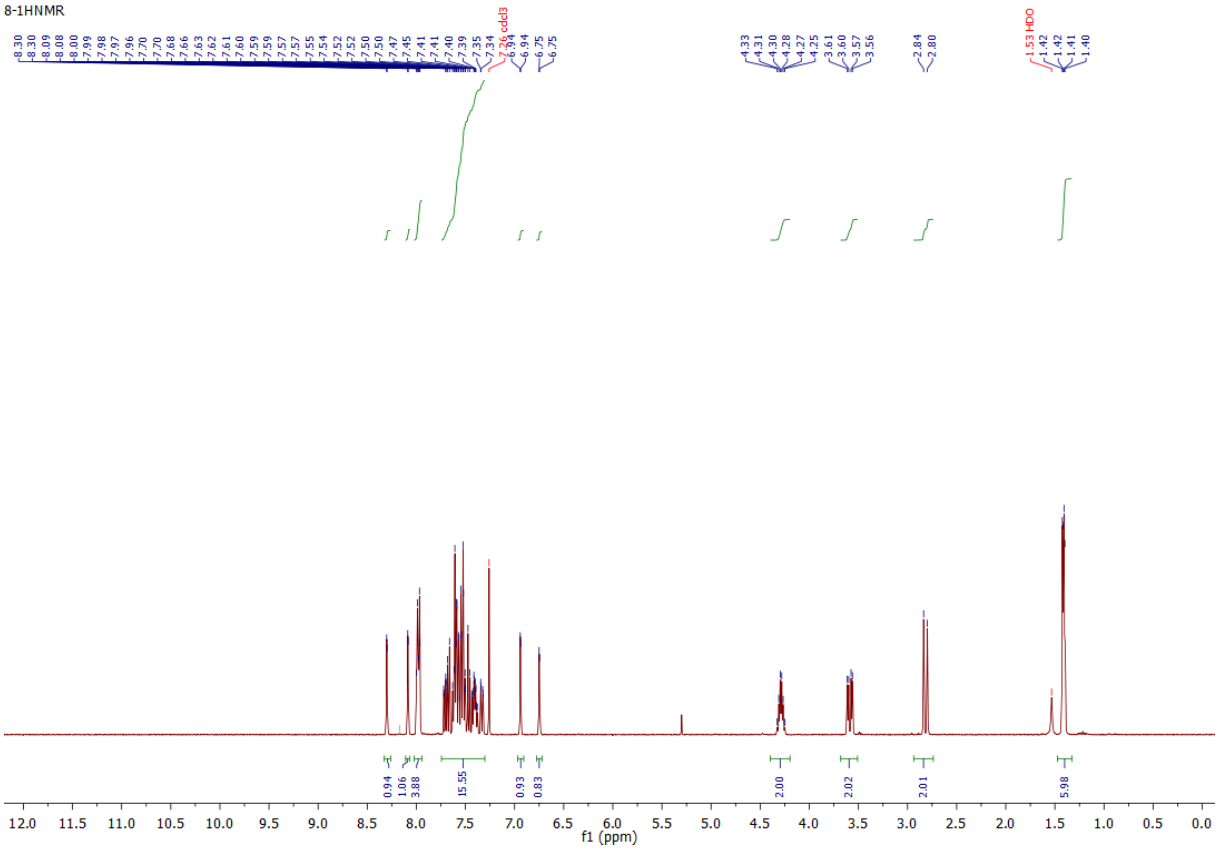

Supplementary Figure 62. ^{1}H NMR spectrum of **9**.

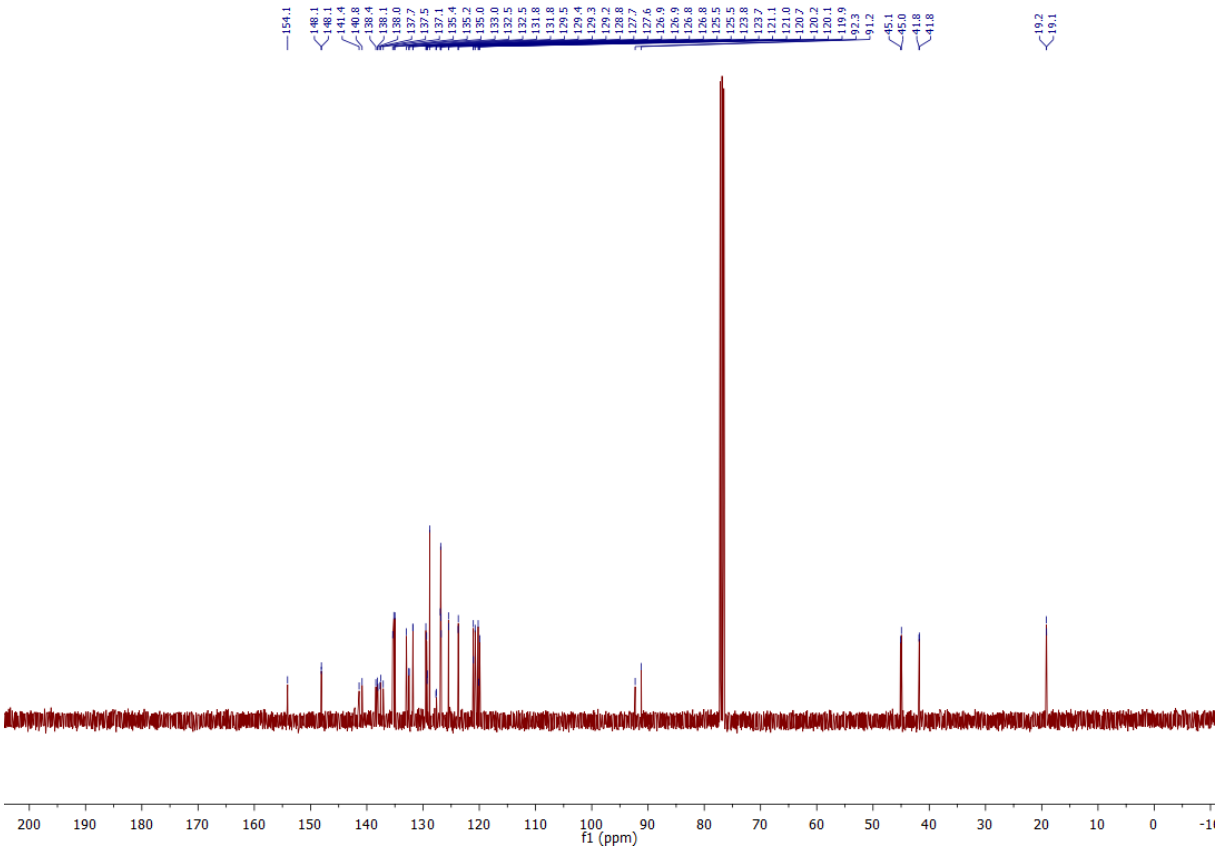

Supplementary Figure 63. ^{13}C NMR spectrum of **9**.

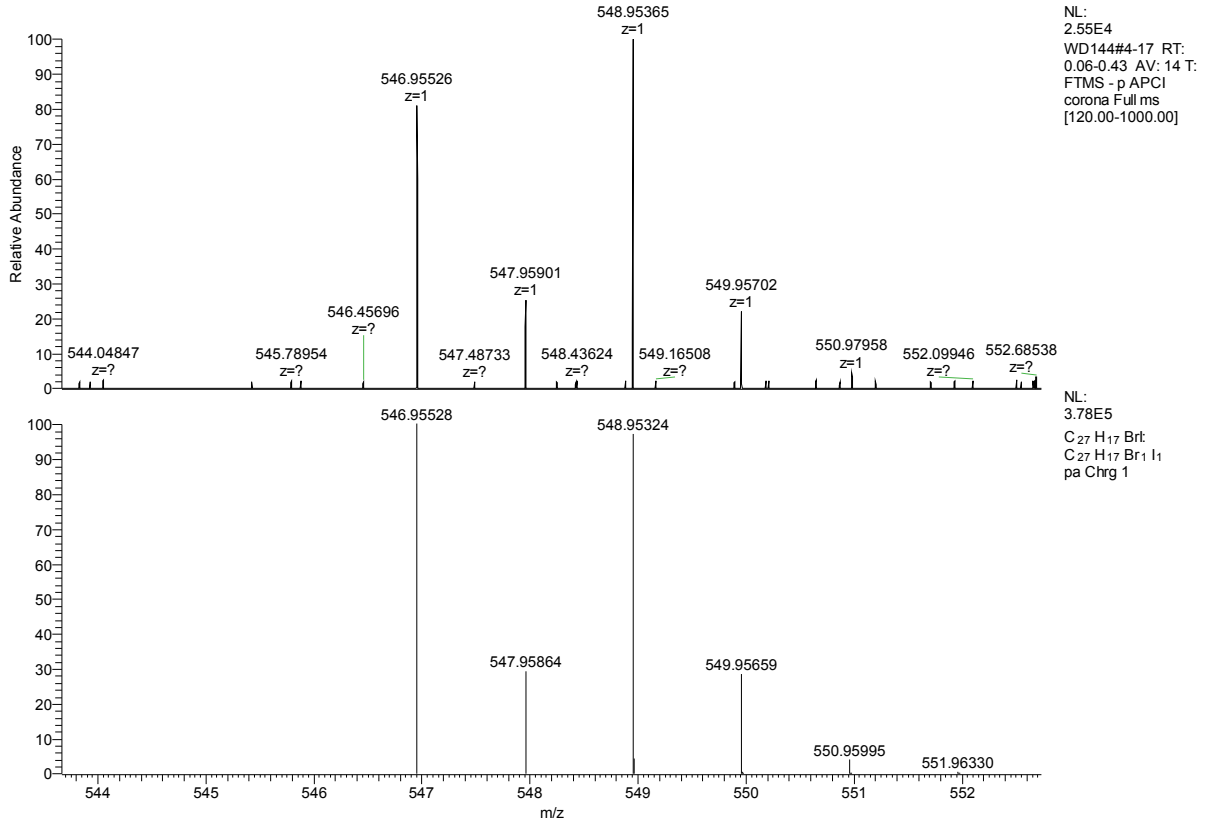

Supplementary Figure 64. HRMS (APCI) spectra of **9** (top:measured, bottom: calcd.).

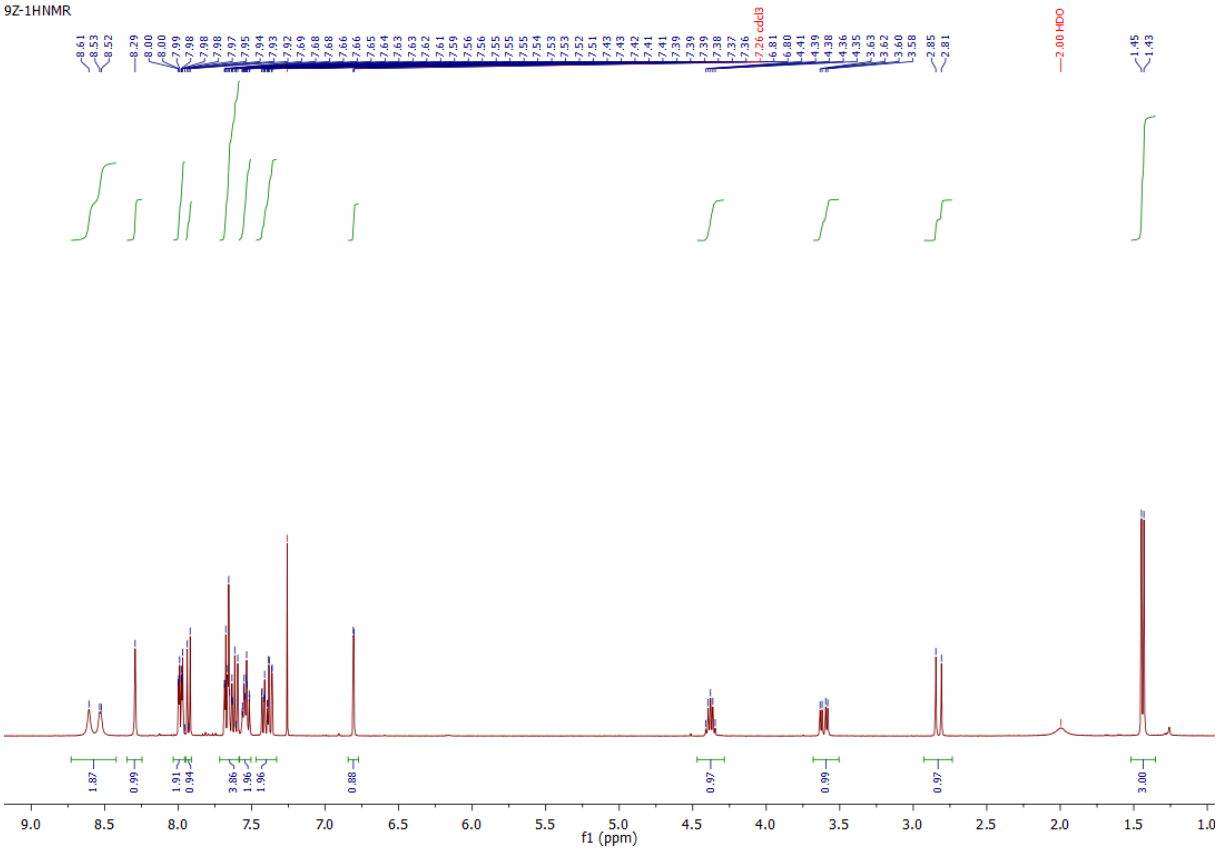

Supplementary Figure 65. ^{1}H NMR spectrum of **10-*Z***.

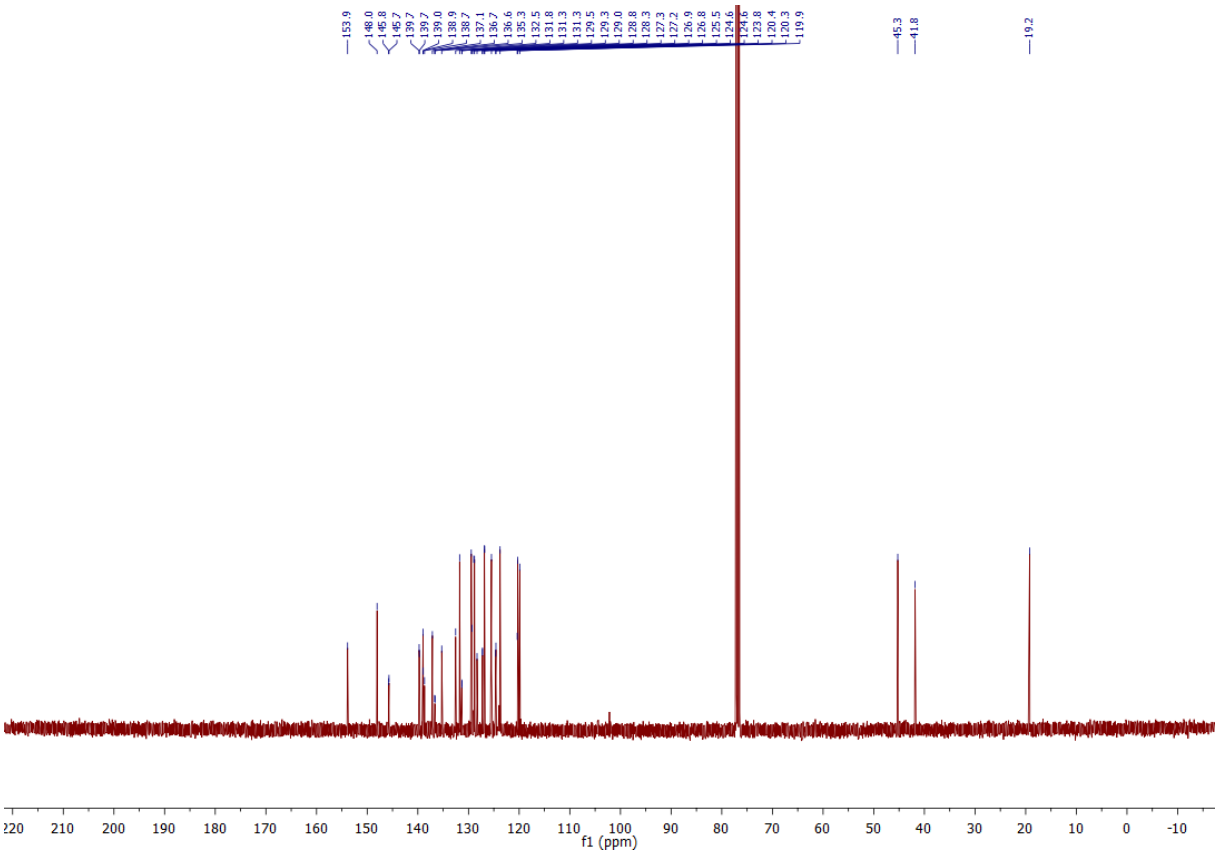

Supplementary Figure 66. ^{13}C NMR spectrum of **10-*Z***.

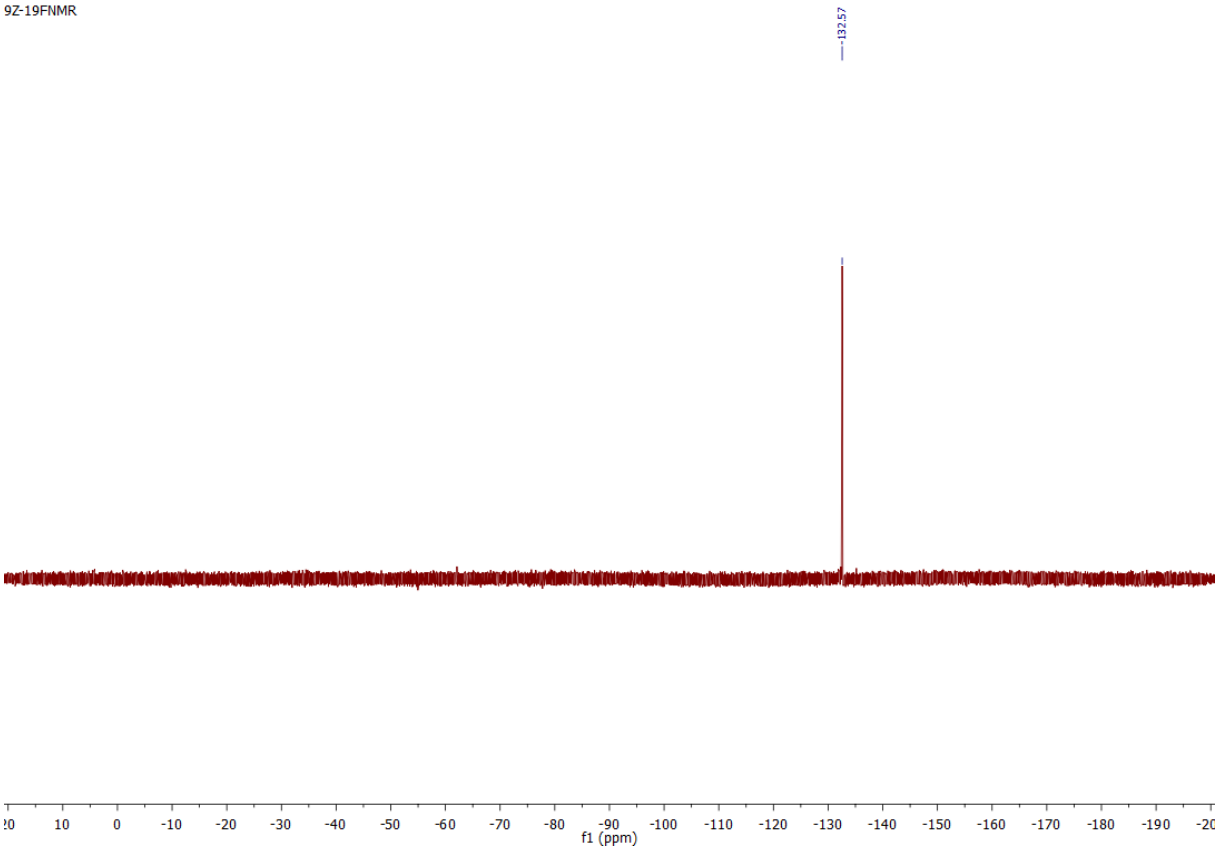

Supplementary Figure 67. ^{19}F NMR spectrum of **10-*Z***.

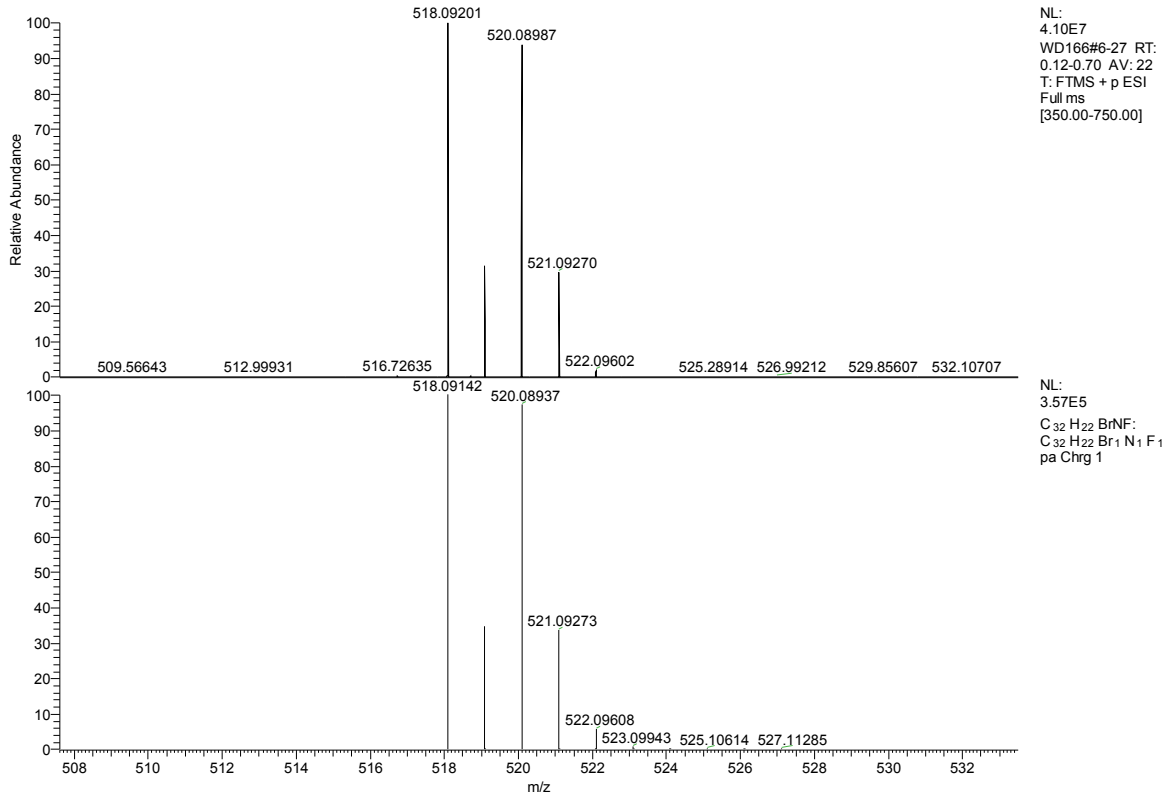

Supplementary Figure 68. HRMS (ESI) spectra of **10-*Z*** (top:measured, bottom: calcd.).

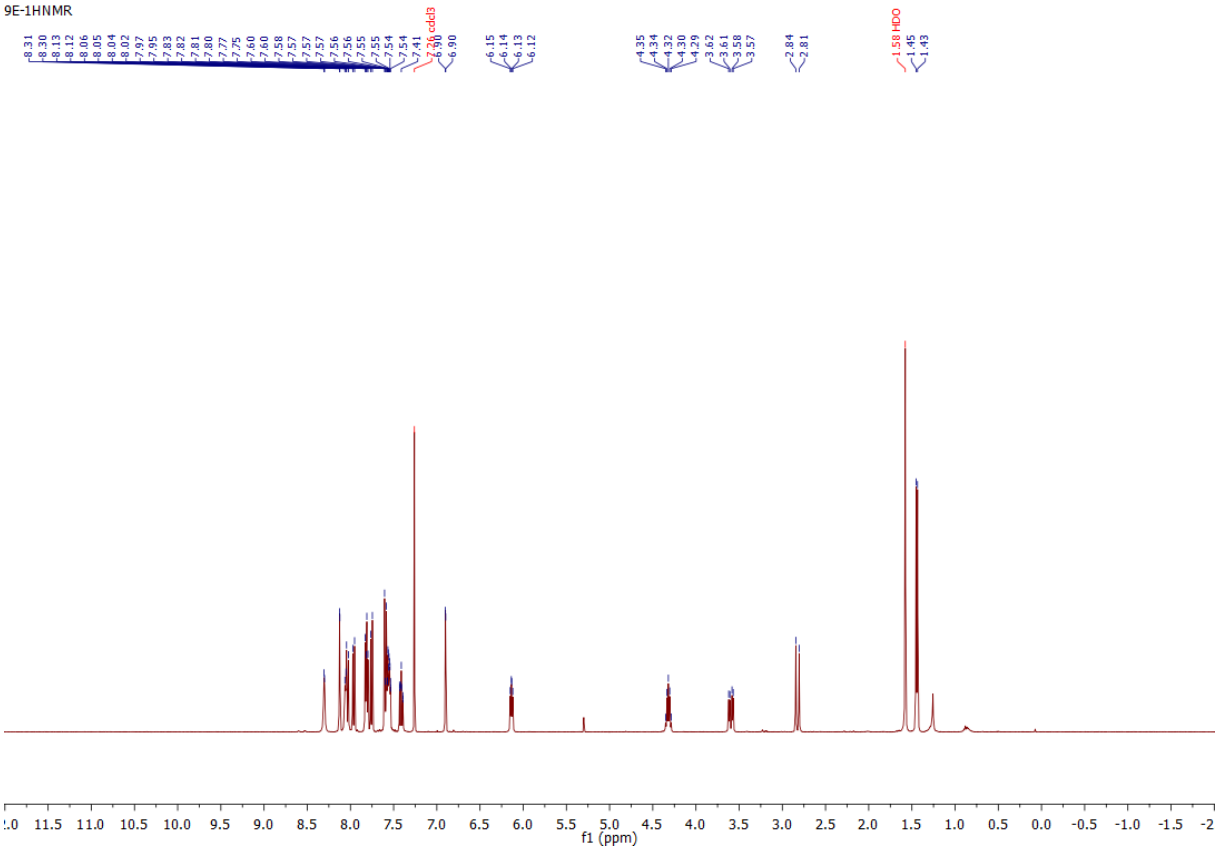

Supplementary Figure 69. ^{1}H NMR spectrum of **10-*E***.

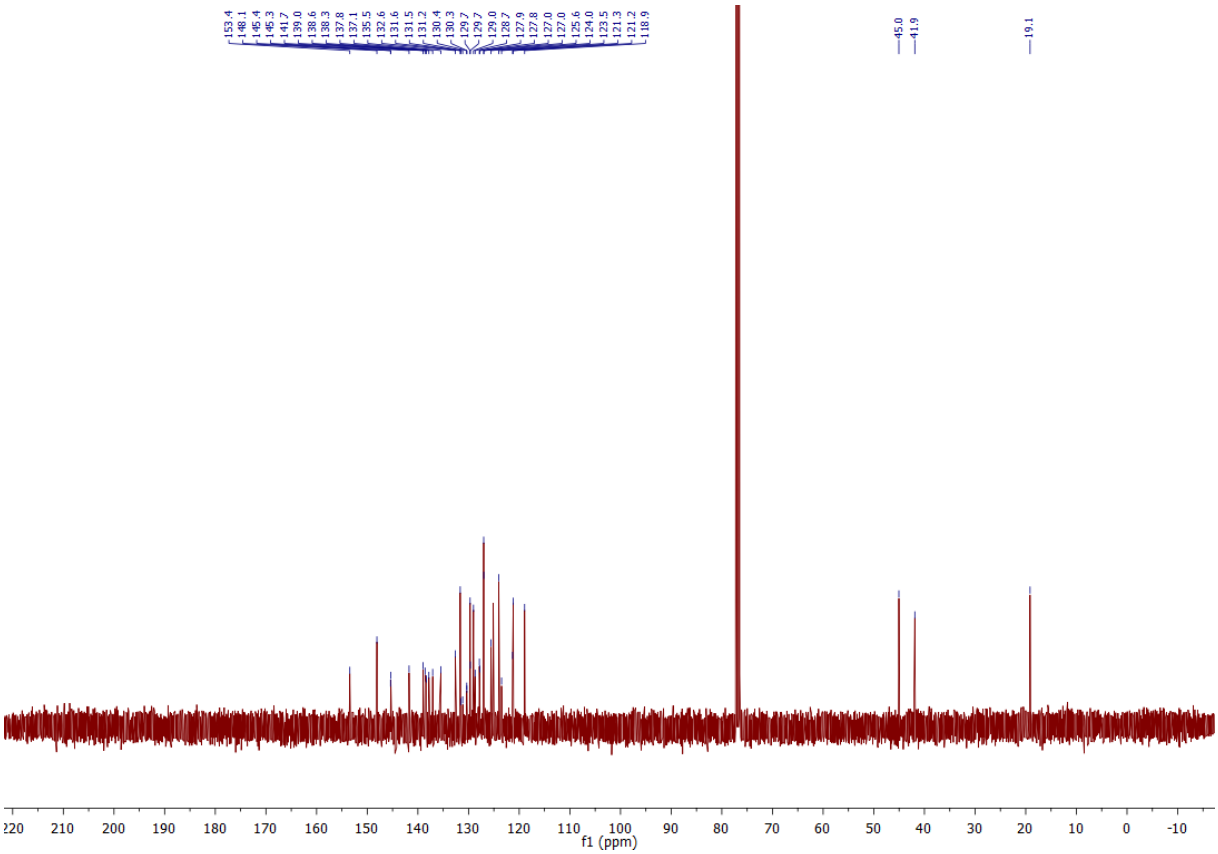

Supplementary Figure 70. ^{13}C NMR spectrum of **10-*E***.

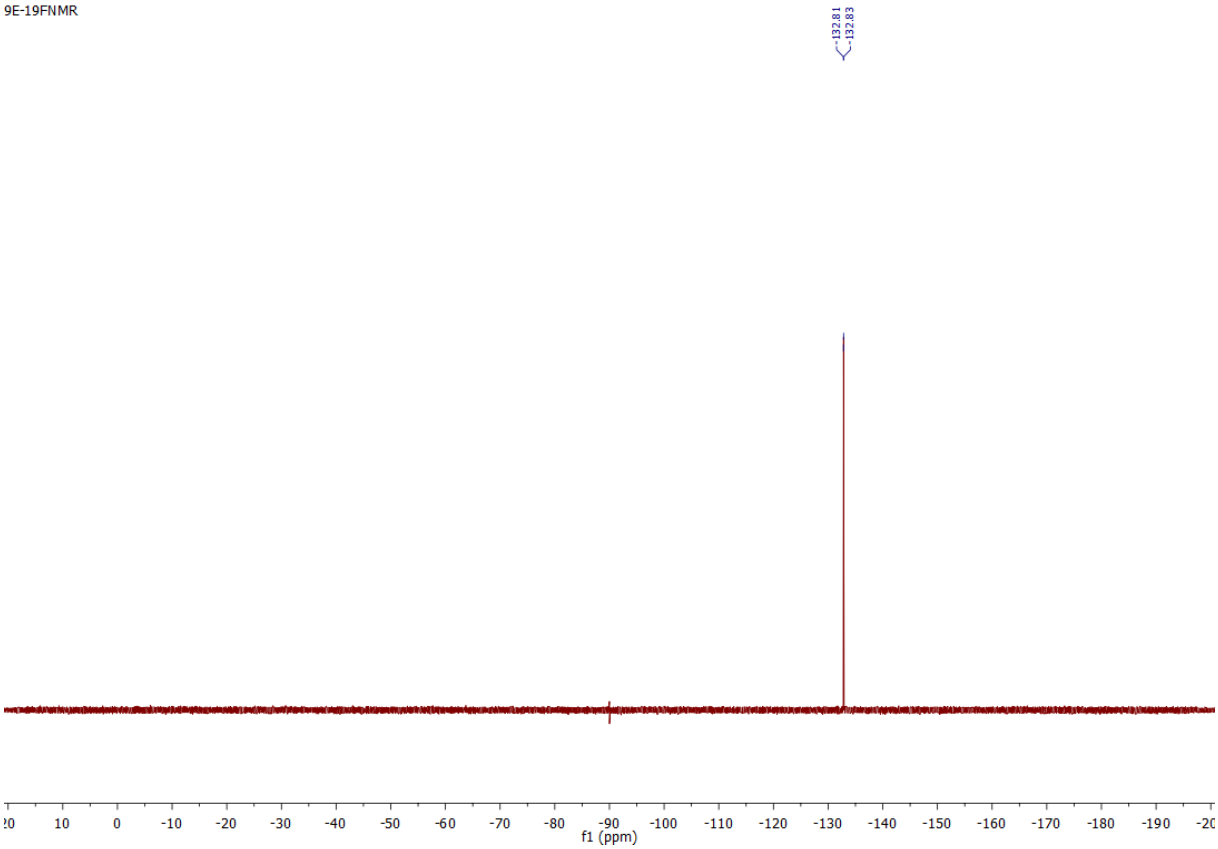

Supplementary Figure 71. ^{19}F NMR spectrum of **10-*E***.

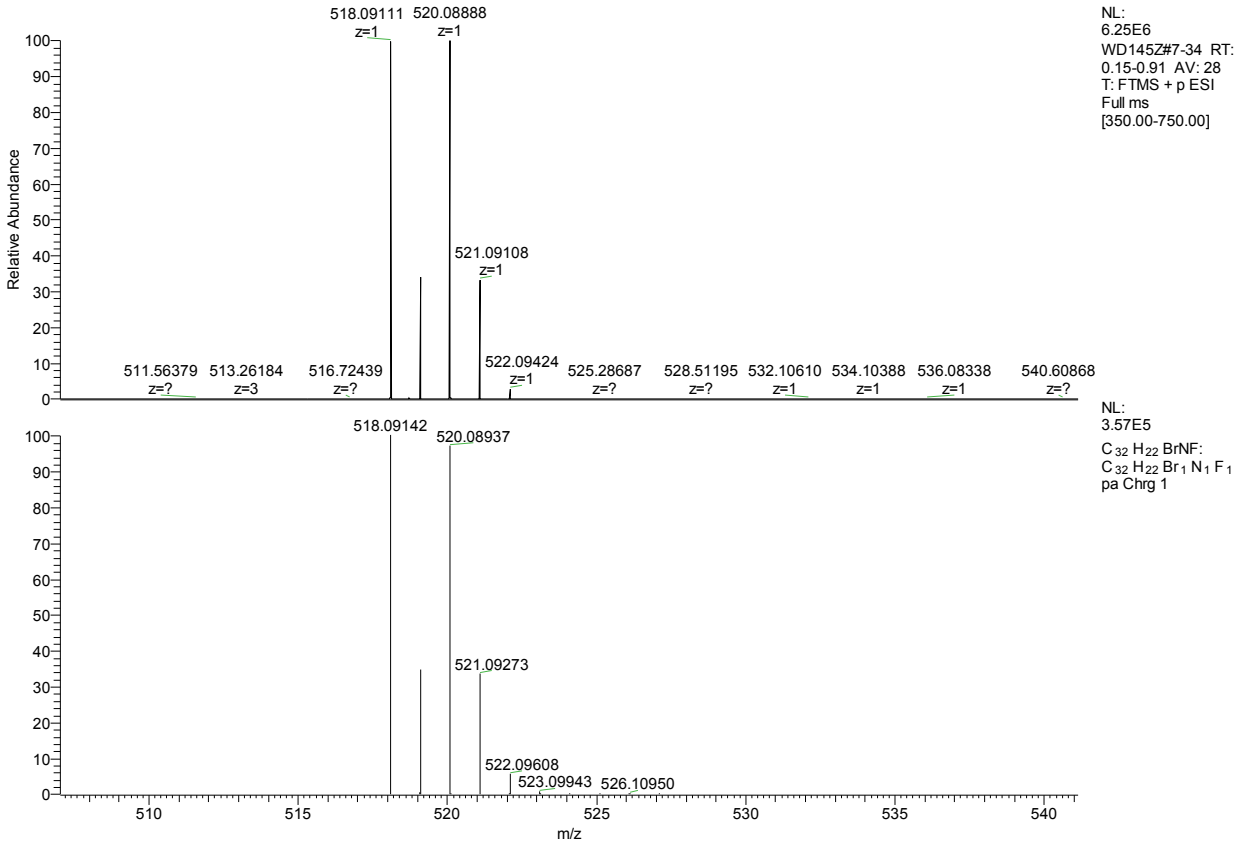

Supplementary Figure 72. HRMS (ESI) spectra of **10-*E*** (top:measured, bottom: calcd.).

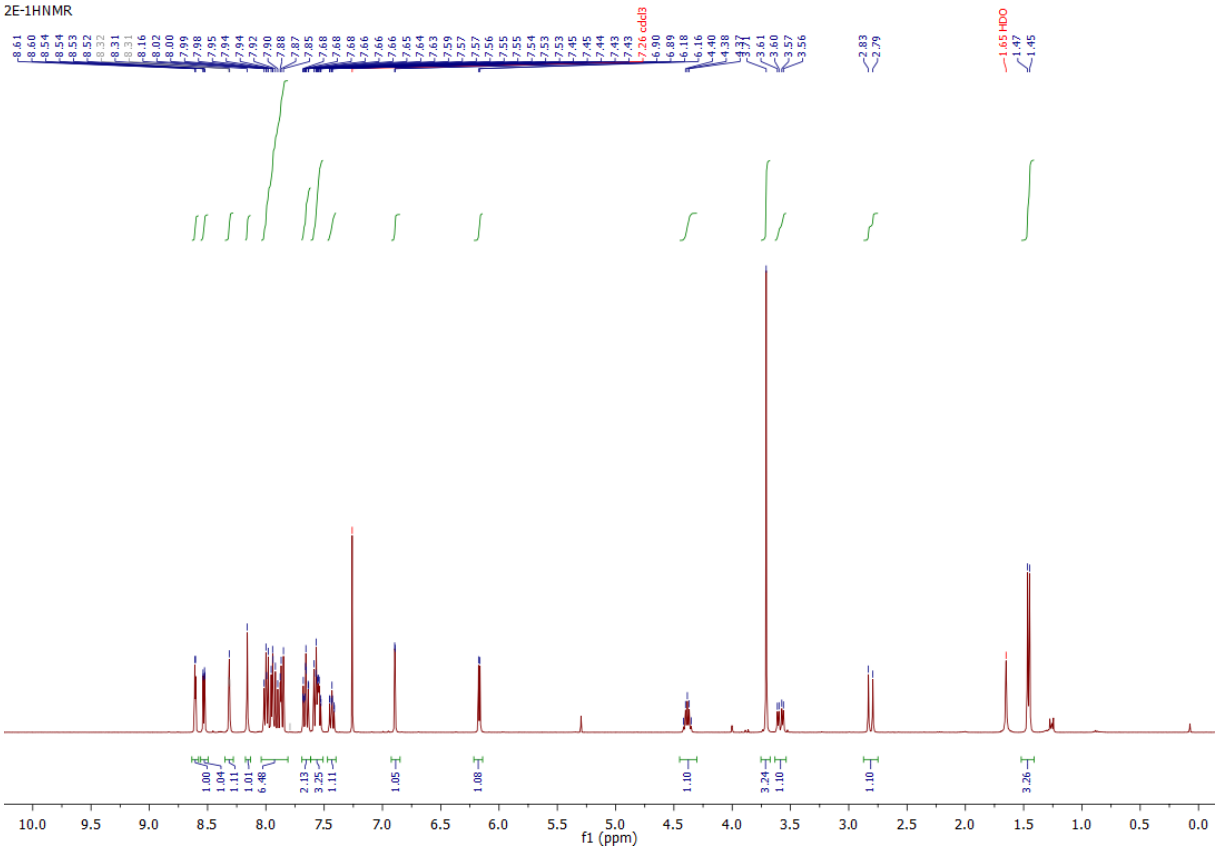

Supplementary Figure 73. ^{1}H NMR spectrum of **2-*E***.

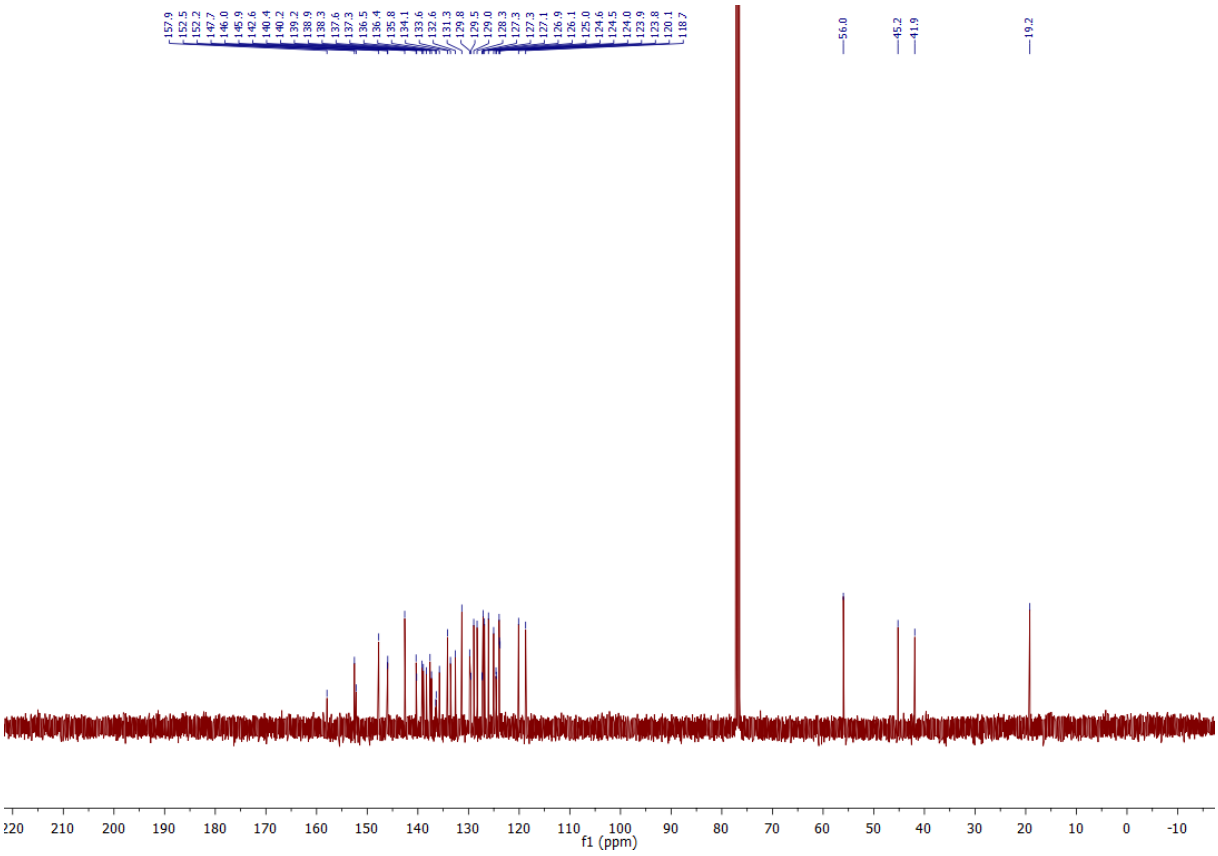

Supplementary Figure 74. ^{13}C NMR spectrum of **2-*E***.

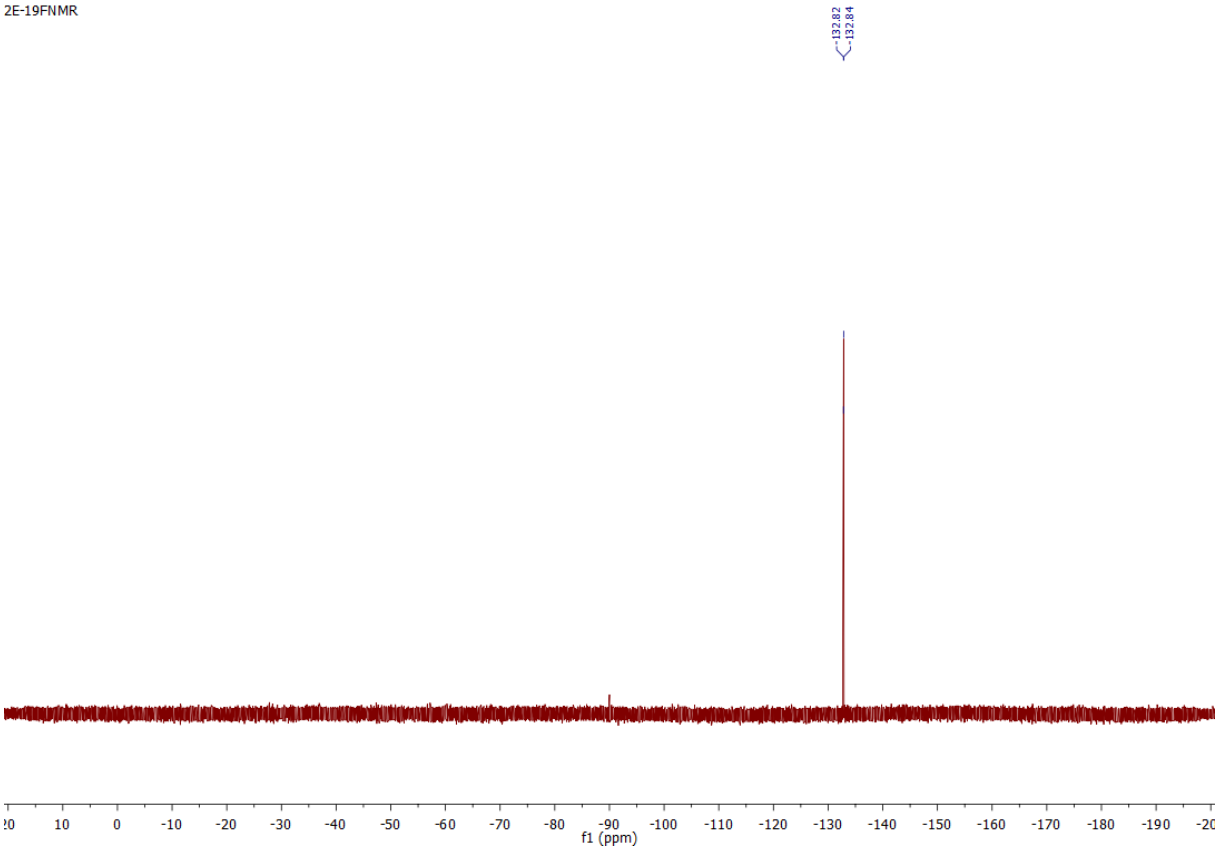

Supplementary Figure 75. ^{19}F NMR spectrum of **2-*E***.

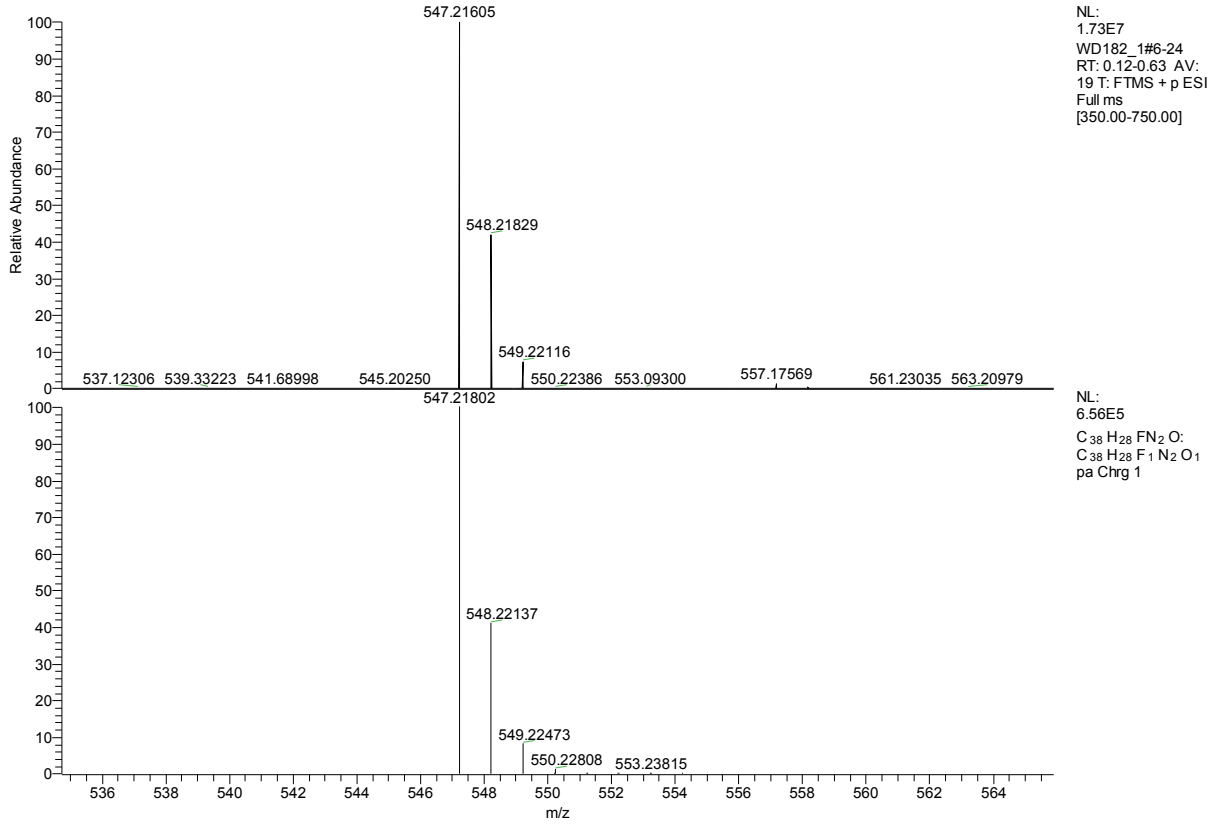

Supplementary Figure 76. HRMS (ESI) spectra of **2-*E*** (top :measured, bottom: calcd.).

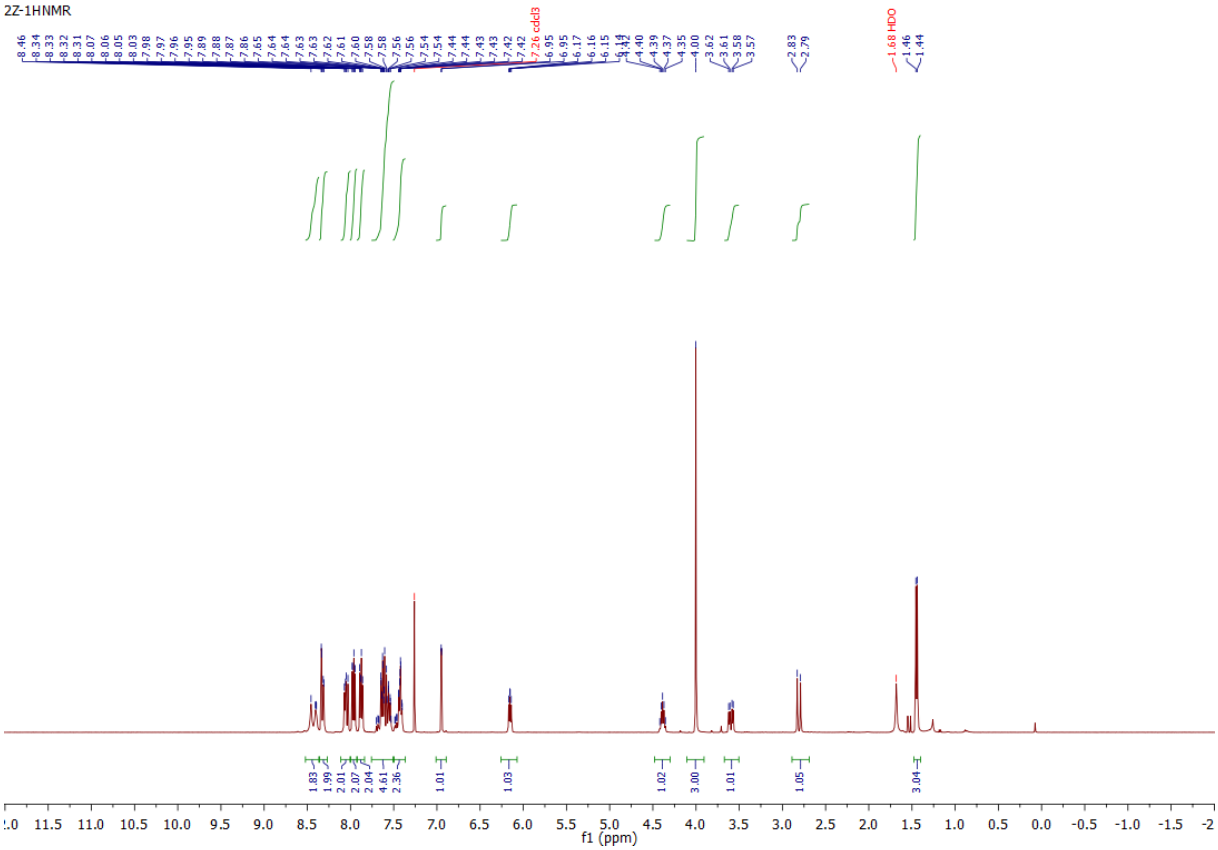

Supplementary Figure 77. ^{1}H NMR spectrum of **2-*Z***.

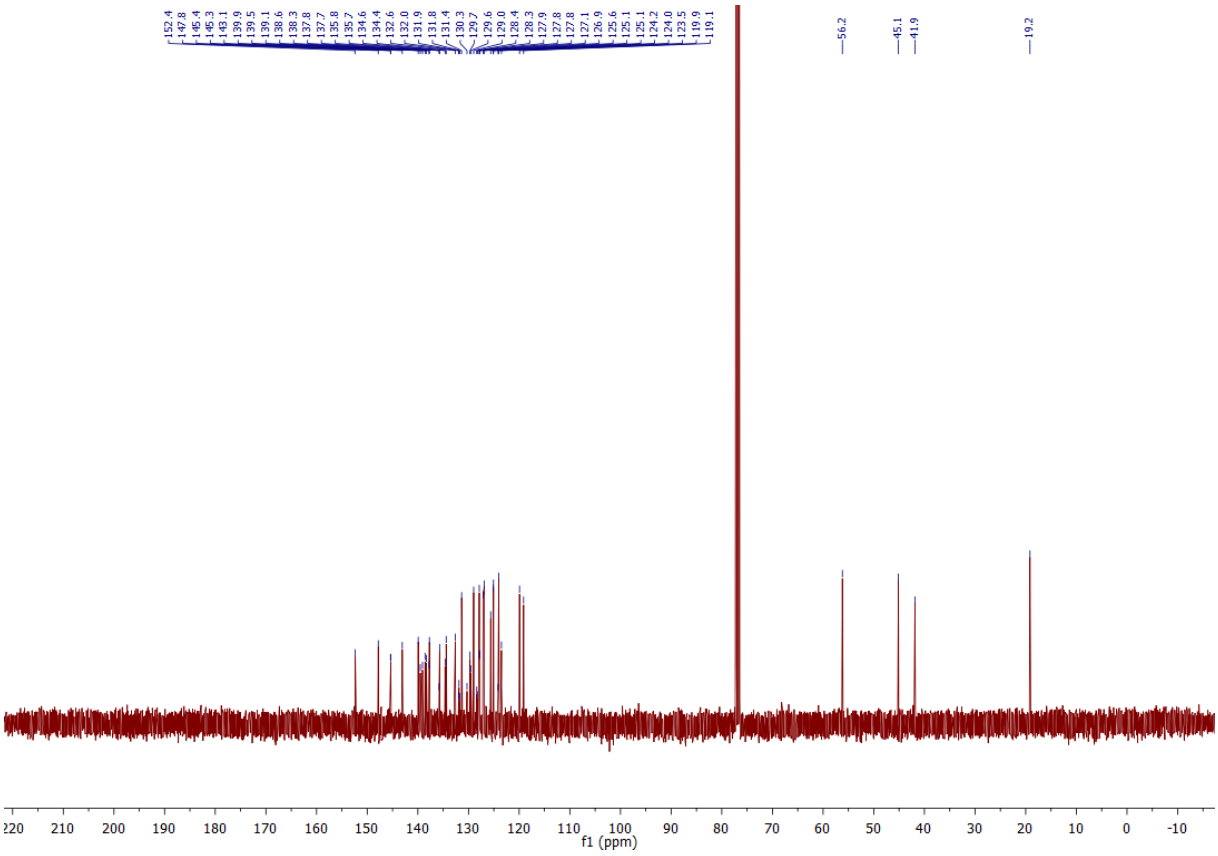

Supplementary Figure 78. ^{13}C NMR spectrum of **2-*Z***.

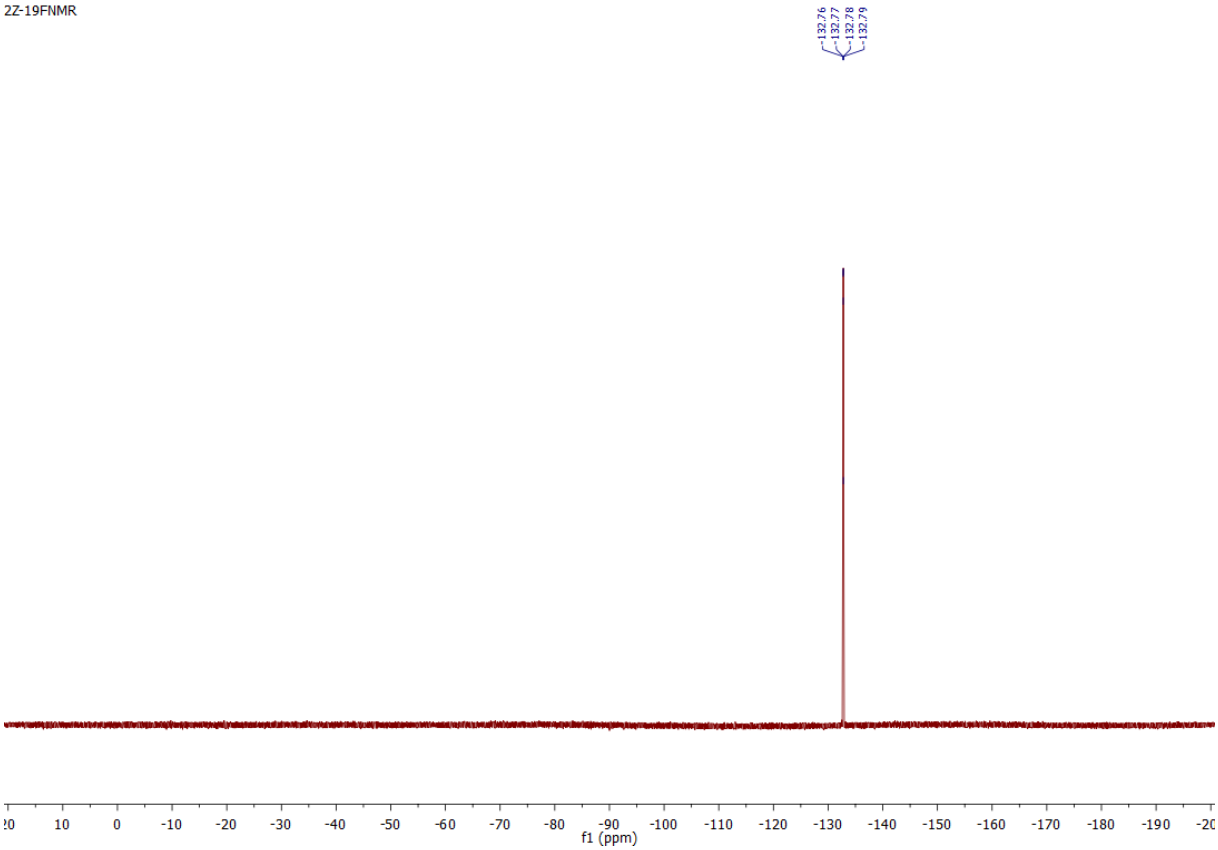

Supplementary Figure 79. ^{19}F NMR spectrum of **2-*Z***.

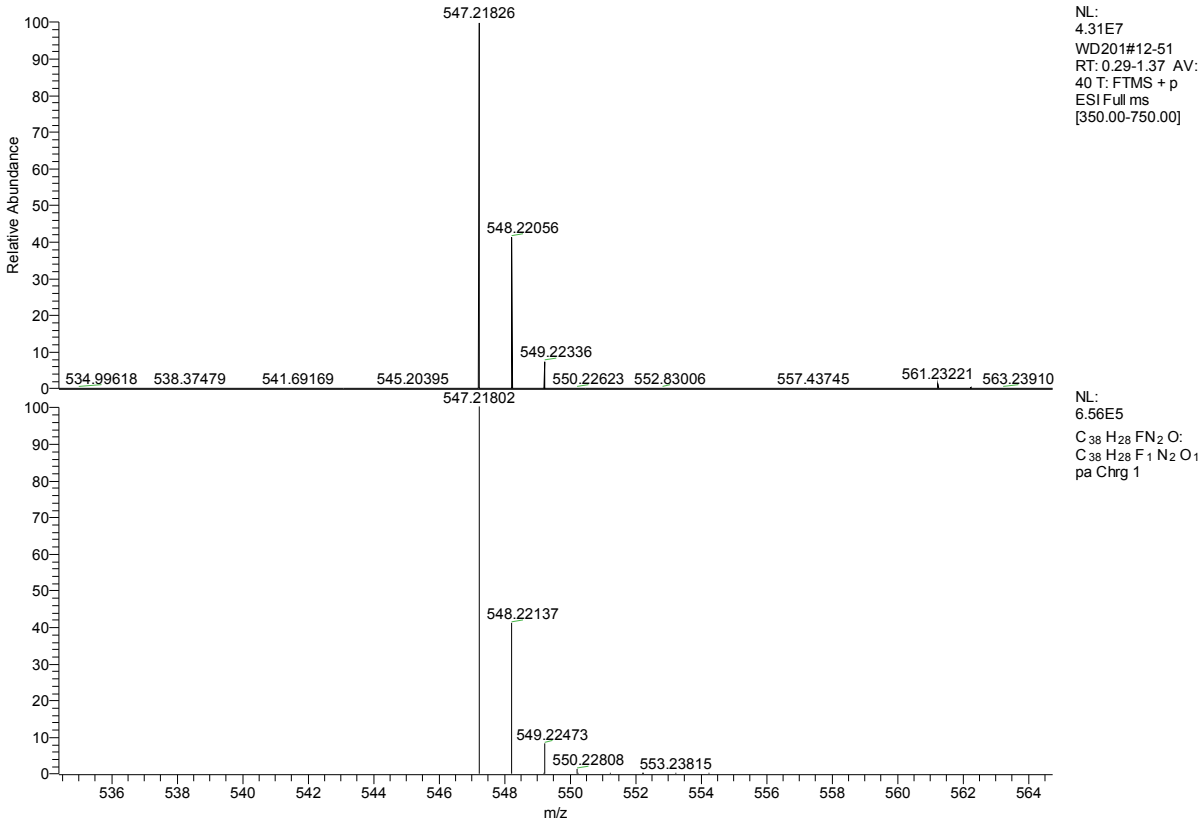

Supplementary Figure 80. HRMS (ESI) spectra of **2-*Z*** (top:measured, bottom: calcd.).

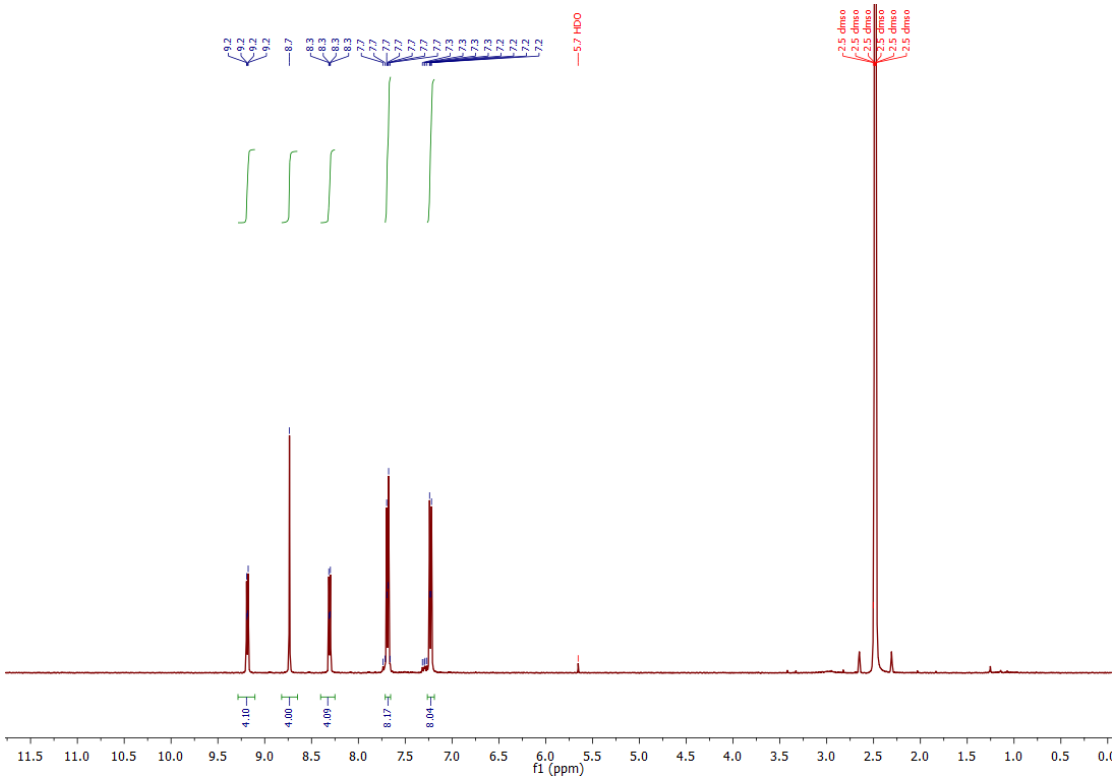

Supplementary Figure 81. ^{1}H NMR spectrum of digested (D_2SO_4) crystals of parent MOF.

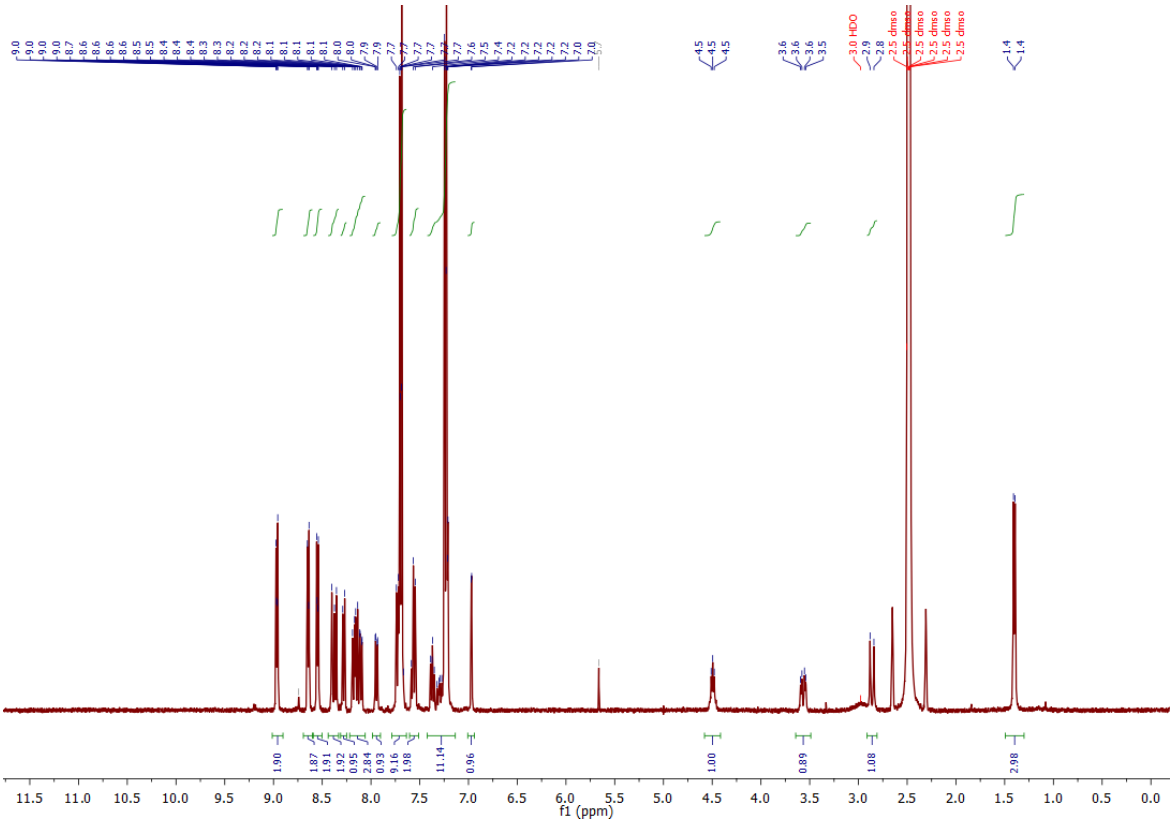

Supplementary Figure 82. ^{1}H NMR spectrum of digested (with D_2SO_4) crystals of moto-MOF**1**.

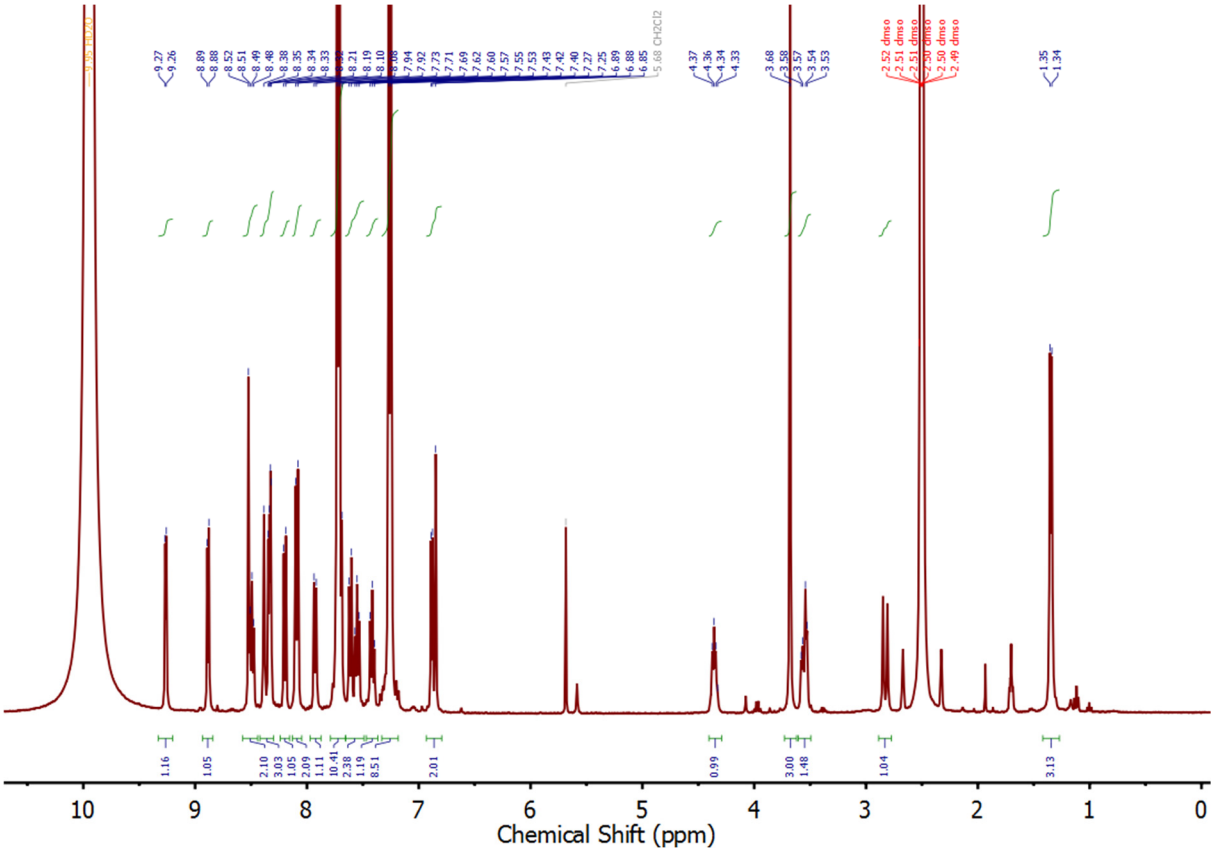

Supplementary Figure 83. ^{1}H NMR spectrum of digested (with D_2SO_4) crystals of moto-MOF**2-*E***.

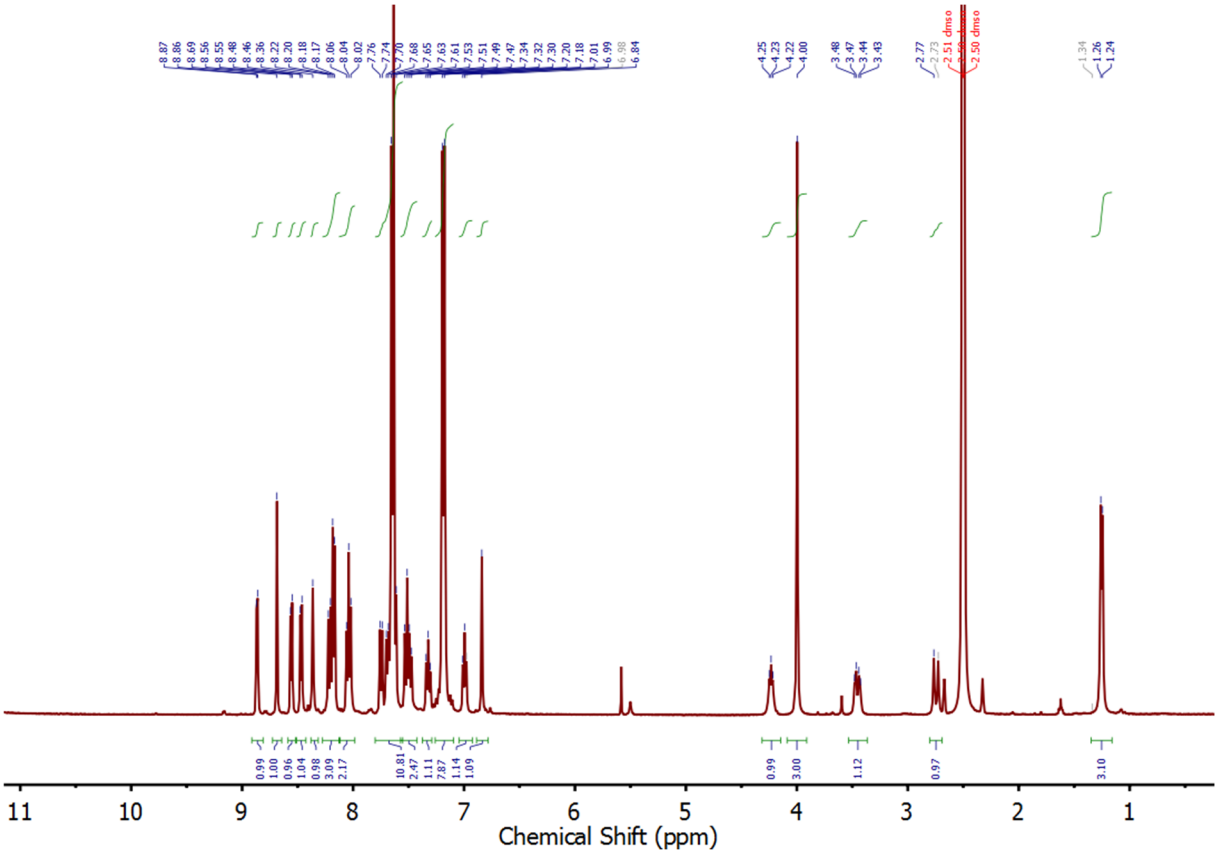

Supplementary Figure 84. ^{1}H NMR spectrum of digested (with D_2SO_4) crystals of moto-MOF**2-*Z***.

15. References

1. Davis, P. J. *et al.* Substituted diaryldiazomethanes and diazofluorenes: Structure, reactivity and stability. *Tetrahedron Lett.* **52,** 1553–1556 (2011).
2. Pijper, D. & Feringa, B. L. Molecular transmission: Controlling the twist sense of a helical polymer with a single light-driven molecular motor. *Angew. Chem. Int. Ed.* **46,** 3693–3696 (2007).
3. Valášek, M. *et al.* Synthesis of molecular tripods based on a rigid 9,9'-spirobifluorene scaffold. *J. Org. Chem.* **79,** 7342–7357 (2014).
4. Farha, O. K., Malliakas, C. D., Kanatzidis, M. G. & Hupp, J. T. Control over Catenation in Metal- Organic Frameworks via Rational Design of the Organic Building Block. *J. Am. Chem. Soc.* **132,** 950–952 (2010).
5. Feldmeier, C., Bartling, H., Riedle, E. & Gschwind, R. M. LED based NMR illumination device for mechanistic studies on photochemical reactions - Versatile and simple, yet surprisingly powerful. *J. Magn. Reson.* **232,** 39–44 (2013).
6. Frisch, M. J.; Trucks, G. W.; Schlegel, H. B.; Scuseria, G. E.; Robb, M. A.; Cheeseman, J. R.; Scalmani, G.; Barone, V.; Mennucci, B.; Petersson, G. A.; Nakatsuji, H.; Caricato, M.; Li, X.; Hratchian, H. P.; Izmaylov, A. F.; Bloino, J.; Zheng, G.; Sonnenberg, J. L.; Hada, M.; Ehara, M.; Toyota, K.; Fukuda, R.; Hasegawa, J.; Ishida, M.; Nakajima, T.; Honda, Y.; Kitao, O.; Nakai, H.; Vreven, T.; Montgomery, J. A., Jr.; Peralta, J. E.; Ogliaro, F.; Bearpark, M.; Heyd, J. J.; Brothers, E.; Kudin, K. N.;

Staroverov, V. N.; Kobayashi, R.; Normand, J.; Raghavachari, K.; Rendell, A.; Burant, J. C.; Iyengar, S. S.; Tomasi, J.; Cossi, M.; Rega, N.; Millam, N. J.; Klene, M.; Knox, J. E.; Cross, J. B.; Bakken, V.; Adamo, C.; Jaramillo, J.; Gomperts, R.; Stratmann, R. E.; Yazyev, O.; Austin, A. J.; Cammi, R.; Pomelli, C.; Ochterski, J. W.; Martin, R. L.; Morokuma, K.; Zakrzewski, V. G.; Voth, G. A.; Salvador, P.; Dannenberg, J. J.; Dapprich, S.; Daniels, A. D.; Farkas, Ö.; Foresman, J. B.; Ortiz, J. V.; Cioslowski, J.; Fox, D. J. Gaussian 09, revision D.01; Gaussian: Wallingford, CT, 2013. Frisch, M. J.; Trucks, G. W.; Schlegel, H. B.; Scuseria, G. E.; Robb, M. A.; Cheeseman, J. R.; Scalmani, G.; Barone, V.; Mennucci, B.; Petersson, G. A.; Nakatsuji, H.; Caricato, M.; Li, X.; Hratchian, H. P.; Izmaylov, A. F.; Bloino, J.; Zheng, G.; Sonnenberg, J. L.; Hada, M.; Ehara, M.; Toyota, K.; Fukuda, R.; Hasegawa, J.; Ishida, M.; Nakajima, T.; Honda, Y.; Kitao, O.; Nakai, H.; Vreven, T.; Montgomery, J. A., Jr.; Peralta, J. E.; Ogliaro, F.; Bearpark, M.; Heyd, J. J.; Brothers, E.; Kudin, K. N.; Staroverov, V. N.; Kobayashi, R.; Normand, J.; Raghavachari, K.; Rendell, A.; Burant, J. C.; Iyengar, S. S.; Tomasi, J.; Cossi, M.; Rega, N.; Millam, N. J.; Klene, M.; Knox, J. E.; Cross, J. B.; Bakken, V.; Adamo, C.; Jaramillo, J.; Gomperts, R.; Stratmann, R. E.; Yazyev, O.; Austin, A. J.; Cammi, R.; Pomelli, C.; Ochterski, J. W.; Martin, R. L.; Morokuma, K.; Zakrzewski, V. G.; Voth, G. A.; Salvador, P.; Dannenberg, J. J.; Dapprich, S.; Daniels, A. D.; Farkas, Ö.; Foresman, J. B.; Ortiz, J. V.; Cioslowski, J.; Fox, D. J. Gaussian 09, revision D.01; Gaussian: Wallingford, CT, 2013.

7. Becke, A. D. J. Density-functional thermochemistry. III. The role of exact exchange. *J. Chem. Phys.* **98,** 5648–5652 (1993).
8. Vosko, S. H., Wilk, L. & Nusair, M. Accurate spin-dependent electron liquid correlation energies for local spin density calculations: a critical analysis. *Can. J. Phys.* **58,** 1200–1211 (1980).
9. Lee, C., Yang, W. & Parr, R. G. Development of the Colle-Salvetti correlation-energy formula into a functional of the electron density. *Phys. Rev. B* **37,** 785–789 (1988).
10. Schreurs, A.M.M., Xian, X., Kroon-Batenburg, L. M. J. EVAL15: a diffraction data integration method based on ab initio predicted profiles. *J. Appl. Cryst.* **43,** 70–82 (2010).
11. Kuwahara, S. *et al.* Thermal E / Z Isomerization in First Generation Molecular Motors. *J. Org. Chem.* **83,** 4800–4804 (2018).
12. Kistemaker, J. C. M., Pizzolato, S. F., van Leeuwen, T., Pijper, T. C. & Feringa, B. L. Spectroscopic and Theoretical Identification of Two Thermal Isomerization Pathways for Bistable Chiral Overcrowded Alkenes. *Chem. Eur. J.* **22,** 13478–13487 (2016).
13. Štacko, P., Kistemaker, J. C. M. & Feringa, B. L. Fluorine-Substituted Molecular Motors with a Quaternary Stereogenic Center. *Chem. Eur. J.* **23,** 6643–6653 (2017).
14. Chen, J., Kistemaker, J. C. M., Robertus, J. & Feringa, B. L. Molecular stirrers in action. *J. Am. Chem. Soc.* **136,** 14924–14932 (2014).
15. Conyard, J. *et al.* Ultrafast Excited State Dynamics in Molecular Motors: Coupling of Motor Length to Medium Viscosity. *J. Phys. Chem. A* **121,** 2138–2150 (2017).